Field-Effect Transistors and Optoelectronic Devices Based on Emerging Atomically Thin Materials

Submitted by Selim Unal to the University of Exeter as a thesis for the degree of Doctor of Philosophy in Physics,

January 2017.

This thesis is available for library use on the understanding that it is copyright material and that no quotation from the thesis may be published without proper acknowledgement.

I certify that all material in this thesis which is not my own work has been identified and that no material has previously been submitted and approved for the award of a degree by this or any other university.

Selim Unal

January 2017

Field-Effect Transistors and Optoelectronic Devices Based on Emerging Atomically Thin Materials

Selim Unal

CEMPS,

University of Exeter,

Exeter,

UK,

EX4 4QL

January 2017

Abstract

Development of field-effect transistors and their applications is advancing at a relentless pace. Since the discovery of graphene, a single layer of carbon atoms, the ability to isolate and fabricate devices on atomically thin materials has marked a paradigm shift in the timeline of transistor technologies.

In this thesis, electrical and optical properties of atomically thin structures of graphene and tungsten disulfide (WS_2) are investigated. Transport in graphene side-gated transistors and contact resistance at the metal-WS_2 interface are presented. Finally, the optoelectronic performance of the hybrid graphene-WS_2 devices is examined.

Presently, atomically thin semiconductors grown by chemical vapour deposition are of growing interest by a broad scientific community. For this work of thesis, an air stable material which requires non-toxic gases for the growth such as WS_2 is selected. A considerable contact resistance at the metal/WS_2 interface is found to hamper the electrical performance of WS_2 transistors. The possible origin of this contact resistance is presented in this thesis.

The graphene field-effect transistors with graphene side gates are fabricated by a single step of electron beam lithography and an O_2 etching procedure. A comparative study of the electrical transport properties as a function of a bias applied to the side and back gate is conducted. The side gates allow for a much more efficient modulation of the charge density in the graphene channel owing to the larger maximum electric field which can experimentally be accomplished. Furthermore, the leakage between the side gate and the graphene channel is studied in a vacuum environment. It is found that the transport between graphene and the side gate

is associated with Fowler-Nordheim tunnelling and Frenkel-Poole transport. More specifically, for voltages less than 60 V, the Frenkel-Poole transport dominates the transport, whereas the Fowler-Nordheim tunnelling governs the transport at higher bias.

Finally, optoelectronic properties of graphene-WS_2 heterostructure are explored. An ionic polymer is used as a top gate to enhance the screening of long-lived trap charges. Responsivities as large as 10^6 A/W under illumination with 600 nm wavelength of light are demonstrated at room temperature. The fall and rise time are in the order of milliseconds due to the screening of the traps by the ionic polymer. This study is the first presentation of the transition metal dichalcogenide (TMDC)-graphene hybrid heterostructure with such a high photoresponsivity and fast response times.

Acknowledgement

First and foremost, I would like to thank my supervisor Saverio Russo for his tremendous support, encouragement and help during my research. I am grateful to him for giving chance and confidence to collaborate, my colleagues, Russo-Craciun lab members and many groups. I have gained a lot of experience working with you becoming a much better scientist. I would also like to thank Monica Craciun for being my second supervisor and useful discussions. I am grateful to have worked with many excellent colleagues and friends in the Russo-Craciun lab.

I would like to thank all my collaborators, co-workers, past and present for their contributions to this thesis. Jake Mehew for helping me in the measurements and understanding of the graphene-TMDC hybrid structure optoelectronic devices. Mohsin Aziz for assisting me in the initial measurements of the field-effect transistors. Elias Torres Alonso for transferring CVD graphene. Saad Ramadhan for his magic ionic polymer. Gareth Jones for his useful discussions in optoelectronics.

During my studies, I had the pleasure to work with great people from the University of Salerno and CNR-SPIN Salerno. I would like to thank Antonio Di Battolomeo and Filippo Giubileo for the hard work they have done. In addition, Cecilia Mattevi from Imperial College London deserves thanks for growing CVD TMDCs.

I would like to thank my lab-mates in G25, Matt Barnes, Nicola Townsend and Adolfo De Sanctis for their friendship, bringing cakes, building measurement setups and collaboration. I would like to thank former and current members of Russo-Craciun lab Toby Octon, Iddo Amit, Mukond Khetani, Peng Tian, Dominique Wehenkel, George Karkera, Will Rees, Guerino Avallone, Kieran Walsh for their friendships, discussions and collaboration.

I would like to thank the technicians and experimental officers at the University. Thanks to Adam Woodgate and David Gregory for supplying liquid helium constantly for measurements, Paul Wilkins for helping on workshop jobs and setting up measurement tools, cutting metallic pieces, Mark Heath for keeping the clean room in order and providing assistance, David Hudson and Tom Bointon for training in clean room equipment.

Special thanks to brilliant colleagues Nicola Townsend, Jake Mehew, Matt Barnes and Gareth Jones for giving me feedback and checking the grammar of this thesis. I also want to thank Turkish community and PhD students helping me to adjust easily to a new environment, providing constant motivation and suggestions.

At last, not least, I thank my parents, my brother and sister for their constant support and encouragement all these years.

Contents

List of Figures

List of Abbreviations

2D Two-Dimensional

Au Gold

CVD Chemical Vapor Deposition

DI Deionized

DOS Density of States

EBL Electron Beam Lithography

EQE External Quantum Efficiency

$FeCl_3$ Iron(III) Chloride

FET Field-Effect Transistor

IPA Isopropyl Alcohol

IQE Internal Quantum Efficiency

JDOS Joint Density of States

$LiClO_4$ Lithium Perchlorate

MEK Methyl Ethyl Ketone

MIBK Methyl Isobutyl Ketone

MoS_2 Molybdenum Disulfide

NEP Noise Equivalent Power

PEO Poly (ethylene oxide)

PMGI Polymethylglumarimide

PMMA Poly-methyl Methacrylate

SiO_2 Silicon Dioxide

SPCM Scanning Photocurrent Microscopy

TMDC Transition Metal Dichalcogenide

TTL Transistor-Transistor Logic

WS_2 Tungsten Disulfide

Chapter 1

Introduction

1.1 Problem statement and aims

There has been growing interest in fast, energy-efficient and cheap electronic devices in the semiconductor industry since the discovery of the field-effect transistor (FET). The integration of these devices in compact structures is essential to the development of future electronics. Following Moore's law, density of FETs is expected to increase on a microprocessor chip as well as their performance reducing the node size [1]. As the transistor size decreases down to the single atom device, the validity of this law is questioned [2, 3]. Presently, the semiconductor industry is more focussed on finding novel applications for these nanodevices and production of them, depending on what is desired for specific needs rather than supplying better chips [3]. In order to improve these devices, novel materials with higher charge carrier mobilities, high optical transparency and electrical conductivity are highly sought for in combination with added functionalities such as mechanical flexibility and resilience to harsh environments. To this end, the emerging class of atomically thin two-dimensional (2D) materials has been attracting wide interest by the scientific community.

Graphene, which is the first experimentally isolated two-dimensional material, is a single atomic layer of carbon atoms on a honeycomb lattice. Since the early theoretical studies by P. Wallace in 1947 [4], it was commonly believed that free-

standing graphene should not exist since long ranged crystalline order in 2D cannot occur [5]. This scenario changed in 2004 when for the very first time graphene was isolated and electrical measurements in a single atom thick transistor were demonstrated by the team of Prof. A. Geim and K. Novoselov (Nobel Prize in Physics, 2010) [6].

Graphene is a highly transparent and flexible material. The visible light absorption is 2.3% [7]. It can be stretched up to 20% before breaking [8] and it exhibits record high values of charge carrier mobility at room temperature [9]. Low values of contact resistance ($\sim 100\ \Omega\ \mu$m) have been demonstrated at the graphene/metal interface, and its use in a wide range of research areas to include electronic, optoelectronic, chemical, biological sensing and energy storage has been demonstrated [10–14]. Even though, graphene has a unique gamut of properties, the lack of an energy gap in the energy dispersion limits its usage in integrated circuits and optoelectronics.

After the isolation of graphene, many other 2D materials have been discovered and many are still waiting to be explored. Presently, transition metal dichalcogenides (TMDCs) are attracting growing attention by the scientific community since they can display metallic, superconducting and semiconducting properties. These materials are compounds with the general formula MX_2, where M is a transition metal and X is an element of the chalcogen group. For example, dichalcogenides with group V transition metals Nb and Ta show metallic and superconducting properties whereas Mo and W based TMDCs are usually semiconducting with a large band gap [15, 16]. Similar to graphene, single atomic layers of these materials can be obtained easily by mechanical cleavage method due to the weak van der Waals forces between the layers. Semiconducting TMDCs have a large band gap which is tunable with the number of layers making them suitable for optoelectronics, digital electronics and energy harvesting applications [17–19].

However, the development of fast electronic and optoelectronic applications based on TMDCs is presently facing several challenges. For example, the presence of a large Schottky barrier at the metal/TMDC interface results in high contact resis-

tance and reduces the performance of the device. Furthermore, trapped charges on the substrate due to the random distribution of charged impurities at the interface are also known to limit the values of charge carrier mobility [20]. The encapsulation of these materials in an ionic polymer has been shown to improve the values of mobility, though significant advances would truly require a better control of the atomic defects present in the crystal structure of these materials [21, 22].

Recent advances in the research on 2D materials are showing that hybrid structures obtained by transferring different atomically thin materials onto each other can display surprising properties, effectively overcoming some of the limitations of pure graphene or TMDCs [23]. For example, by using graphene edge contacts on MoS_2, the contact resistance is lowered, and an ohmic contact is achieved rather than a Schottky barrier [24]. Furthermore, hybrid structures of atomically thin materials can be used in photodetector applications. In this case, the high charge carrier mobility of graphene is combined with the presence of an energy gap in TMDC. A photogenerated electron (hole) in the TMDC can be extracted in graphene where it can recirculate many times before the hole (electron) left in the TMDC relaxes [25, 26]. This gain mechanism can result in highly sensitive photodetectors.

1.2 Thesis outline

In chapter 2, the band structure of graphene will be introduced. The energy dispersion relation and the linear dispersion relation near the Dirac point will be defined. The band structure of semiconducting TMDCs will be discussed. Three different mechanisms of electrical transport in graphene-TMDC heterostructures will be described. Photodetection mechanisms responsible for the photocurrent in graphene and TMDCs will be discussed and the key parameters used in the optoelectronic devices will be determined. The aim is to establish a background for the further chapters.

In chapter 3, fabrication methods for graphene and WS_2 will be discussed. Patterning methods including laser beam writing and nano-beam lithography will be

shown. Electrical and optical characterisation methods will be outlined. The optical setup used to characterise the optoelectronic properties of the two-dimensional materials will be described. The methods outlined in this chapter are used in the fabrication, characterisation and investigation of electrical and optoelectronic properties of the devices.

In chapter 4, fabrication of contact metals on WS_2 with variable distances will be demonstrated. The contact resistance of the chemical vapor deposition (CVD) grown few-layer WS_2 will be explained for two different measurements which are performed at cryogenic and room temperature.

In chapter 5, transport properties of graphene will be introduced with a Si/SiO_2 back gating and a graphene side gating effects. The back gate and the graphene side gate will be compared using their normalised transconductance. The transport at low and high voltage regimes will be interpreted with Fowler-Nordheim and Frenkel-Poole transport.

In chapter 6, a hybrid graphene-WS_2 device will be characterised electrically and using Raman spectroscopy. An ionic polymer will be used to gate bias the device. Optoelectronic properties of this heterostructure will be investigated using a scanning photocurrent microscopy and bulk illumination methods. The key parameters and responsivity spectra of the photodetector will be demonstrated.

Bibliography

[1] G. E. Moore, "Progress in digital integrated electronics," *IEDM Tech. Digest*, pp. 11–13, 1975.

[2] J. A. del Alamo, "Nanometre-scale electronics with III-V compound semiconductors," *Nature*, vol. 479, no. 7373, pp. 317–323, 2011.

[3] M. M. Waldrop, "The chips are down for Moore's law," *Nature*, vol. 530, pp. 144–147, Feb 2016.

[4] P. Wallace, "The band theory of graphite," *Physical Review*, vol. 71, pp. 622–634, May 1947.

[5] N. D. Mermin, "Crystalline order in two dimensions," *Physical Review*, vol. 176, pp. 250–254, Dec 1968.

[6] K. S. Novoselov, "Electric field effect in atomically thin carbon films," *Science*, vol. 306, pp. 666–669, Oct 2004.

[7] R. R. Nair, P. Blake, A. N. Grigorenko, K. S. Novoselov, T. J. Booth, T. Stauber, N. M. R. Peres, and A. K. Geim, "Fine structure constant defines visual transparency of graphene," *Science*, vol. 320, pp. 1308–1308, Jun 2008.

[8] C. Lee, X. Wei, J. W. Kysar, and J. Hone, "Measurement of the elastic properties and intrinsic strength of monolayer graphene," *Science*, vol. 321, pp. 385–388, Jul 2008.

[9] K. I. Bolotin, K. J. Sikes, Z. Jiang, M. Klima, G. Fudenberg, J. Hone, P. Kim, and H. L. Stormer, "Ultrahigh electron mobility in suspended graphene," *Solid State Communications*, vol. 146, no. 9-10, pp. 351–355, 2008.

[10] K. S. Novoselov, A. K. Geim, S. V. Morozov, D. Jiang, M. I. Katsnelson, I. V. Grigorieva, S. V. Dubonos, and A. A. Firsov, "Two-dimensional gas of massless Dirac fermions in graphene," *Nature*, vol. 438, pp. 197–200, Nov 2005.

[11] Z. Cheng, Q. Li, Z. Li, Q. Zhou, and Y. Fang, "Suspended graphene sensors with improved signal and reduced noise," *Nano Letters*, vol. 10, no. 5, pp. 1864–1868, 2010.

[12] M. Craciun, S. Russo, M. Yamamoto, and S. Tarucha, "Tuneable electronic properties in graphene," *Nano Today*, vol. 6, pp. 42–60, Feb 2011.

[13] M. F. El-Kady, V. Strong, S. Dubin, and R. B. Kaner, "Laser scribing of high-rerformance and flexible graphene-based electrochemical capacitors," *Science*, vol. 335, pp. 1326–1330, Mar 2012.

[14] F. H. L. Koppens, T. Mueller, P. Avouris, A. C. Ferrari, M. S. Vitiello, and M. Polini, "Photodetectors based on graphene, other two-dimensional materials and hybrid systems," *Nature Nanotechnology*, vol. 9, pp. 780–793, Oct 2014.

[15] M. S. El-Bana, D. Wolverson, S. Russo, G. Balakrishnan, D. M. Paul, and S. J. Bending, "Superconductivity in two-dimensional $NbSe_2$ field effect transistors," *Superconductor Science and Technology*, vol. 26, p. 125020, Dec 2013.

[16] B. Radisavljevic, A. Radenovic, J. Brivio, V. Giacometti, and A. Kis, "Single-layer MoS_2 transistors," *Nature Nanotechnology*, vol. 6, pp. 147–150, Mar 2011.

[17] D. Jariwala, V. K. Sangwan, L. J. Lauhon, T. J. Marks, and M. C. Hersam, "Emerging device applications for semiconducting two-dimensional transition metal dichalcogenides," *ACS Nano*, vol. 8, pp. 1102–1120, Feb 2014.

[18] Q. H. Wang, K. Kalantar-Zadeh, A. Kis, J. N. Coleman, and M. S. Strano, "Electronics and optoelectronics of two-dimensional transition metal dichalcogenides," *Nature Nanotechnology*, vol. 7, pp. 699–712, Nov 2012.

[19] H. Huang, Y. Cui, Q. Li, C. Dun, W. Zhou, W. Huang, L. Chen, C. A. Hewitt, and D. L. Carroll, "Metallic 1T phase MoS_2 nanosheets for high-performance thermoelectric energy harvesting," *Nano Energy*, vol. 26, pp. 172–179, May 2016.

[20] A. B. Kaul, "Two-dimensional layered materials: Structure, properties, and prospects for device applications," *Journal of Materials Research*, vol. 29, no. 03, pp. 348–361, 2014.

[21] S. Ghatak, A. N. Pal, and A. Ghosh, "Nature of electronic states in atomically thin MoS_2 field-effect transistors," *ACS Nano*, vol. 5, pp. 7707–7712, Oct 2011.

[22] M.-W. Lin, L. Liu, Q. Lan, X. Tan, K. S. Dhindsa, P. Zeng, V. M. Naik, M. M.-C. Cheng, and Z. Zhou, "Mobility enhancement and highly efficient gating of monolayer MoS_2 transistors with polymer electrolyte," *Journal of Physics D: Applied Physics*, vol. 45, no. 34, p. 345102, 2012.

[23] K. Roy, M. Padmanabhan, S. Goswami, T. P. Sai, G. Ramalingam, S. Raghavan, and A. Ghosh, "Graphene-MoS_2 hybrid structures for multifunctional photoresponsive memory devices," *Nature Nanotechnology*, vol. 8, pp. 826–830, Nov 2013.

[24] M. H. D. Guimarães, H. Gao, Y. Han, K. Kang, S. Xie, C. J. Kim, D. A. Muller, D. C. Ralph, and J. Park, "Atomically thin ohmic edge contacts between two-dimensional materials," *ACS Nano*, vol. 10, no. 6, pp. 6392–6399, 2016.

[25] G. Konstantatos, M. Badioli, L. Gaudreau, J. Osmond, M. Bernechea, F. P. G. de Arquer, F. Gatti, and F. H. L. Koppens, "Hybrid graphene-quantum dot phototransistors with ultrahigh gain," *Nature Nanotechnology*, vol. 7, no. 6, pp. 363–368, 2012.

[26] L. Britnell, R. M. Ribeiro, A. Eckmann, R. Jalil, B. D. Belle, A. Mishchenko, Y.-J. Kim, R. V. Gorbachev, T. Georgiou, S. V. Morozov, A. N. Grigorenko, A. K. Geim, C. Casiraghi, A. H. Castro Neto, and K. S. Novoselov, "Strong light-matter interactions in heterostructures of atomically thin films," *Science*, vol. 340, pp. 1311–1314, Jun 2013.

Chapter 2

Theoretical background

2.1 Electronic structure of graphene

Graphene is an atomically thin layer of carbon atoms arranged in a hexagonal lattice [1]. The electronic configuration of the carbon atoms is [He] $2s^2$ $2p^2$, hence they have four valence electrons in the outer shell. Each carbon atom is bonded to three other carbon atoms leaving one electron free in the p orbital for each atom. The $2p_z$ electrons form π bonds, yielding the lower (bonding) and higher (anti-bonding) energy bands of the graphene [2].

The lattice structure of graphene is characterised by two inequivalent atoms in the unit cell, commonly labelled as A and B. The primitive vectors a_1 and a_2 are

$$a_1 = \frac{a_{c-c}}{2}(3, \sqrt{3}), \qquad a_2 = \frac{a_{c-c}}{2}(3, -\sqrt{3}) \tag{2.1}$$

where $a_{c-c} \approx 1.42$ Å is the distance to the nearest carbon atom. The reciprocal lattice vectors in the Bravais lattice are

$$b_1 = \frac{2\pi}{3a_{c-c}}(1, \sqrt{3}), \qquad b_2 = \frac{2\pi}{3a_{c-c}}(1, -\sqrt{3}). \tag{2.2}$$

The three nearest-neighbour vectors for the A sublattice are given as

$$\delta_1 = a_{c-c}(1, 0), \qquad \delta_2 = \frac{a_{c-c}}{2}(-1, \sqrt{3}), \qquad \delta_3 = \frac{a_{c-c}}{2}(-1, -\sqrt{3}). \tag{2.3}$$

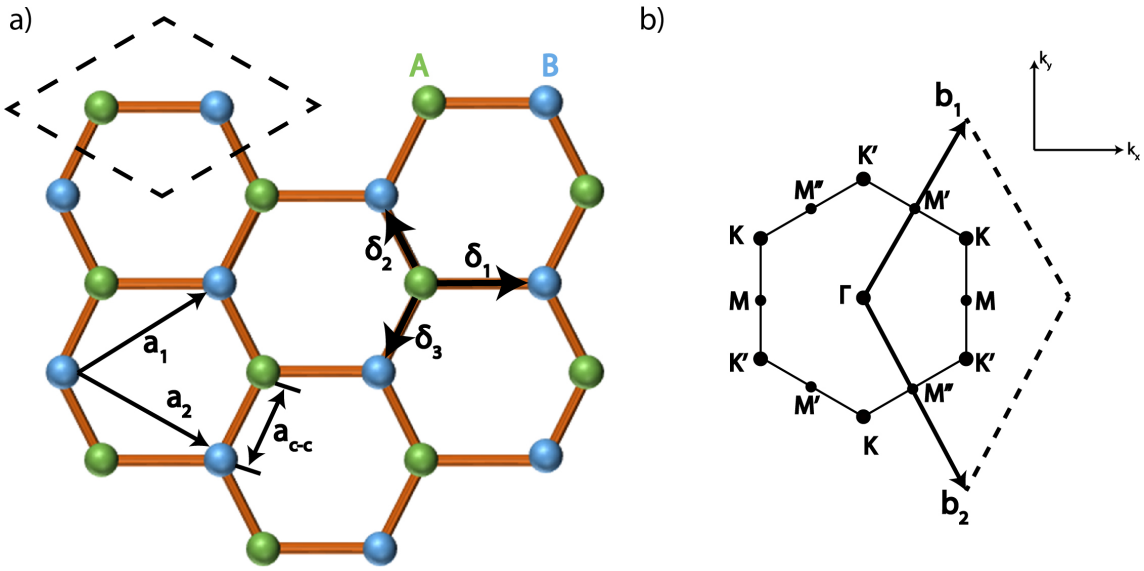

Figure 2.1: (a) The hexagonal lattice structure of single layer graphene. The balls correspond to the carbon atoms and the sticks are the σ bonds. a_1 and a_2 are the lattice unit vectors, and δ_1, δ_2 and δ_3 are the nearest-neighbour vectors. A and B are the sublattices shown as green and blue. (b) Reciprocal lattice and the first Brillouin zone (hexagonal area) with the Dirac points K and K'. Γ is the centre of Brillouin zone. b_1 and b_2 are the primitive lattice vectors. M, M' and M" are the three inequivalent crystallographic points.

2.1.1 Tight binding theory of graphene

The tight binding model is used to estimate the electronic energy dispersion of graphene [3]. I am interested in describing the properties of itinerant electrons which aid the flow of electric current and heat. The linear combination of atomic orbitals is adopted to write an expression for the electron wave function in the crystal using the wave functions of electrons on each of the two sublattices

$$\psi = c_1\Phi_1 + c_2\Phi_2. \tag{2.4}$$

Since itinerant electrons are focused on, each sublattice wave function is written as a Bloch sum

$$\Phi_1 = \frac{1}{\sqrt{N}}\sum_{R_A} e^{ikR_A}\phi(r - R_A), \qquad \Phi_2 = \frac{1}{\sqrt{N}}\sum_{R_B} e^{ikR_B}\phi(r - R_B). \tag{2.5}$$

where N is the number of unit cells in the lattice, the Bravais lattice vectors are R_A and R_B; $\phi(r - R_A)$ and $\phi(r - R_B)$ are the atomic wave functions of the p_z orbitals. To calculate the expectation value of the nearest neighbour tight binding Hamiltonian,

$$H_{AA} = H_{BB} = \langle \Phi_1 | H | \Phi_1 \rangle \tag{2.6}$$

and

$$H_{AB} = H^*_{BA} = \langle \Phi_1 | H | \Phi_2 \rangle. \tag{2.7}$$

are calculated. From the orthogonality conditions

$$\langle \Phi_1 | \Phi_1 \rangle = \langle \Phi_2 | \Phi_2 \rangle = 1, \qquad \langle \Phi_1 | \Phi_2 \rangle = \langle \Phi_2 | \Phi_1 \rangle = 0. \tag{2.8}$$

The H_{AA} and H_{AB} Hamiltonians are calculated as

$$H_{AA} = \frac{1}{N} \sum_{R_A R_{A'}} e^{ik(R_A - R_{A'})} \langle \Phi_1(r - R_{A'}) | H | \Phi_1(r - R_A) \rangle = \tag{2.9}$$

$$= \frac{1}{N} \sum_{R_A = R_{A'}} \varepsilon_{2p} + \frac{1}{N} \sum_{R_A = R_{A'} \pm a} e^{\pm ika} \langle \Phi_1(r - R_{A'}) | H | \Phi_1(r - R_A) \rangle + \tag{2.10}$$

$$+ \text{terms from } R_A = R_{A'} \pm 2a \text{ and larger.} \tag{2.11}$$

Small terms coming from the next-neighbour contributions are ignored. Assuming that the on-site energy of the A and B sublattice is the same and equal to ε_{2p}, the Hamiltonians are

$$H_{AA} = H_{BB} \approx \varepsilon_{2p} \tag{2.12}$$

and

$$H_{AB} = \frac{1}{N} \sum_{R_B R_A} e^{ik(R_B - R_A)} \langle \Phi_1(r - R_A) | H | \Phi_2(r - R_B) \rangle = \tag{2.13}$$

$$= \frac{t}{N} \sum_{R_B R_A} e^{ik(R_B - R_A)} = t f(k) \tag{2.14}$$

where $t = \langle \Phi_A(r - R_A)|H|\Phi(r - R_B)\rangle$,

$$f(k) = \sum_i^3 e^{ikR_i} = e^{\frac{ik_x a}{\sqrt{3}}} + 2e^{\frac{-ik_x a}{2\sqrt{3}}} cos(\frac{k_y a}{2}) \tag{2.15}$$

and a is $a_{c-c}\sqrt{3} = 2.46$ Å.

The overlap integral matrix S_{AA} and S_{BB} can be given as $S_{AA} = S_{BB} = 0$ and $S_{AB} = S_{BA^*} = sf(k)$ where $s = \langle \Phi_A(r - R_A)|\Phi_B(r - R_B)\rangle$. Then, the Hamiltonian, H and the overlap integral matrix S can be written as

$$H = \begin{pmatrix} \varepsilon_{2p} & tf(k) \\ tf(k)^* & \varepsilon_{2p} \end{pmatrix}, \qquad S = \begin{pmatrix} 1 & sf(k) \\ sf(k)^* & 1 \end{pmatrix}. \tag{2.16}$$

From $\det(H - ES) = 0$, one can find the eigenvalue E_k which gives the energy dispersion relation

$$E_k = \frac{\varepsilon_{2p} \pm tw(k)}{1 \pm sw(k)} \tag{2.17}$$

where ω(k) can be written as

$$\omega(k) = \sqrt{|f(k)|^2} = \sqrt{1 + 4cos(\frac{\sqrt{3}k_x a}{2})cos(\frac{k_y a}{2}) + 4cos^2(\frac{k_y a}{2})}. \tag{2.18}$$

The energy dispersion relation of graphene is plotted in Figure 2.2 using equation 2.17. Here, k_x and k_y are the components of the electron wave vector. t = -3 eV is the hopping energy of an electron from atom to its nearest neighbour, $s = 0.13$ is the nearest neighbour overlap integral, and ε_{2p} is the on-site energy which is equivalent for the A and B sublattices in pristine graphene and can be set equal to zero without loss of generality [4]. A finite difference between the on-site energy of A and B would result in the opening of energy band gap in the otherwise gapless energy dispersion of graphene. In the energy dispersion, + sign in the numerator and denominator corresponds to the valence band and π bonding whereas − sign gives the conduction band structure and π^* anti-bonding. K and K' points of the Brillouin zone signify points where the valence and the conduction band overlap giving the zero-band-gap

property of graphene, see Figure 2.2a inset.

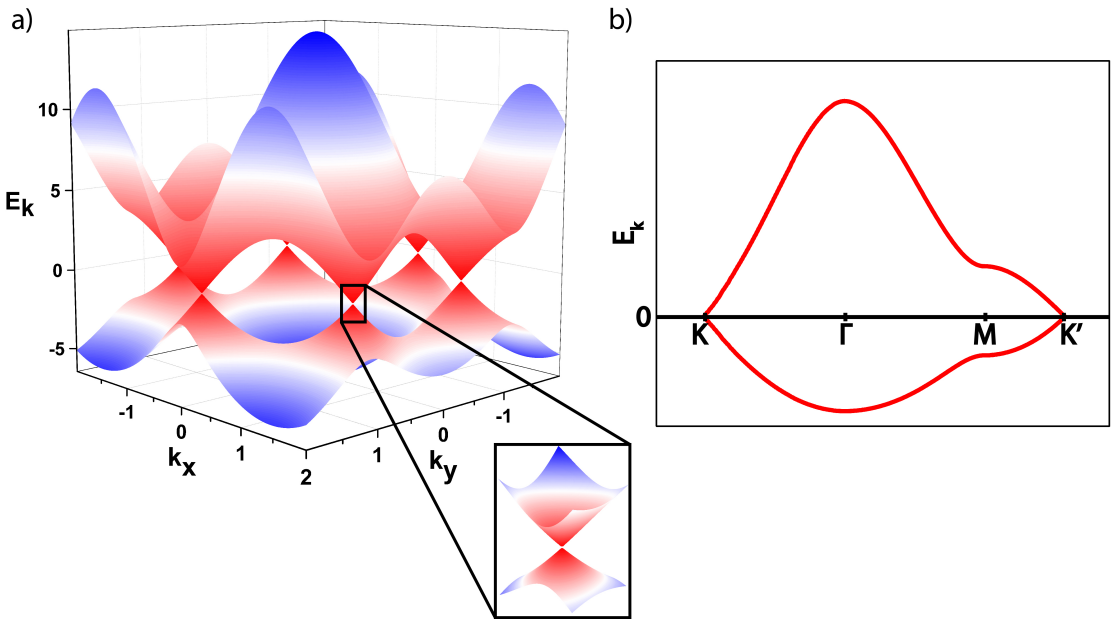

Figure 2.2: The band structure of monolayer graphene given by the nearest neighbour tight-binding approximation. (a) 3D plot of the band structure, band structure becomes linear in the vicinity of K point where the zoomed part is. Six points at E = 0 construct the hexagonal structure of Brillouin zone. (b) A vector line is cut though from the band structure as K $\rightarrow$ Γ $\rightarrow$ M $\rightarrow$ K' showing the dispersion relation at these points.

At the K point of the Brillouin zone, f(k) falls to zero due to the zero-band gap structure. A linear dispersion relation can be obtained in this part of the band structure. The Taylor expansion can be applied on f(k) in order to find the dispersion relation close to the Dirac point [5]. Therefore,

$$f(k) = f(k_0) + (x - x_0)\frac{df}{dx} + (y - y_0)\frac{df}{dy} + ... \tag{2.19}$$

with

$$\frac{df}{dk_x} = e^{ik_x a/\sqrt{2}} + 2e^{-ik_x a/2\sqrt{3}} cos(\frac{k_y a}{2}), \qquad \frac{df}{dk_y} = -ae^{-ik_x a/2\sqrt{3}} sin(\frac{k_y a}{2}). \tag{2.20}$$

$$f(k) = f(k_0) + (x - x_0)(e^{ik_x a/\sqrt{2}} + 2e^{-ik_x a/2\sqrt{3}} cos(\frac{k_y a}{2})) + \tag{2.21}$$

$$+ (y - y_0)(-ae^{-ik_x a/2\sqrt{3}} sin(\frac{k_y a}{2})) + ... \tag{2.22}$$

The position of K can be taken as

$$K = (0, \frac{4\pi}{3\sqrt{3}a_{c-c}}) \qquad \text{which is} \qquad K = (0, -\frac{4\pi}{3a}) \qquad \text{and} \qquad K' = (0, \frac{4\pi}{3a}). \tag{2.23}$$

For K and K' , $f(k)$ can be written as

$$f(k) \approx \frac{3a}{2\sqrt{3}}(ik_x \mp k_y). \tag{2.24}$$

and

$$H_{K,K'} = \frac{3at}{2\sqrt{3}} \begin{pmatrix} 0 & ik_x \mp k_y \\ -ik_x \mp k_y & 0 \end{pmatrix}. \tag{2.25}$$

Solving the equation $\det(H - EI) = 0$ where I is an identity matrix and s = 0 around E = ε_{2p},

$$E_k = \pm\frac{3at}{2\sqrt{3}}\sqrt{k_x^2 + k_y^2} \tag{2.26}$$

and

$$E_k = \pm\upsilon_F|\mathbf{k}| \tag{2.27}$$

where the Fermi velocity, $\upsilon_F = 10^6$ m/s, is the electron velocity at the K-points. This linear dispersion relation is governed by electrons known as massless Dirac fermions [6]. This approximation is only valid for energies much smaller than the nearest neighbour hopping energy.

2.2 Transition metal dichalcogenides (TMDCs)

Graphene is not the only two-dimensional material in nature. Transition metal dichalcogenides are also atomically thin and they possess very different properties compared to graphene [7, 8]. Their chemical formula is MX_2 where M is a transition metal atom from the group IV, V or VI of the periodic table of elements. X is a chalcogen atom such as sulphur (S), selenium (Se) and tellurium (Te) atoms. M is sandwiched between two X atoms and bonded with a covalent bond forming X-

M-X structure, see Figure 2.3a. They contain trigonal-prismatic and octahedral molecular geometry [9].

Similarly to graphene, stacked layers of TMDCs are held together with van der Waals forces and can be isolated easily by mechanical exfoliation or obtained by chemical growth methods, see Chapter 3. They can hold metallic, semiconducting and superconducting properties. Additionally, they have high stable, non-reactive surface due to the absence of dangling bonds and high thermal stability [7, 10].

MoS_2 and WS_2 are the most studied semiconducting TMDCs due to their stability in air and the absence of dangling bonds on their surface. They have many applications in industrial dry and solid film lubricant and surface protection [11]. MoS_2 and WS_2 have trigonal-prismatic and octahedral crystal structure [12]. For semiconducting WS_2, the vertical distance between tungsten atoms is 6.07 Å, and the distance between S atoms is 3.18 Å, see Figure 2.3b [13].

These TMDCs have hexagonal (2H), tetragonal (1T) or rhombohedral (3R) symmetry repetition of two layers, one layer and three layers per unit respectively [14]. 2H and 3R symmetric MoS_2 and WS_2 show semiconducting behaviour, however, crystals with 1T symmetry are metallic.

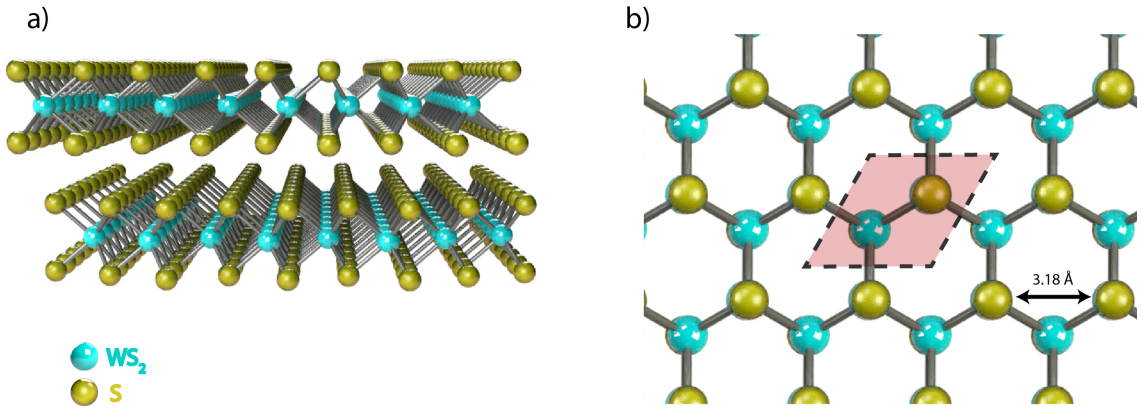

Figure 2.3: (a) AB stacked bilayer WS_2, tungsten atoms are sandwiched between sulphur atoms. (b) Top view of the WS_2, the shaded area with dashed lines represents the primitive unit cell.

The band gaps of bulk 2H geometries of MoS_2 and WS_2 are indirect. Unlike graphene, the energy dispersion of TMDCs presents a direct energy gap at the K point of the Brillouin zone. For bulk WS_2, the indirect band gap occurs between

the valence band peak at the Γ point of the Brillouin zone and conduction band between K and Γ points on the conduction band, see Figure 2.4a.

Perpendicular quantum confinement, hybridisation of p_z orbitals on S atoms and d orbitals of Mo or W atoms cause a change in the band structure with the number of layers [14–16]. Strongly localised d orbitals dominate the conduction band states at the K point [16]. States near the Γ point originate from the linear combination of d orbitals on Mo atoms and anti-bonding of p_z orbitals on S atoms which have high interlayer coupling and contribute to the formation of the indirect band gap from the monolayer to multilayer MoS_2 [10, 16, 17]. Upon decreasing the number of layers, the energies corresponding to the anti-bonding states, Γ, are reduced resulting in a large direct band gap in the monolayers [17]. The minimum point of the conduction band approaches the K point with decreasing thickness, see Figure 2.4a and b. Finally, the direct band gap becomes smaller than the indirect band gap situated at the K point with a band gap of 2.1 eV in WS_2 [18]. The large band gap provides opportunities to study optoelectronic properties of these materials in the visible and infrared region of the electromagnetic spectrum, see Chapter 6.

MoS_2 and WS_2 have strong spin-orbit interaction, and their inversion symmetry is broken for odd-numbered atomic layers, see Figure 2.5b. The two sublattices are occupied by two sulphur atoms and a molybdenum or a tungsten atom [20]. Spin-up and spin-down states are degenerate at K and K' points on the conduction band [21]. These degenerate states are separated by a spin-orbit splitting on the valence band resulting in a gap between spin-up and -down states due to the strong spin-orbit coupling from the d-orbital of the metal atom and interlayer hopping in multilayer (even number of layers) TMDCs, see Figure 2.5a [22, 23]. Size and effective mass difference between TMDCs cause various spin-orbit splitting [24, 25]. It is ~ 0.16 eV and ~ 0.4 eV for MoS_2 and WS_2 respectively [20, 22, 24]. Because of the spin-orbit splitting, the lower valence band transitions can be observed in the optical measurements [22, 23].

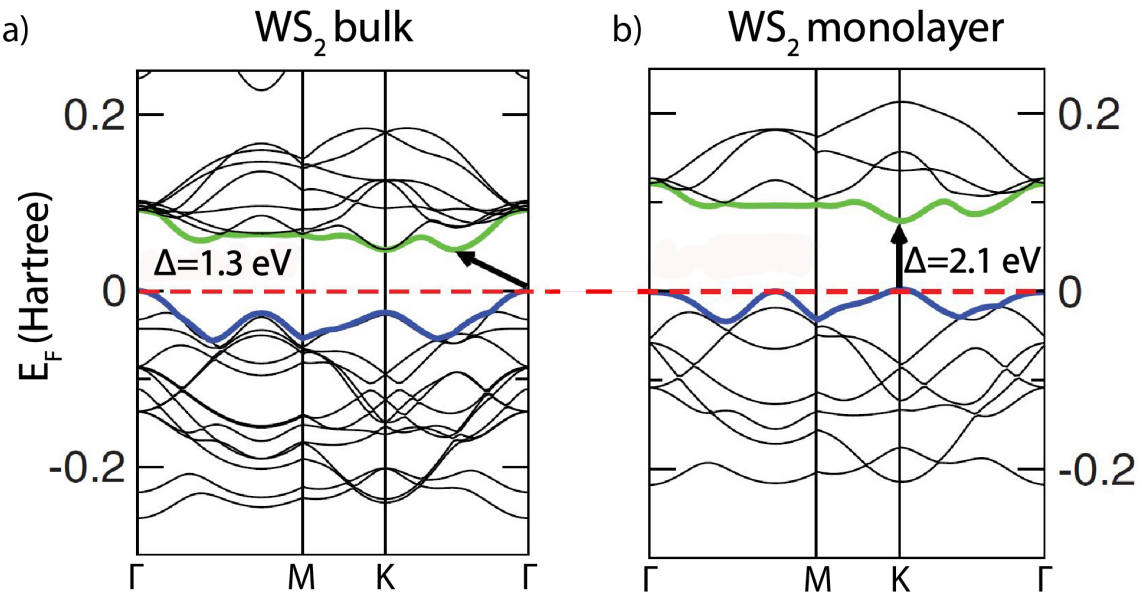

Figure 2.4: (a) Band structure of bulk WS_2 and (b) band structure of monolayer WS_2, adapted from [18] where the Hartree energy, $1E_h = 27.2$ eV [19]. Red horizontal dashed lines are the Fermi level. The indirect and the direct band gaps are shown with arrows. The green line represents the conduction band minimum whereas the blue line indicates the valence band maximum.

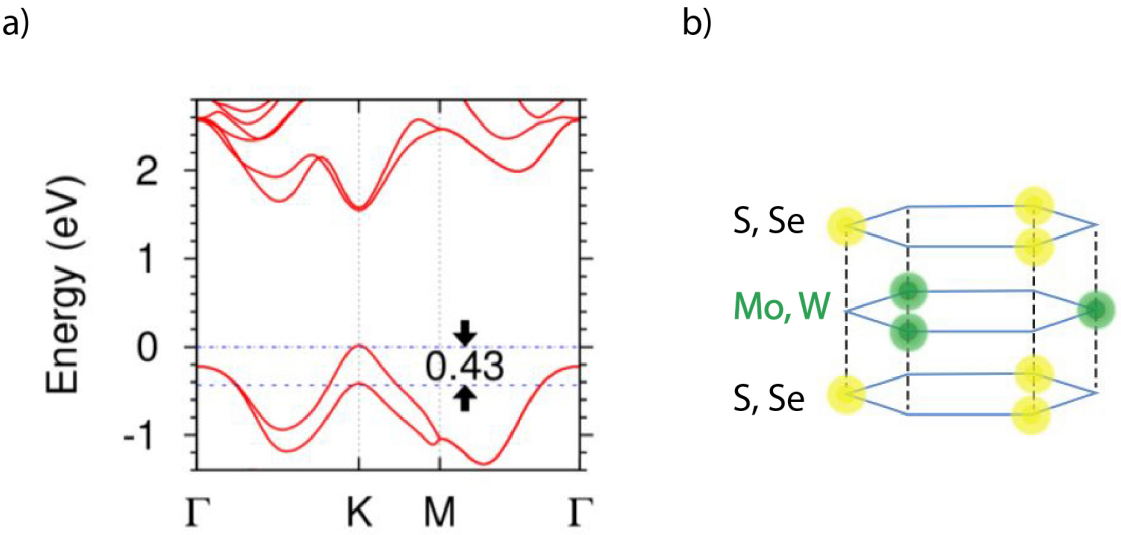

Figure 2.5: (a) Ab initio calculated band structure of monolayer WS_2, the splitting of the valence band is 0.43 eV, adapted from [22]. (b) Trigonal prismatic structure of monolayer WS_2 with broken immersion symmetry, adapted from [21].

2.3 Graphene-semiconducting TMDC heterostructures

Graphene has attracted enormous interest by a wide scientific community due to an unprecedented combination of properties including record-high room temperature charge carrier mobility, extreme mechanical flexibility and optical transparency [26–29]. However, this carbon material suffers from the lack of a band gap and therefore, it is not suitable for semiconductor technology [7]. On the other hand, atomically thin TMDCs have an energy gap. The development of real life applications based on the semiconducting properties of TMDCs faces multiple challenges, such as a low charge carrier mobility and high contact resistance at the metal/TMDCs interface. Hybrid structures of graphene and TMDCs can overcome some of the aforementioned limitations leading to a new generation of opto-electronic devices, see Figure 2.6 [30, 31]. In this thesis, the optical properties of WS_2 and the outstanding electrical properties of graphene are explored to pioneer a new class of highly efficient photodetectors. It is also shown that TMDCs can act as a tunnel barrier assisting tunnelling field-effect transistors and a Schottky barrier can be established at the junction [32–34].

The electron affinity of MoS_2 and graphene is given in Figure 2.7a along with the work function of highly p-doped Si. When MoS_2 and graphene are brought together, a built-in electric field occurs in the depletion region due to the accumulation of electrons from the semiconductor to the semi-metal. The Fermi levels subsequently align, establishing a potential barrier (ϕ_b) in the depletion region called a Schottky barrier, see Figure 2.7b. If the Si gate is biased positively, the barrier is reduced inducing the electrons to the graphene and decreasing its Fermi level, see Figure 2.7c. On the other hand, under a negative gate bias, the Schottky barrier raises inducing holes to the graphene and the Fermi level is increased, see Figure 2.7d.

In structures such as MoS_2-graphene-MoS_2, the injection of electrons into graphene reduces the Schottky barrier between MoS_2 and graphene, increasing the Fermi level.

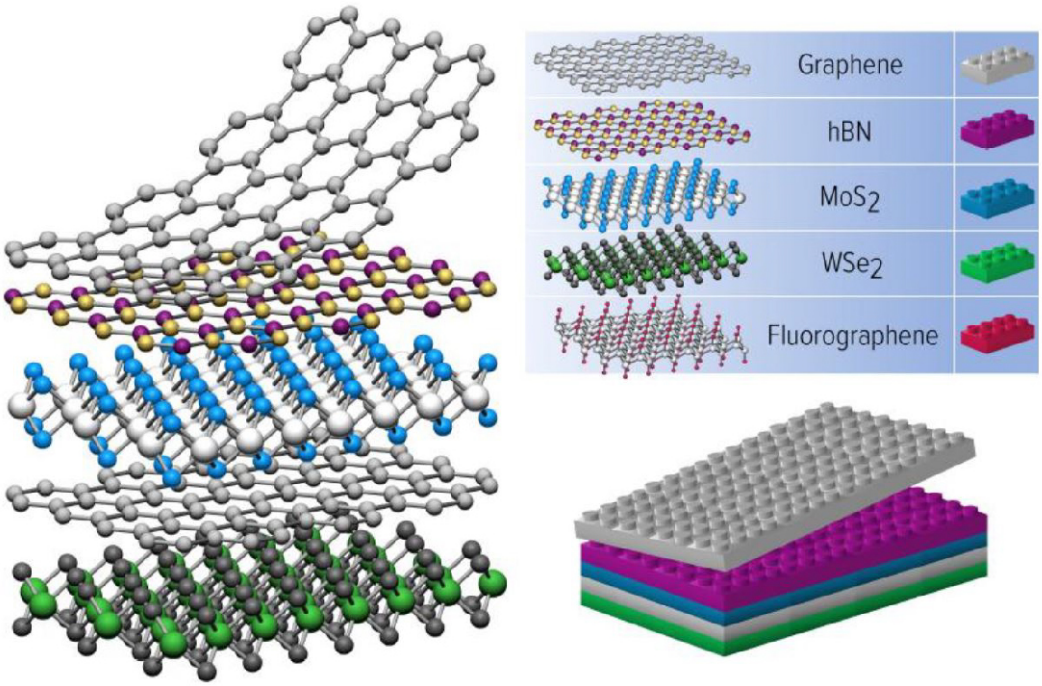

Figure 2.6: Van der Waals heterostructures: Atomically thin materials can be constructed as Lego blocks, adapted from [35].

The current passing through the channel can be adjusted by the gate bias [36]. The energy barrier existing between MoS_2 and graphene at low and large gate biases is given as ψ_{R1} and ψ_{R2} respectively, see Figure 2.8a and b.

Finally, a semiconducting TMDC can be used as a tunnelling barrier between two graphene layers [33], see Figure 2.9. In these structures, the tunnel barrier between the graphene layers increases as the gate bias is switched down to a negative voltage. On the contrary, a positive gate bias shifts the Fermi level into the conduction band which might turn on the semiconductor TMDC resulting in ON state currents. Charge carriers can penetrate to the top of the graphene due to the weak screening of the monolayer graphene and high electric field from the gate electrode [33].

Other combinations of two-dimensional materials are possible and it is presently inspiring a wide breadth of research including integrated circuits [37], memory cells [38], tunnelling field-effect transistors [33, 39].

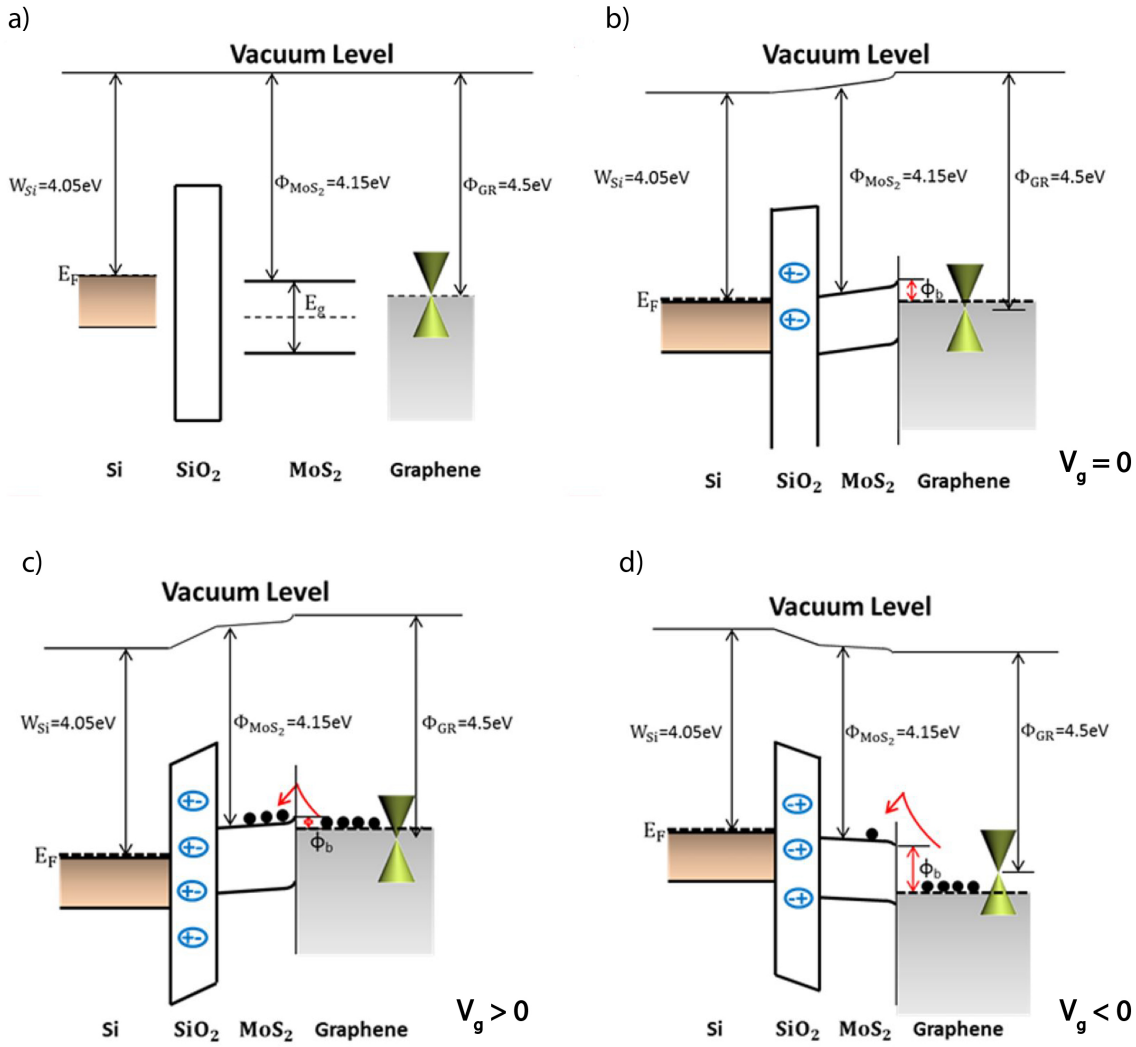

Figure 2.7: The energy band alignments of a graphene-MoS_2 heterojunction and MoS_2-graphene-MoS_2. (a) Energy band diagram of $Si/SiO_2/MoS_2$/graphene. (b) Band bending in MoS_2 nearby the contact at zero gate bias, $V_g = 0$, (c) energy-band diagram with a positive gate bias (d) and a negative gate bias, adapted from [36].

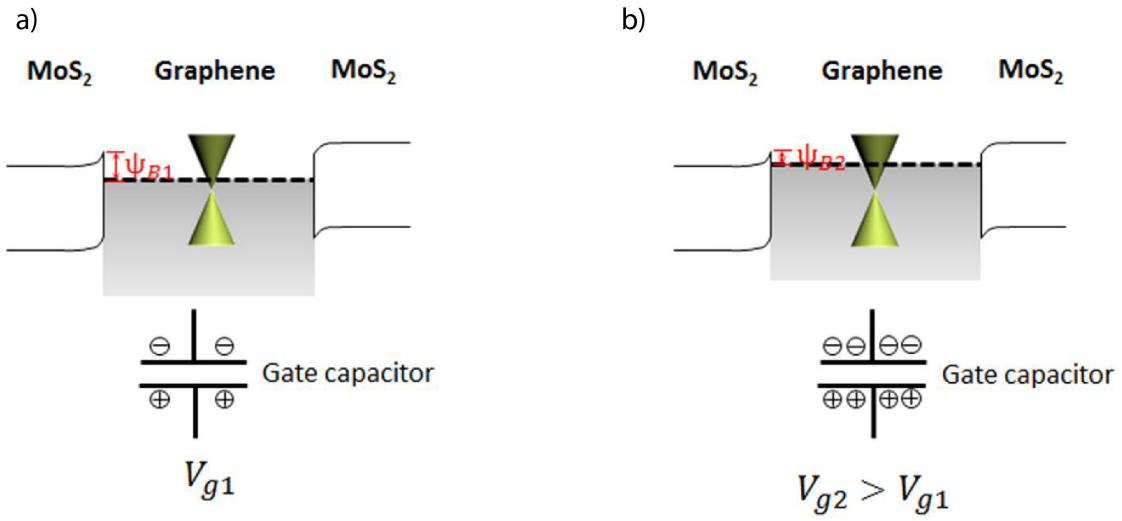

Figure 2.8: (a) Energy-band diagram for a MoS_2-graphene-MoS_2 heterostructure under a small gate voltage, V_{g1} and (b) a large gate bias, V_{g2}, adapted from [36].

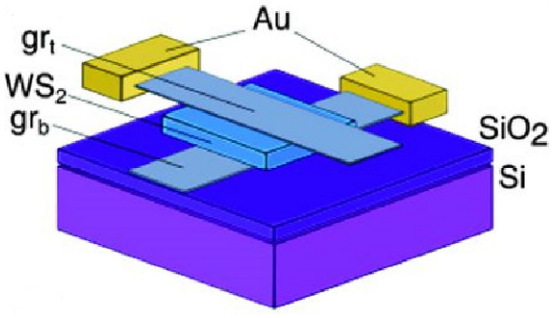

Figure 2.9: Schematic of a graphene-WS_2-graphene heterostructure device, gr_t and gr_b are the top and bottom graphene layers respectively, adapted from [32].

2.4 Photocurrent generation and mechanisms in two-dimensional materials

2.4.1 Absorption of a photon

When a material is illuminated by a light source, absorption, transmission or reflection might occur. Photodetection mechanisms in semiconductors are dependent on the absorption process. An incoming photon with an energy higher than the energy band gap of the semiconductor ($E_{ph} > E_{bg}$) transmits its energy to an electron in the valence band. In a direct band gap semiconductor, this interband transition process occurs as the electron is excited to the empty states in the conduction band, and a hole or unoccupied state is left in the valence band, see Figure 2.10a. In this case, no momentum is needed to excite an electron to the upper bands. In an indirect band gap semiconductor, the minimum of the conduction band and the valence band maximum are at the different momentum zones. Therefore, the excited electron not only requires an incoming photon of energy higher than the band gap but it also requires a sufficient input of momentum to enable the indirect transition, see Figure 2.10b [40]. This process can be assisted by phonon absorption from the lattice of the semiconductor.

The formation of an electron-hole (e-h) pair upon absorption of a photon is one of the possible light-matter interaction processes. In this case, the Coulomb interaction between the excited electron and the hole in the valence band can attract the two charges forming an e-h pair known as an exciton. Strong excitonic effects occur in the absorption of TMDCs and they play an important role in TMDC based photodetectors, see Chapter 6.

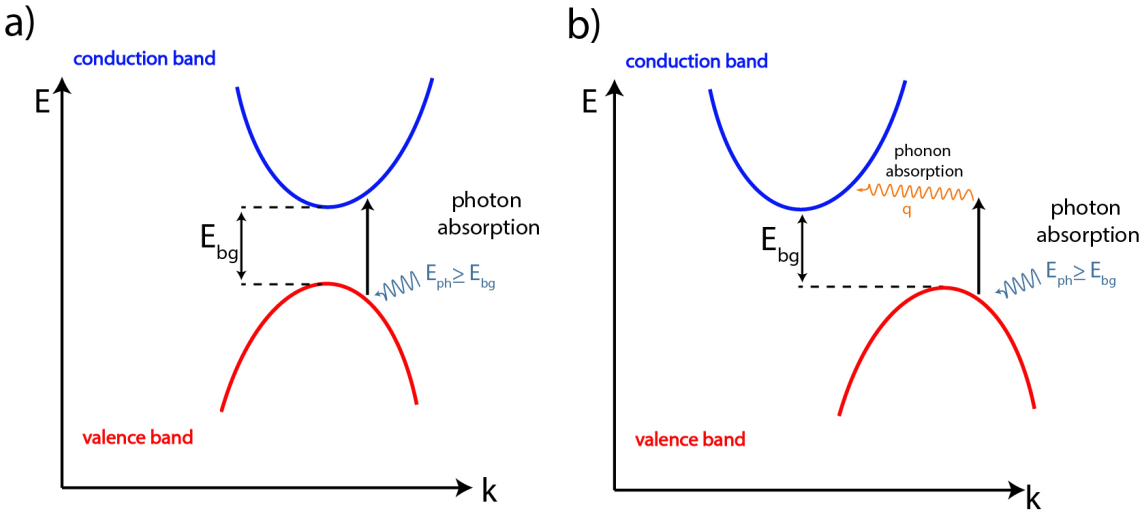

Figure 2.10: Interband photon absorption transitions in semiconductors: (a) direct band gap and (b) indirect band gap. The vertical line represents photon absorption in the band gap, the wiggly orange arrow represents phonon absorption processes for the indirect band gap. E_{bg} is the band gap of the semiconductor, E_{ph} is the photon energy and q is the electron momentum required to reach the indirect band gap.

2.4.2 Key points in photodetectors

Photoresponsivity

Upon absorption of a photon, the photogenerated carriers at energies higher than the band gap of a semiconductor can contribute towards conduction, changing the conductance of a device. Experimentally, the contribution due to the photogenerated carriers is defined as the photocurrent (I_{ph})

$$I_{ph} = I_{illumination} - I_{dark} \tag{2.28}$$

where $I_{illumination}$ is the current due to the photon illumination and I_{dark} is the current in the dark condition.

The photoresponsivity is given as photocurrent generated per unit of incident optical power. This is one of the main parameters widely used to characterise the performance of photodetectors. The photoresponsivity (A/W) and voltage responsivity (V/W) are

$$R_I = \frac{I_{ph}}{P_{opt}} \qquad \text{and} \qquad R_V = \frac{V_{ph}}{P_{opt}} \tag{2.29}$$

where P_{opt} is the total optical power and V_{ph} is the photoinduced voltage.

Spectral responsivity

In general, the photoresponsivity is a parameter which depends on the wavelength of the light shone onto the material of choice. The spectral range of a photodetector is limited by the excitation energy of the photons, the band gap and the defect states of the semiconductor. The spectral responsivity of a photodetector is defined by measuring the photocurrent or photovoltage responsivity at different wavelengths which can be written as

$$R(\lambda) = \frac{I_{ph}(\lambda)}{P_{opt}(\lambda)} \tag{2.30}$$

where $I_{ph}(\lambda)$ is the photocurrent, $P_{opt}(\lambda)$ is the optical power at a given wavelength and λ is the excitation wavelength. The spectral responsivity can provide information about the photon-semiconductor interaction. For example, the spectral responsivity of graphene and TMDC devices on a Si/SiO_2 substrate can strongly depend on the absorption spectrum of the device due to the thickness of the oxide layer and reflections between Si and SiO_2 [41]. As a result of this, energies of defect states, excitonic interactions and band gap of a semiconductor can be studied.

External quantum efficiency

The external quantum efficiency (EQE) is the number of charge carriers which contribute towards photocurrent generation per total number of incident photons. The EQE can be written as

$$\text{EQE} = \frac{n_e}{n_{photon}^{total}} = \frac{I_{ph}/e}{P_{opt}/h\nu} = R_I \frac{hc}{e\lambda} \tag{2.31}$$

where e is the charge of the electron, h is the Plank constant, c is the speed of light, ν is the frequency of incident light and λ is the photon wavelength [42].

The EQE is usually in the range of 0 to 100%. However, internal effects can result in an EQE exceeding 100%. For example, if one charge type (e.g. hole) is

trapped, it is in some cases feasible to let the other charge type (electron) travel multiple times through the device. If the trapped charge lifetime is much longer than the transit time of the free carriers, a net gain is observed [43]. This can result in EQE values as high as 10^6%, see Chapter 6.

Internal quantum efficiency

Similar to the EQE, the internal quantum efficiency (IQE) can be given as the ratio between the number of measured photogenerated charge carriers (n_e) and the number of absorbed photons (n_{abs}) which is

$$\text{IQE} = \frac{n_e}{n_{abs}}. \tag{2.32}$$

This can be rewritten as

$$\text{IQE} = \frac{I_{ph}}{e\phi_{abs}} \tag{2.33}$$

where I_{ph} is the photocurrent, e is the electron charge and ϕ_{abs} is the number of absorbed photons. The IQE depends on photocurrent generation mechanism and the absorption coefficient. The number of absorbed photons can be determined by the difference between the total number of incident photons and photon losses in transmission and reflection processes.

Response time

The response time defines how fast a photodetector responses to the illumination. The rise (fall) time is the response time when the light is turned on (off). 10% offset time is usually given when the response time is measured for both fall and rise times. A photodetector requires fast response times in order to be used in optoelectronic applications such as high-speed integrated data communication systems and video-rate imaging [44].

Bandwidth

The bandwidth of a photodetector is defined by the light modulation frequency difference between the lowest and the highest cutoff frequencies. -3 dB bandwidth is given by the frequency where the square of the output electrical power of the device drop by 50% of its maximum value, $R^2(f_{-3dB}) = R^2(0)/2$ [45]. -3 dB frequency can be calculated as

$$f_{-3dB} = \frac{0.35}{\tau} \tag{2.34}$$

where τ is the rise time of the device [45]. 0.35 fraction is due to the 10% offset of the response time and RC circuit shape bandwidth. This corresponds to the point where the photocurrent is reduced by a factor of $\sqrt{2}$.

Noise-equivalent power (NEP)

The noise-equivalent power is the minimum detectable illumination power, a photodetector can resolve. This can also be defined as the optical power signal which produces a signal-to-noise ratio 1 at 1 Hz bandwidth. The NEP corresponds to the sensitivity of the photodetector which is given in $W/\sqrt{Hz}$. It can be calculated as

$$\text{NEP} = \frac{P_{min}}{\sqrt{BW}} \tag{2.35}$$

where P_{min} is the minimum detectable power or the power corresponds to a signal-to-noise ratio equal to 1 and BW is the measured bandwidth. NEP is the minimum limit of the detector sensitivity.

Detectivity

The detectivity is the active area (A) on which the NEP has an effect on, and it is given by

$$D^* = \frac{\sqrt{A}}{\text{NEP}}. \tag{2.36}$$

If the NEP is defined independently from the bandwidth, then the detectivity can be written as

$$D^* = \frac{\sqrt{A * BW}}{\text{NEP}} \tag{2.37}$$

where A is the active area and BW is the bandwidth of the photodetector. The detectivity is measured in cm $\sqrt{Hz}$ W^{-1} = 1 Jones. The different photoactive areas can be compared with this parameter.

2.4.3 Photocurrent generation mechanisms

In this section, the photocurrent generation mechanisms in graphene and semiconducting TMDCs will be discussed. Photogeneration of charge carriers in these devices is dominated by photoconductive effect, photovoltaic effect, photo-thermoelectric effect and bolometric effect which will be defined in this thesis.

Photoconductive effect

Photons which have higher energy than the band gap of a semiconductor can be absorbed and generate free carriers in the conduction (electrons) and/or valence (holes) bands. In the presence of charge trap states, one of the two photoexcited type of charges can be localised while the other remains delocalised in the energy band (valence or conduction). Upon applying an external source-drain bias, the photoexcited carrier which is in the conduction (valence) band assists the flow of the electrical current in the material.

In photogating effect, a light-induced change in carrier density of graphene governs the photogeneration [42]. An electron-hole pair is generated in graphene or in a semiconductor in the vicinity of the graphene. One of the two charges is trapped in charge traps, molecules or in the conduction or the valence band of the semiconductor [46]. The other charge circulates between the source and drain under a gate bias [42, 47].

In photoconductive and photogating effect, an increase in conductivity of the semiconductor or graphene upon illumination is measured. If the relaxation time

of the photoexcited carrier in the charge trap state is much longer than the transit time of the free carrier, it is possible to recirculate the free carrier multiple times. This gain mechanism can increase the values of the EQE to well above 100%. The photoconductive gain can be expressed as

$$G = \frac{\tau_{carrier}}{\tau_{transit}} = \frac{\tau_{carrier}\mu V_{sd}}{L^2} \tag{2.38}$$

where $\tau_{carrier}$ is the lifetime of a trapped charge or the lifetime of photoexcited carriers, $\tau_{transit}$ is carrier drift time to the electrodes, μ is the mobility of the semiconductor, V_{sd} is the external bias to drift carriers between two electrodes and L is the distance between electrodes [48]. Large $\tau_{carrier}$ can increase the gain, however, it reduces the response time and bandwidth due to slow recombination times which prevents these devices from being used in video imaging applications [42, 48].

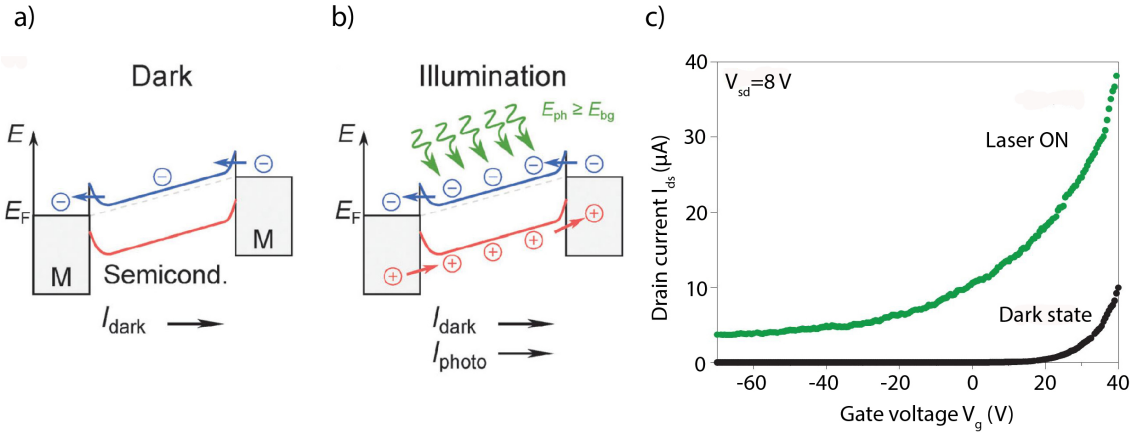

Figure 2.11: (a) Band alignment between metals (M) and a semiconductor with an external V_{sd} source-drain bias before illumination and (b) under illumination, adapted from [49]. I_{dark} and I_{photo} are the dark current and photocurrent with the addition of dark current. E_F is the Fermi level. (c) Gate sweep of the single-layer MoS_2 photodetector under 8 V source-drain bias, adapted from [50]. The black curve represents the dark current and the green line is the current under illumination (I_{photo}). The semiconductor stays in the OFF state up to 22 V. However, the laser illumination turns the device on at lower currents and increases the current in the circuit [50].

Photovoltaic effect

Unlike the photoconductive effect, the photovoltaic effect is based on the built-in electric field in the photodetector which sets apart the electron-hole pairs in opposite directions where the electrodes are located. There is no external bias required, so the dark current can be minimised. This built-in electric field can either be generated by a p-n junction or a Schottky barrier. A large depletion region occurs between the Fermi levels in the p-n junction or a semiconductor and metal which boosts the built-in electric field. The built-in field transmits the electron-hole pairs to each end of the channel, see Figure 2.12a. Reverse bias can be applied to increase the depletion region, see Figure 2.12b. With an illumination under the reverse bias, large built-in field reduces the carrier drift time.

In general, the inorganic semiconductor photodiodes show exponential I - V, source-drain curve depending on $I_{sd} \sim exp(V_{sd}) - I_{dark}$ where I_{sd} and V_{sd} the source-drain current and voltage, and I_{dark} is the dark current at reverse bias, see Figure 2.12b.

Due to the semi-metallic nature of graphene, the photovoltaic effect manifests itself differently than in the case of conventional semiconductor p-n junctions. Gradients in electrochemical potential may be generated at the lateral interfaces of graphene regions which are electrostatically or chemically doped to differing extents. Figure 2.12c and d show the photocurrent generated by the photovoltaic effect with modulation of the Fermi level in a graphene transistor with a split gate structure. The photocurrent can be written as $I_{PV} \propto (\tan^{-1}(\mu_1) - \tan^{-1}(\mu_2))$ where μ_1 and μ_2 are the chemical potentials of the two independently gated regions [51]. If the gate voltage of either region is independently swept, a map can be produced detailing the photocurrent generated as a function of chemical potential either side of the lateral interface. The maximum photocurrent is produced when μ_1 and μ_2 have opposite signs which establishes a p-n junction [51].

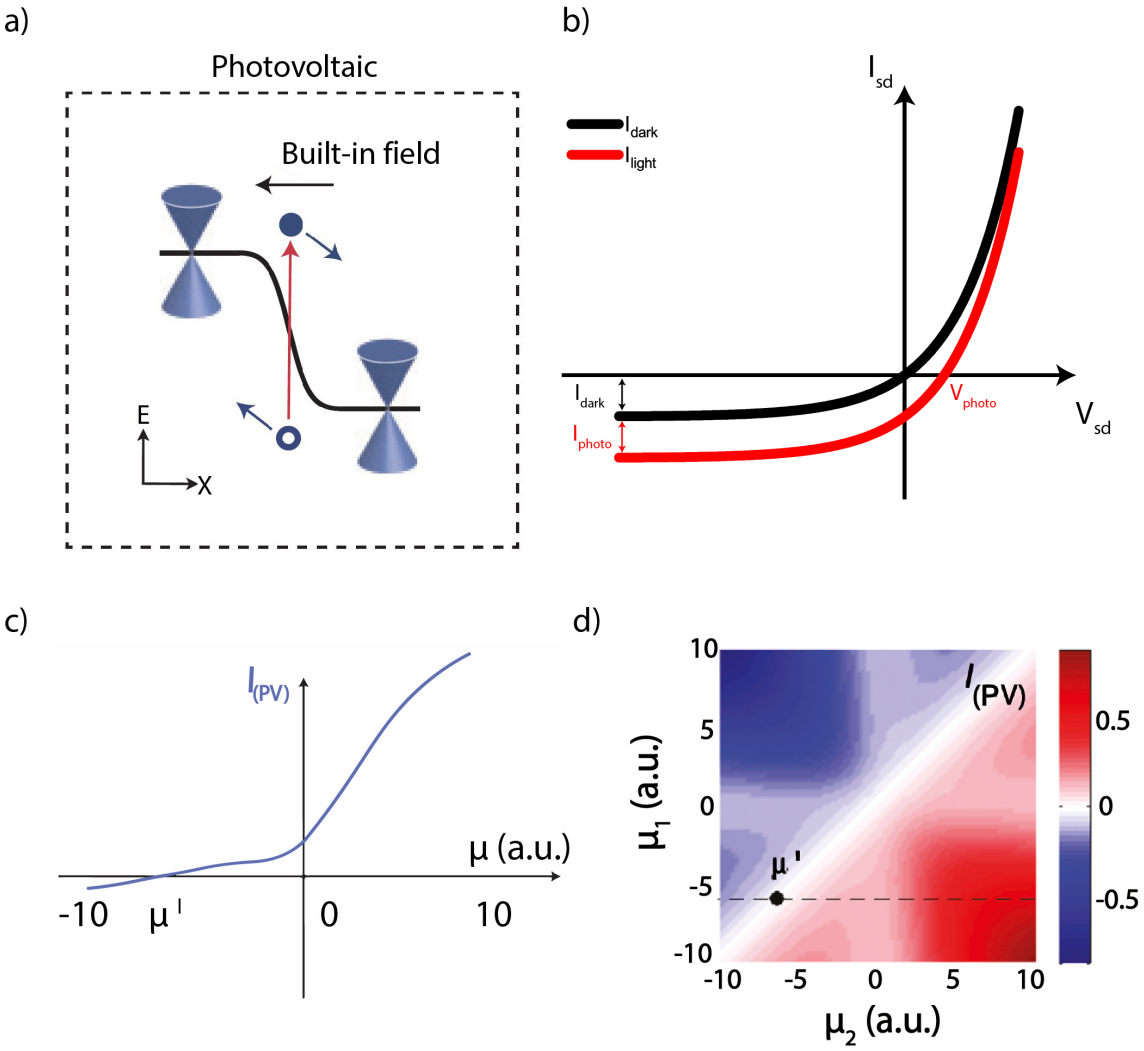

Figure 2.12: (a) Representation of the photovoltaic effect, adapted from [42]. The conic shapes show n and p-type graphene. Open and closed circles represent hole and electron separation due to the electric field. (b) I - V plot of an inorganic semiconductor photodiode representing $exp(V_{sd}) - I_{dark}$. (c) Theoretical model of the photocurrent produced due to the photovoltaic effect as a function of the chemical potential on one side of a dual-gated graphene junction, adapted from [51]. (d) Photocurrent produced by the photovoltaic effect as a function of the chemical potential either side of a dual-gated monolayer graphene junction obtained from theoretical calculation, adapted from [51].

Photo-thermoelectric effect

Another phenomenon leading to the generation of free charge carriers upon illumination is the photo-thermoelectric effect. In this case, the light shone onto the sample can lead to heating. If the device is formed by materials with different thermal conductivity, it is possible to attain steep temperature gradients. Hence, through the Seebeck effect, a voltage difference is generated upon attaining a temperature difference. At the interface between two regions of graphene with different Seebeck coefficient (S) the generated photo-thermal voltage is given by

$$V_{PTE} = (S_1 - S_2)\Delta T \tag{2.39}$$

where ΔT is the difference between average electron temperature in the lattice and the lattice temperature.

In a non-interacting model, the Seebeck coefficient is a function of the density of states of the different materials as expressed by the Mott relation [52]

$$S = -\frac{\pi^2 k_B^2 T}{3|e|}\frac{dG}{GdV_g}\frac{dV_g}{dE}\Big|_{E=E_F} \tag{2.40}$$

where G is the electrical conductivity, e is the electron charge, k_B is the Boltzmann constant and E is the energy of the system [53]. For graphene, $\frac{dV_g}{dE}$ is evaluated at the Fermi energy which is $E_f = \hbar\nu_F(\pi n)^{1/2}$ where $\hbar$ is the Plank constant, ν_F is the Fermi velocity and n is the charge density [54, 55].

In graphene, the photo-thermoelectric effect plays a dominant role due to absence of energy gap and the small enough Fermi surface which freezes out optical phonons and high energy acoustic phonons [56]. Electrons are excited from the valence band to the conduction band and they quickly relax back to the Fermi level forming a hot Fermion gas [55, 57]. The photoactive interface is formed due to the difference in density of states of regions with different doping levels. Between single and bilayer junction of the graphene, the hot carriers diffuse into the bilayer due to its larger density of states and the temperature gradient between these two materials [55].

A junction between a metal and a semiconductor can drive photocurrent due to the difference between Seebeck coefficients. The metal has much lower Seebeck coefficient than semiconductors. Therefore, generated photocurrent can be written as

$$\Delta V_{PTE} = S_{sc}.\Delta T \tag{2.41}$$

where S_{sc} is the Seebeck coefficient of the semiconductor. The photocurrent only depends on the Seebeck coefficient of the semiconductor here. This scenario has been experimentally demonstrated at the interface of pristine/heavily doped graphene [57].

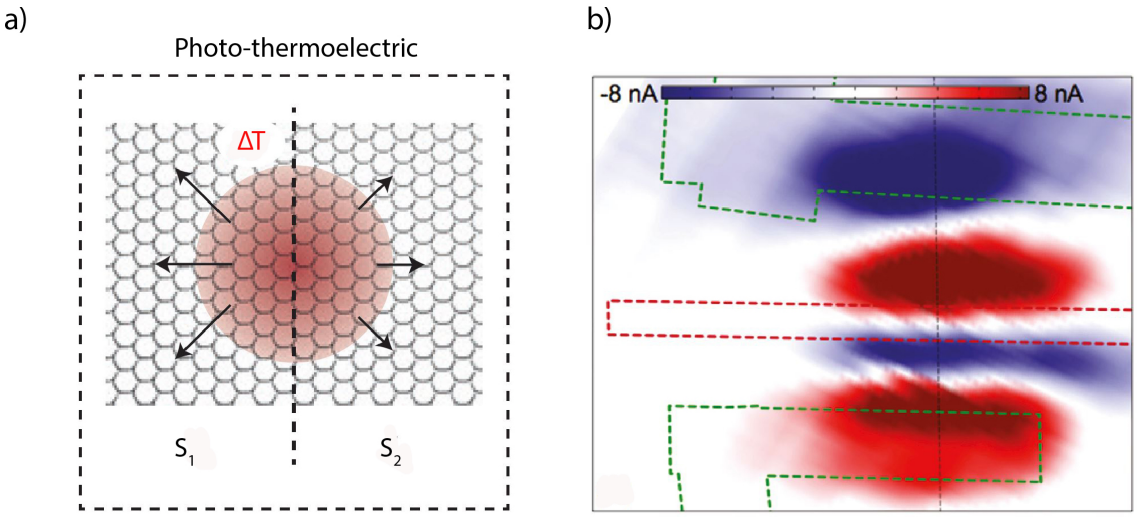

Figure 2.13: (a) Schematic representation of the photo-thermoelectric effect, adapted from [42]. Temperature distribution on the surface is shown as red area and ΔT is the elevation of the electron temperature on the lattice. S_1 and S_2 are Seebeck coefficients of two regions. (b) Scanning photocurrent microscopy map of graphene with a top gate (red dashed line), adapted from [58]. Green dashed lines represent source and drain contacts. The photocurrent increases close to the contacts due to the charge carrier separation with band bending and the local electric field close to metal/graphene interfaces [55, 59]. Due to the lack of strong fields in the middle of the device, the photocurrent is not generated and electron-hole pairs can recombine [59]. A slight change in the doping from p to n-type produces a difference in the Seebeck coefficients resulting in high photocurrent [58, 59].

Bolometric effect

The bolometric effect is based on the change in the conductivity of a material due to homogeneous heating on the surface induced by photon absorption [42, 47, 49]. The bolometric effect is proportional to the change in the conductance of the material with the temperature. This effect can be determined by a measurement of the temperature dependence of the transport current [60]. The bolometric effect coefficient is

$$\beta = \frac{\Delta I}{\Delta T} \tag{2.42}$$

where ΔI is the change in the current and ΔT is the change in the temperature [60]. This effect has also been seen in graphene photodetectors [60, 61].

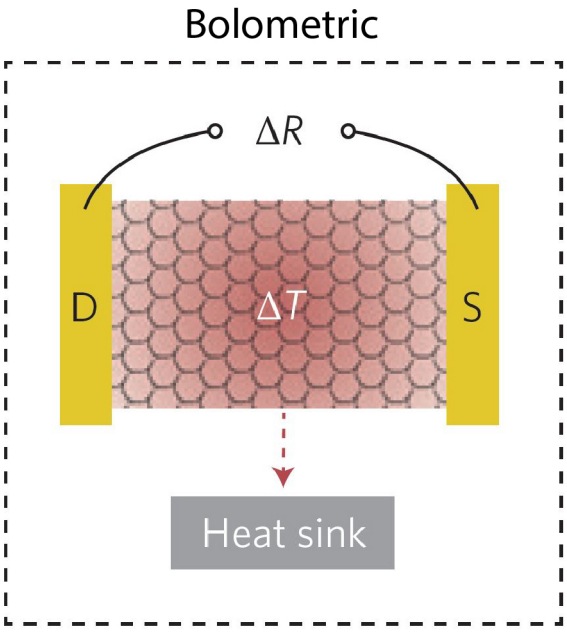

Figure 2.14: Schematic diagram of the bolometric effect, adapted from [42]. S and D represent the source and the drain electrodes. The red shaded area is the distribution of temperature and ΔT is the temperature gradient across the channel. ΔR is the difference in the resistance between source and drain.

Bibliography

[1] K. S. Novoselov, "Electric field effect in atomically thin carbon films," *Science*, vol. 306, pp. 666–669, Oct 2004.

[2] M. S. Fuhrer, C. N. Lau, and A. H. MacDonald, "Graphene: Materially better carbon," *MRS Bulletin*, vol. 35, pp. 289–295, Apr 2010.

[3] P. Wallace, "The band theory of graphite," *Physical Review*, vol. 71, pp. 622–634, May 1947.

[4] R. Saito, G. Dresselhaus, and M. S. Dresselhaus, *Physical properties of carbon nanotubes*. No. 1, Imperial College Press, 1998.

[5] T. Stroucken, J. H. Grönqvist, and S. W. Koch, "Optical response and ground state of graphene," *Physical Review B - Condensed Matter and Materials Physics*, vol. 84, no. 20, 2011.

[6] A. H. Castro Neto, N. M. R. Peres, K. S. Novoselov, and A. K. Geim, "The electronic properties of graphene," *Reviews of Modern Physics*, vol. 81, pp. 109–162, Jan 2009.

[7] B. Radisavljevic, A. Radenovic, J. Brivio, V. Giacometti, and A. Kis, "Single-layer MoS_2 transistors," *Nature Nanotechnology*, vol. 6, pp. 147–150, Mar 2011.

[8] J. Wilson and A. Yoffe, "The transition metal dichalcogenides discussion and interpretation of the observed optical, electrical and structural properties," *Advances in Physics*, vol. 18, pp. 193–335, May 1969.

[9] M. Kertesz and R. Hoffmann, "Octahedral vs. trigonal-prismatic coordination and clustering in transition-metal dichalcogenides," *Journal of the American Chemical Society*, vol. 106, pp. 3453–3460, Jun 1984.

[10] A. V. Kolobov and J. Tominaga, *Two-dimensional transition-metal dichalcogenides*, vol. 239 of *Springer Series in Materials Science*. Springer International Publishing, 2016.

[11] G. Chatzitheodorou, S. Fiechter, M. Kunst, J. Luck, and H. Tributsch, "Low temperature chemical preparation of semiconducting transition metal chalcogenide films for energy conversion and storage, lubrication and surface protection," *Materials Research Bulletin*, vol. 23, no. 9, pp. 1261–1271, 1988.

[12] R. A. Bromley, R. B. Murray, and A. D. Yoffe, "The band structures of some transition metal dichalcogenides. III. Group VIA: trigonal prism materials," *Journal of Physics C: Solid State Physics*, vol. 5, pp. 759–778, Apr 1972.

[13] A. Molina-Sánchez and L. Wirtz, "Phonons in single and few-layer MoS_2 and WS_2," *Physical Review B*, vol. 84, p. 155413, Sep 2011.

[14] Q. H. Wang, K. Kalantar-Zadeh, A. Kis, J. N. Coleman, and M. S. Strano, "Electronics and optoelectronics of two-dimensional transition metal dichalcogenides," *Nature Nanotechnology*, vol. 7, pp. 699–712, Nov 2012.

[15] K. F. Mak, C. Lee, J. Hone, J. Shan, and T. F. Heinz, "Atomically Thin MoS_2: A New Direct-Gap Semiconductor," *Physical Review Letters*, vol. 105, no. 13, p. 136805, 2010.

[16] A. Splendiani, L. Sun, Y. Zhang, T. Li, J. Kim, C. Y. Chim, G. Galli, and F. Wang, "Emerging photoluminescence in monolayer MoS_2," *Nano Letters*, vol. 10, no. 4, pp. 1271–1275, 2010.

[17] T. Li and G. Galli, "Electronic properties of MoS_2 nanoparticles," *The Journal of Physical Chemistry C*, vol. 111, no. 44, pp. 16192–16196, 2007.

[18] A. Kuc, N. Zibouche, and T. Heine, "Influence of quantum confinement on the electronic structure of the transition metal sulfide TS_2," *Physical Review B*, vol. 83, p. 245213, Jun 2011.

[19] P. J. Mohr, D. B. Newell, and B. N. Taylor, "CODATA recommended values of the fundamental physical constants: 2014," *Reviews of Modern Physics*, vol. 88, p. 035009, Sep 2016.

[20] K. F. Mak, K. He, J. Shan, and T. F. Heinz, "Control of valley polarization in monolayer MoS_2 by optical helicity," *Nature Nanotechnology*, vol. 7, no. 8, pp. 494–498, 2012.

[21] K. F. Mak and J. Shan, "Photonics and optoelectronics of 2D semiconductor transition metal dichalcogenides," *Nature Photonics*, vol. 10, no. 4, pp. 216–226, 2016.

[22] H. Zeng, G.-B. Liu, J. Dai, Y. Yan, B. Zhu, R. He, L. Xie, S. Xu, X. Chen, W. Yao, and X. Cui, "Optical signature of symmetry variations and spin-valley coupling in atomically thin tungsten dichalcogenides," *Scientific Reports*, vol. 3, p. 1608, 2013.

[23] L. Sun, J. Yan, D. Zhan, L. Liu, H. Hu, H. Li, B. K. Tay, J. L. Kuo, C. C. Huang, D. W. Hewak, P. S. Lee, and Z. X. Shen, "Spin-orbit splitting in single-layer MoS_2 revealed by triply resonant raman scattering," *Physical Review Letters*, vol. 111, no. 12, pp. 1–5, 2013.

[24] W. Zhao, Z. Ghorannevis, L. Chu, M. Toh, C. Kloc, P.-H. Tan, and G. Eda, "Evolution of electronic structure in atomically thin sheets of WS_2 and WSe_2," *ACS Nano*, vol. 7, pp. 791–797, Jan 2013.

[25] A. Kormányos, V. Zólyomi, N. D. Drummond, and G. Burkard, "Spin-orbit coupling, quantum dots, and qubits in monolayer transition metal dichalcogenides," *Physical Review X*, vol. 4, no. 1, pp. 1–16, 2014.

[26] K. I. Bolotin, K. J. Sikes, Z. Jiang, M. Klima, G. Fudenberg, J. Hone, P. Kim, and H. L. Stormer, "Ultrahigh electron mobility in suspended graphene," *Solid State Communications*, vol. 146, no. 9-10, pp. 351–355, 2008.

[27] L. Banszerus, M. Schmitz, S. Engels, J. Dauber, M. Oellers, F. Haupt, K. Watanabe, T. Taniguchi, B. Beschoten, and C. Stampfer, "Ultrahigh-mobility graphene devices from chemical vapor deposition on reusable copper," *Science Advances*, vol. 1, no. 6, pp. 1–6, 2015.

[28] R. R. Nair, P. Blake, A. N. Grigorenko, K. S. Novoselov, T. J. Booth, T. Stauber, N. M. R. Peres, and A. K. Geim, "Fine structure constant defines visual transparency of graphene," *Science*, vol. 320, pp. 1308–1308, Jun 2008.

[29] A. Shekhawat and R. O. Ritchie, "Toughness and strength of nanocrystalline graphene," *Nature Communications*, vol. 7, p. 10546, 2016.

[30] K. Roy, M. Padmanabhan, S. Goswami, T. P. Sai, G. Ramalingam, S. Raghavan, and A. Ghosh, "Graphene-MoS_2 hybrid structures for multifunctional photoresponsive memory devices," *Nature Nanotechnology*, vol. 8, pp. 826–830, Nov 2013.

[31] D. De Fazio, I. Goykhman, D. Yoon, M. Bruna, A. Eiden, S. Milana, U. Sassi, M. Barbone, D. Dumcenco, K. Marinov, A. Kis, and A. C. Ferrari, "High responsivity, large-area graphene/MoS_2 flexible photodetectors," *ACS Nano*, vol. 10, no. 9, pp. 8252–8262, 2016.

[32] L. Britnell, R. M. Ribeiro, A. Eckmann, R. Jalil, B. D. Belle, A. Mishchenko, Y.-J. Kim, R. V. Gorbachev, T. Georgiou, S. V. Morozov, A. N. Grigorenko, A. K. Geim, C. Casiraghi, A. H. Castro Neto, and K. S. Novoselov, "Strong light-matter interactions in heterostructures of atomically thin films," *Science*, vol. 340, pp. 1311–1314, Jun 2013.

[33] T. Georgiou, R. Jalil, B. D. Belle, L. Britnell, R. V. Gorbachev, S. V. Morozov, Y.-J. Kim, A. Gholinia, S. J. Haigh, O. Makarovsky, L. Eaves, L. A. Ponomarenko, A. K. Geim, K. S. Novoselov, and A. Mishchenko, "Vertical field-effect transistor based on graphene-WS_2 heterostructures for flexible and transparent electronics," *Nature Nanotechnology*, vol. 8, no. 2, pp. 100–103, 2013.

[34] T. Yamaguchi, R. Moriya, Y. Inoue, S. Morikawa, S. Masubuchi, K. Watanabe, T. Taniguchi, and T. Machida, "Tunneling transport in a few monolayer-thick WS_2/graphene heterojunction," *Applied Physics Letters*, vol. 105, no. 22, p. 223109, 2014.

[35] A. K. Geim and I. V. Grigorieva, "Van der Waals heterostructures," *Nature*, vol. 499, pp. 419–425, Jul 2013.

[36] H. Tian, Z. Tan, C. Wu, X. Wang, M. A. Mohammad, D. Xie, Y. Yang, J. Wang, L.-J. Li, J. Xu, and T.-L. Ren, "Novel field-effect Schottky barrier transistors based on graphene-MoS_2 heterojunctions," *Scientific Reports*, vol. 4, p. 5951, 2014.

[37] L. Yu, Y. H. Lee, X. Ling, E. J. G. Santos, Y. C. Shin, Y. Lin, M. Dubey, E. Kaxiras, J. Kong, H. Wang, and T. Palacios, "Graphene/MoS_2 hybrid technology for large-scale two-dimensional electronics," *Nano Letters*, vol. 14, no. 6, pp. 3055–3063, 2014.

[38] S. Bertolazzi, D. Krasnozhon, and A. Kis, "Nonvolatile memory cells based on MoS_2/graphene heterostructures," *ACS Nano*, vol. 7, no. 4, pp. 3246–3252, 2013.

[39] L. Britnell, R. V. Gorbachev, R. Jalil, B. D. Belle, F. Schedin, A. Mishchenko, T. Georgiou, M. I. Katsnelson, L. Eaves, S. V. Morozov, N. M. R. Peres, J. Leist, A. K. Geim, K. S. Novoselov, and L. A. Ponomarenko, "Field-effect tunneling transistor based on vertical graphene heterostructures," *Science*, vol. 335, no. 6071, pp. 947–950, 2012.

[40] M. Fox, *Optical Properties of Solids*. Oxford University Press, 1st ed., 2001.

[41] K. J. Tielrooij, L. Piatkowski, M. Massicotte, A. Woessner, Q. Ma, Y. Lee, K. S. Myhro, C. N. Lau, P. Jarillo-Herrero, N. F. van Hulst, and F. H. L. Koppens, "Generation of photovoltage in graphene on a femtosecond timescale through efficient carrier heating," *Nature Nanotechnology*, vol. 10, no. 5, pp. 437–443, 2015.

[42] F. H. L. Koppens, T. Mueller, P. Avouris, A. C. Ferrari, M. S. Vitiello, and M. Polini, "Photodetectors based on graphene, other two-dimensional materials and hybrid systems," *Nature Nanotechnology*, vol. 9, pp. 780–793, Oct 2014.

[43] D. Kufer and G. Konstantatos, "Photo-FETs: Phototransistors enabled by 2D and 0D nanomaterials," *ACS Photonics*, pp. 2197–2210, Oct 2016.

[44] M. Massicotte, P. Schmidt, F. Vialla, K. G. Schädler, A. Reserbat-Plantey, K. Watanabe, T. Taniguchi, K. J. Tielrooij, and F. H. L. Koppens, "Picosecond photoresponse in van der Waals heterostructures," *Nature Nanotechnology*, vol. 11, no. 1, pp. 42–46, 2015.

[45] J. Liu, *Photonic Devices*. Cambridge: Cambridge University Press, 2005.

[46] G. Konstantatos, M. Badioli, L. Gaudreau, J. Osmond, M. Bernechea, F. P. G. de Arquer, F. Gatti, and F. H. L. Koppens, "Hybrid graphene-quantum dot phototransistors with ultrahigh gain," *Nature Nanotechnology*, vol. 7, no. 6, pp. 363–368, 2012.

[47] C. Xie, C. Mak, X. Tao, and F. Yan, "Photodetectors based on two-dimensional layered materials beyond graphene," *Advanced Functional Materials*, 2016.

[48] B. E. A. Saleh and M. C. Teich, *Fundamentals of Photonics*. Wiley Series in Pure and Applied Optics, New York, USA: John Wiley & Sons, Inc., Aug 1991.

[49] M. Buscema, J. O. Island, D. J. Groenendijk, S. I. Blanter, G. A. Steele, H. S. van der Zant, and A. Castellanos-Gomez, "Photocurrent generation with two-

dimensional van der Waals semiconductors," *Chemical Society Reviews*, vol. 44, no. 11, pp. 3691–3718, 2015.

[50] O. Lopez-Sanchez, D. Lembke, M. Kayci, A. Radenovic, and A. Kis, "Ultrasensitive photodetectors based on monolayer MoS_2," *Nature Nanotechnology*, vol. 8, pp. 497–501, Jul 2013.

[51] J. C. W. Song, M. S. Rudner, C. M. Marcus, and L. S. Levitov, "Hot carrier transport and photocurrent response in graphene," *Nano Letters*, vol. 11, no. 11, pp. 4688–4692, 2011.

[52] M. Cutler and N. F. Mott, "Observation of Anderson localization in an electron gas," *Physical Review*, vol. 181, pp. 1336–1340, May 1969.

[53] Y. M. Zuev, W. Chang, and P. Kim, "Thermoelectric and magnetothermoelectric transport measurements of graphene," *Physical Review Letters*, vol. 102, no. 9, pp. 1–4, 2009.

[54] P. Wei, W. Bao, Y. Pu, C. N. Lau, and J. Shi, "Anomalous thermoelectric transport of dirac particles in graphene," *Physical Review Letters*, vol. 102, no. 16, pp. 1–4, 2009.

[55] X. Xu, N. M. Gabor, J. S. Alden, A. M. Van Der Zande, and P. L. McEuen, "Photo-thermoelectric effect at a graphene interface junction," *Nano Letters*, vol. 10, no. 2, pp. 562–566, 2010.

[56] D. K. Efetov and P. Kim, "Controlling electron-phonon interactions in graphene at ultrahigh carrier densities," *Physical Review Letters*, vol. 105, no. 25, pp. 2–5, 2010.

[57] F. Withers, T. H. Bointon, M. F. Craciun, and S. Russo, "All-graphene photodetectors," *ACS Nano*, vol. 7, pp. 5052–5057, Jun 2013.

[58] M. C. Lemme, F. H. L. Koppens, A. L. Falk, M. S. Rudner, H. Park, L. S. Levitov, and C. M. Marcus, "Gate-activated photoresponse in a graphene p-n junction," *Nano Letters*, vol. 11, no. 10, pp. 4134–4137, 2011.

[59] T. Mueller, F. Xia, M. Freitag, J. Tsang, and P. Avouris, "Role of contacts in graphene transistors: A scanning photocurrent study," *Physical Review B*, vol. 79, p. 245430, Jun 2009.

[60] M. Freitag, T. Low, F. Xia, and P. Avouris, "Photoconductivity of biased graphene," *Nature Photonics*, vol. 7, pp. 53–59, Dec 2012.

[61] J. Yan, M.-H. Kim, J. A. Elle, A. B. Sushkov, G. S. Jenkins, H. M. Milchberg, M. S. Fuhrer, and H. D. Drew, "Dual-gated bilayer graphene hot-electron bolometer," *Nature Nanotechnology*, vol. 7, no. 7, pp. 472–478, 2012.

Chapter 3

Methods and fabrication

3.1 Introduction

The fabrication of two-dimensional devices often requires high-end nano-fabrication facilities under clean room conditions, where there is a reduced number of dust particles in the air. However, for some 2D materials, a vacuum or inert gas environment is needed to avoid any oxidation on their surface. The fabrication and characterisation methods discussed in this section include graphene exfoliation, fabrication of electrical contacts, electrical transport and optoelectronic measurements of atomically thin materials.

3.2 Fabrication of devices based on two-dimensional materials

3.2.1 Mechanical exfoliation

Bulk TMDCs and graphite are formed by atomic layers weakly coupled by van der Waals forces. These interactions can be broken with a force which can be applied with an adhesive tape.

In this fabrication, a Si/SiO_2 wafer (sourced by IDB Technologies) is used as a substrate. The Si has industry grade <100> crystal orientation which is highly

p-doped with boron and has a thickness of 525 μm. This has 290 nm of thermally grown SiO_2, which serves as a back gate dielectric layer. The substrate is cleaned with ultrasound treatment in deionized (DI) water, acetone and isopropyl alcohol (IPA) solvents. Then, the SiO_2 surface is exposed to oxygen plasma to remove any organic contamination. After that, it is heated on a hot plate up to $\sim$ 80°C. A bulk graphite crystal is picked up and placed onto a blue adhesive tape, see Figure 3.1a. The crystal is thinned down by peeling off with the tape until a uniform grey surface area of about 1 cm^2 is attained, see Figure 3.1b. Subsequently, mechanical transfer of the exfoliated flakes is completed by pressing the cleaned substrate onto the grey area of the tape, see Figure 3.1c. The sample is then placed in acetone for 5 minutes to remove any residues of tape and loosely attached flakes before dipping in IPA to remove the acetone and any other organic residues, then drying with N_2 gas. Graphene flakes down to 1 μm size can be identified by 50x objective of the optical microscope, shown as Figure 3.2a. With optical contrast measurements, the number of flakes can be quantified, see Section 3.3.1.

3.2.2 Chemical vapor deposition of graphene

Chemical vapor deposition (CVD) is a material growth technique usually involving the reaction with chemical gases in a hot furnace on the surface of a substrate material. CVD can be used to fabricate large areas of high-quality graphene of the order of tens of cm (wafer size). This growth process involves exposing a copper foil to a mixture of hydrogen and methane at around 1000°C. During the reaction, methane is adsorbed on the copper, which acts as a catalyst and as a substrate for its disassociation into carbon and hydrogen. The hydrogen then desorbs from the metal, leaving carbon nucleates. The reaction is summarised by [1]

$$CH_4 + 5\text{Cu Surface} \rightleftharpoons \text{Graphene} + 2H_2. \tag{3.1}$$

Hot chamber CVD graphene growth can take more than 100 minutes which consumes large amount of gas, time and energy, increasing cost of the process.

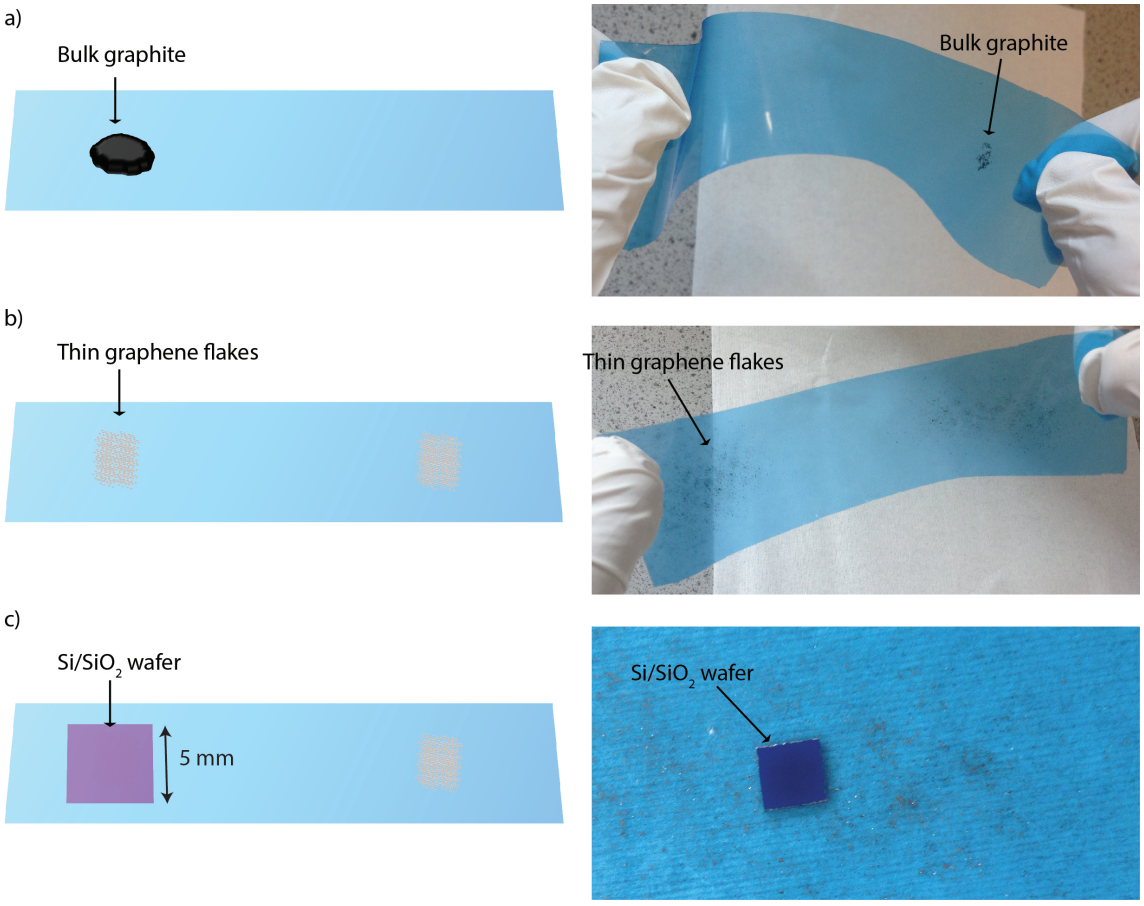

Figure 3.1: Graphene exfoliation involves placing bulk graphite onto a piece of blue tape (a), which is then peeled several times to form a thin graphite (b) before placing a warm Si/SiO_2 substrate onto the thin flakes (c).

However, Cold Wall CVD technique does not require long time gas exposures [2]. In these systems, rapid local heating of the stage can take place in a few minutes, making the system ready for growth in such a short time scale. In this thesis, I use CVD grown graphene with a commercial cold wall system (Moorfield nanoCVD-8G) which employs a resistive heating stage, a programmable gas flow and a temperature control. In most systems, the graphene on copper foil occurs in four stages: ramping up, annealing, growth and cooling [2]. First, the resistive stage is heated to 1035°C at a rate of 5.75°C/s, then copper foil is annealed for 10 minutes with a constant H_2 gas flow. Figure 3.2b shows a colour change on the copper foil before and after the growth which is due to the surface cleaning during the annealing. After that, the temperature is dropped down to 1000°C and a flow of 77.8% CH_4 and 22.2% H_2 are introduced for 40 seconds. Then, the growth is started with increasing the flow rate of CH_4 to 94.6% and reducing H_2 to 5.4%. The stage is subsequently cooled down to room temperature. This whole process takes about 23 minutes and it produces high quality graphene at low cost of cm^2 surface area [2].

3.2.3 Wet transfer method of graphene

Graphene grown on copper can be transferred to the desired substrate using standard wet transfer technique [3, 4]. Graphene growth occurs on both sides of the copper foil. Upper side of the copper is spin coated with poly-methyl methacrylate (PMMA) to protect the graphene layer. Then, the graphene grown on the other side is etched with an argon plasma. Using an $FeCl_3$ solution, also the copper foil is etched, and PMMA/graphene is left afloat on the solution with the PMMA facing upwards. The PMMA/graphene is transferred to DI water to remove residues of $FeCl_3$ and subsequently scooped with a substrate, and left to dry for a day. After baking on a hot plate at 130°C for 15 minutes to let the graphene stick and remove any water residues, the PMMA is removed with acetone, rinsed in IPA, and dried with a N_2 gas. Graphene covering half of SiO_2 is shown in Figure 3.2c.

3.2.4 CVD of WS_2

Atomically thin layer of WS_2 reaching 30 μm sizes can be grown by CVD. One method is to deposit a thin layer of WO_3 onto Si/SiO_2 substrate and then expose to a high concentration of sulphur gas. Alternatively, WO_3 powder is placed in a crucible or on a separate substrate facing the target Si/SiO_2. In order to sulfurize the WO_3, a sulphur powder is placed upstream in the furnace. Using argon or nitrogen as a carrier gas at high temperature ($\sim$ 800°C), thin layer of WS_2 flakes are grown, shown in Figure 3.2d [5, 6].

WS_2 forms as [7]

$$7S + 2WO_3 \longrightarrow 2WS_2 + 3SO_2. \tag{3.2}$$

A triangular shape comes from the non-uniform growth ratio of W and S along the substrate surface. This depends on the growing rate of the different domain edges. If the domain edges grow equally, the shape of the flake becomes hexagonal [8]. Otherwise, S or W terminations grow faster, and this results in triangular flake shapes [8].

3.2.5 Dry TMDC transfer

CVD grown WS_2 on SiO_2/Si can be transferred to a different target substrate by means of a dry transfer technique. First, 4-5 drops of 495K PMMA are dropped on the substrate where the density of WS_2 flakes is high, see Figure 3.3a and b. It is left to dry for a day, and PMMA becomes thick and flexible on the SiO_2 surface, shown as Figure 3.3c. Edges of the dry PMMA are lifted with the help of a scalpel under a long working distance microscope. Small droplets of water are applied on the edges which lift the PMMA and flakes from the surface (Figure 3.3d). The PMMA with flakes can be easily transferred to the desired surface, see Figure 3.3e . PMMA is slightly melted on the transferred sample by heating to $\sim$ 165°C, and it is removed with anisole and acetone solvents (Figure 3.3f). In this process, only PMMA is used as a stamp which can be removed easily with acetone.

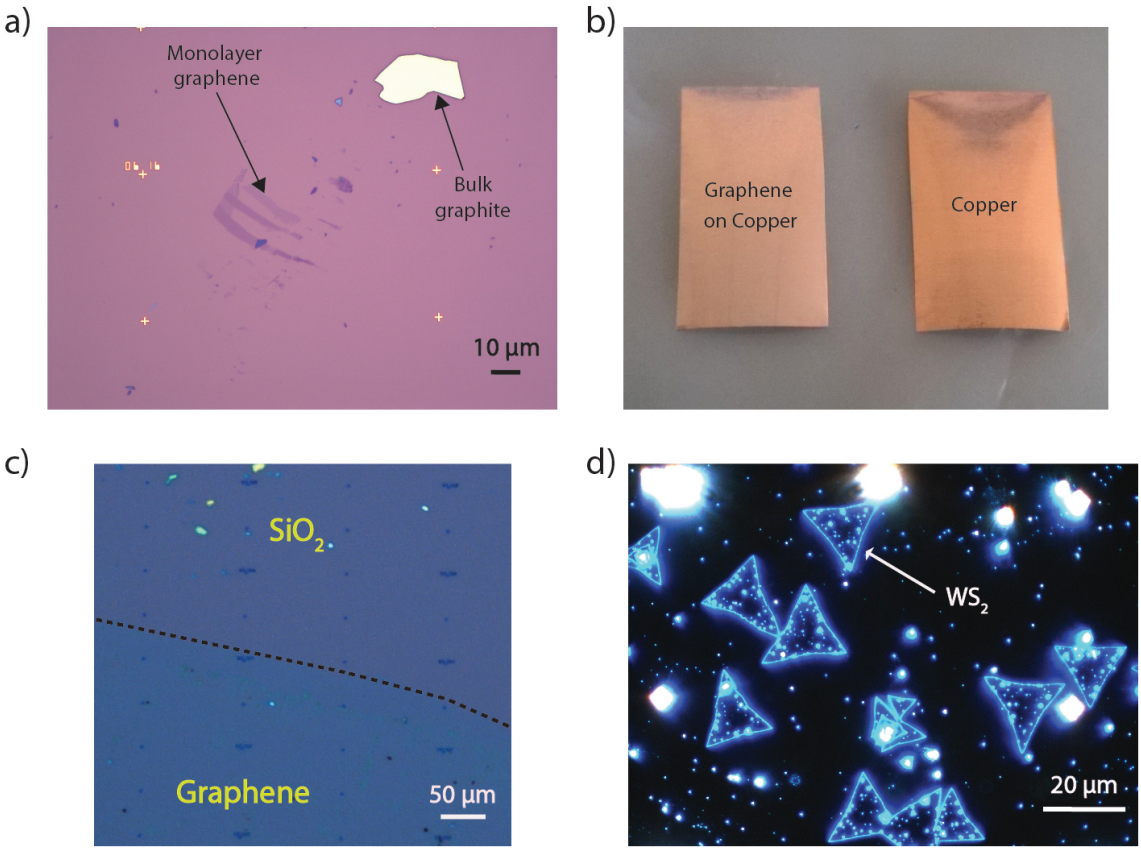

Figure 3.2: (a) Exfoliated graphene on SiO_2, (b) CVD graphene grown on copper (left) and copper foil before the growth (right), (c) CVD graphene on SiO_2 and (d) dark field microscopy image of CVD grown WS_2 (bright blue coloured triangles) on SiO_2.

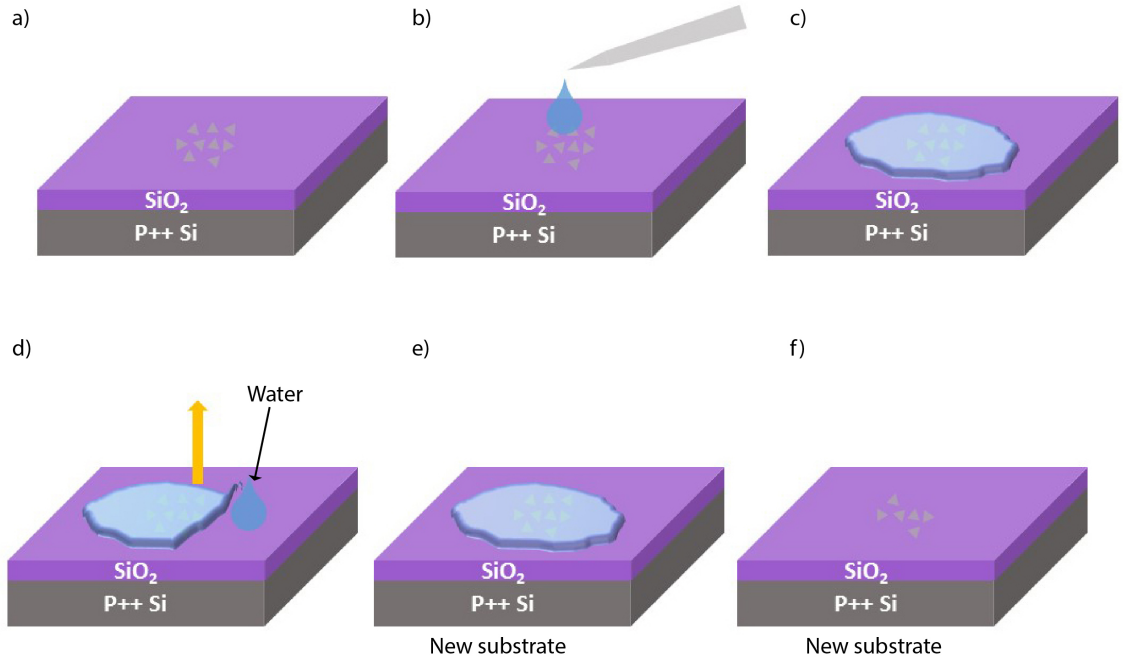

Figure 3.3: Dry transfer technique of CVD grown TMDC: (a) CVD grown TMDCs, (b) drop-cast of PMMA, (c) PMMA after it is left drying for a day, (d) removing of jelly-flexible PMMA, (e) PMMA put on a new substrate, and (f) removal of PMMA with solvents.

3.2.6 Laser beam writer

After obtaining two-dimensional materials on Si/SiO_2 substrate, they can be patterned with a lithography tool. Laser beam writer is an optical method to pattern desired shapes on substrates. Resolution of the lithography method can go down to 200 nm. A beam size ranging from 0.6 μm to 5 μm is used to write large area patterns.

In order to fabricate the contacts, first, $\sim$ 200 nm polymethylglumarimide (PMGI) is spin-coated as a sacrificial layer. This resist layer protects the sample from the photoresist which might contaminate the flakes. PMGI is baked at 160°C for 10 minutes to remove any solvents. Then, a thin layer photoresist S1813 (Rohm and Haas Electronic Materials) is spin-coated at 7000 rpm, this gives 900 nm thickness, see Figure 3.4a. It is baked again 10 minutes at 160°C. A 405 nm laser beam is rastered on the sample to directly write the patterns, shown as Figure 3.4b. The photoresist is developed for 35 seconds in MF319 (Microposit, 2-3% tetramethylam-

monium hydroxide in water), then dipped into deionized water (Figure 3.4c). Cr/Au contacts are evaporated and they are lifted-off in acetone, see Figure 3.4d and e. The bottom PMGI layer is removed with MF319, Figure 3.4f shows the cross-section schematic of the sample after the fabrication.

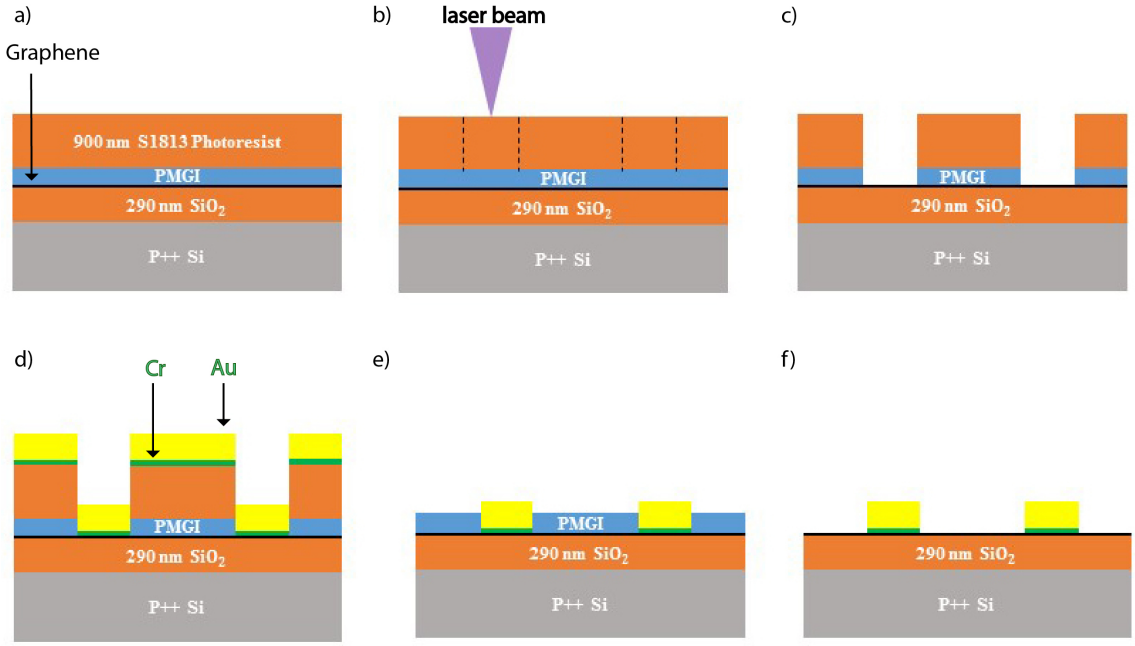

Figure 3.4: (a) Deposited PMGI and photoresist on the substrate with graphene flakes, (b) 405 nm laser beam exposure, (c) developing with MF319, (d) deposition of Cr/Au, (e) lift-off of photoresist with acetone, (f) cleaning of remaining PMGI with MF319.

3.2.7 Electron beam lithography (EBL)

A beam of focused electrons is used to change the chemical bonds in polymers covering semiconducting substrates. For the work presented in this thesis, I use PMMA to pattern metallic contacts. For this positive resist, the electron beam breaks the bonds of the resist and in the development the exposed PMMA areas are removed.

EBL is used to pattern electronic contacts on graphene and TMDCs. First, 375 nm of 950K PMMA is spin-coated onto the sample as the polymer resist before being baked for 1-10 minutes at 160°C to evaporate the anisole solvent, see Figure 3.5b. Electron beam at 80 kV and 5 nA beam current is scanned on pre-defined areas, shown as Figure 3.5d. Previously deposited alignment marks on the surface of SiO_2

with similar method help to precisely obtain the defined pattern on the surface. Patterns are developed with a mixture of IPA, methyl isobutyl ketone (MIBK) and methyl ethyl ketone (MEK), 15 ml, 5 ml, 1 ml respectively for 1 minute. Then, it is dipped into IPA to stop the developing process. Obtained patterns are inspected with an optical microscope (Figure 3.5e).

Metallic connections are deposited by thermal evaporation. 6 nm Cr and 65 nm Au are deposited at a pressure of $\sim 2 \times 10^{-6}$ Torr with low rate of deposition (0.2 Å/s of Cr, 0.5 Å/s of Au) in order to increase uniformity of metallic particles, achieve low contact resistance, and avoid any melting of PMMA due to the heat generated by thermal evaporator, see Figure 3.5f. In some applications, only a thin layer of Au is deposited on the flakes as a contact layer, and the pads are then defined as Cr/Au, as previously described. The excess Au is removed by dissolving the remaining PMMA in acetone at 55°C (lift-off). The sample is then rinsed in IPA and dried with N_2 gas, see Figure 3.5g. The sample can be left three days in acetone to remove any PMMA contamination. The fabricated device is placed on a chip carrier where the contacts pads are wire-bonded. Now the devices are ready for the electrical characterisation.

3.3 Layer number characterisation and Raman spectroscopy

3.3.1 Optical contrast measurements

Graphene is an optically transparent material with just 2.3% absorption of white light as defined by the fine structure constant (1/137), $\alpha = e^2/\hbar c$, where c is the speed of light [9]. As the number of layers, n, increases, the absorption increases by 0.023n. In few-layer graphene on Si/SiO_2, the number of layers can be determined through the attentive analysis of the optical contrast of the flakes [10–12].

The refractive index of Si/SiO_2 depends on the wavelength of incoming light [11], and the contrast of graphene can be found using the Fresnel law for different

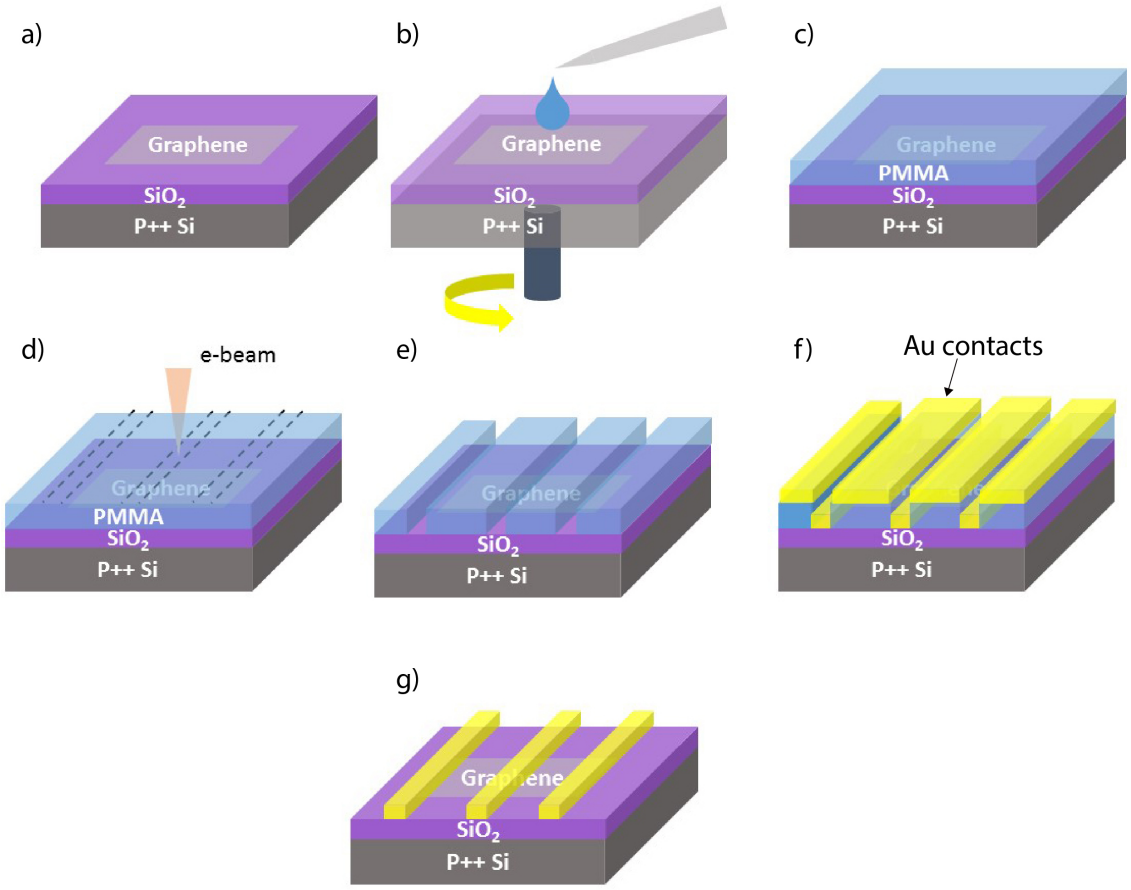

Figure 3.5: Electron beam lithography fabrication process: (a) A substrate with a graphene flake, (b) spin coating of PMMA, (c) PMMA on the substrate, (d) electron beam (e-beam) exposure, (e) developing with IPA, MIBK, MEK removes the exposed PMMA parts, (f) deposition of Cr/Au by thermal evaporator, (g) lift-off of the PMMA with acetone.

thickness of SiO_2 [10]. The highest contrast for graphene on 290 nm SiO_2 is achieved at the green wavelength of the visible spectrum [10]. Therefore, a green filter (568 nm) is commonly used to increase visibility and contrast of graphene flakes in the microscope images, see Figure 3.6a . The images are analysed with ImageJ software in order to compare green channel pixel values between the graphene and substrate. Points 1 and 2 or 1 and 3 on Figure 3.6b can be used to acquire pixel value references. Average green channel pixel value can be calculated as

$$C = \frac{\mid I(SiO_2/Si) - I(sample) \mid}{I(SiO_2/Si)} \tag{3.3}$$

where $I(sample)$ and $I(SiO_2/Si)$ are the pixel values on graphene and substrate respectively [10].

The contrast method analysis is reliable in distinguishing thin (< 4 layers) flakes, since the difference in the contrast for the larger number layers reduces quickly to lower values than the measurement noise level.

3.3.2 Raman spectroscopy of graphene and WS_2

Another method commonly used to characterise two-dimensional materials is Raman spectroscopy [14] which is optical, contactless and non-destructive. It is based on activating phonon modes in a crystal via the excitation of electrons by absorbed photons, which can cause two types of scattering. If momentum is conserved, the electron returns to the same energy state emitting a photon at the same wavelength, then elastic (Rayleigh) scattering occurs. However, in Raman scattering an electron returns to a different vibrational state emitting a photon of different wavelength from that of the incoming photon. Raman scattering can develop in two ways. If the emitted photon has a lower (higher) energy than the incoming photon the process is known as Stokes (Anti-Stokes). Resonant processes occur when the electron is excited to an another unoccupied electronic state, see Figure 3.7 [15].

Here, a sample is illuminated with a 532 nm (2.33 eV) laser using a commercial Renishaw system. The change in the frequency of the light is recorded by a charge

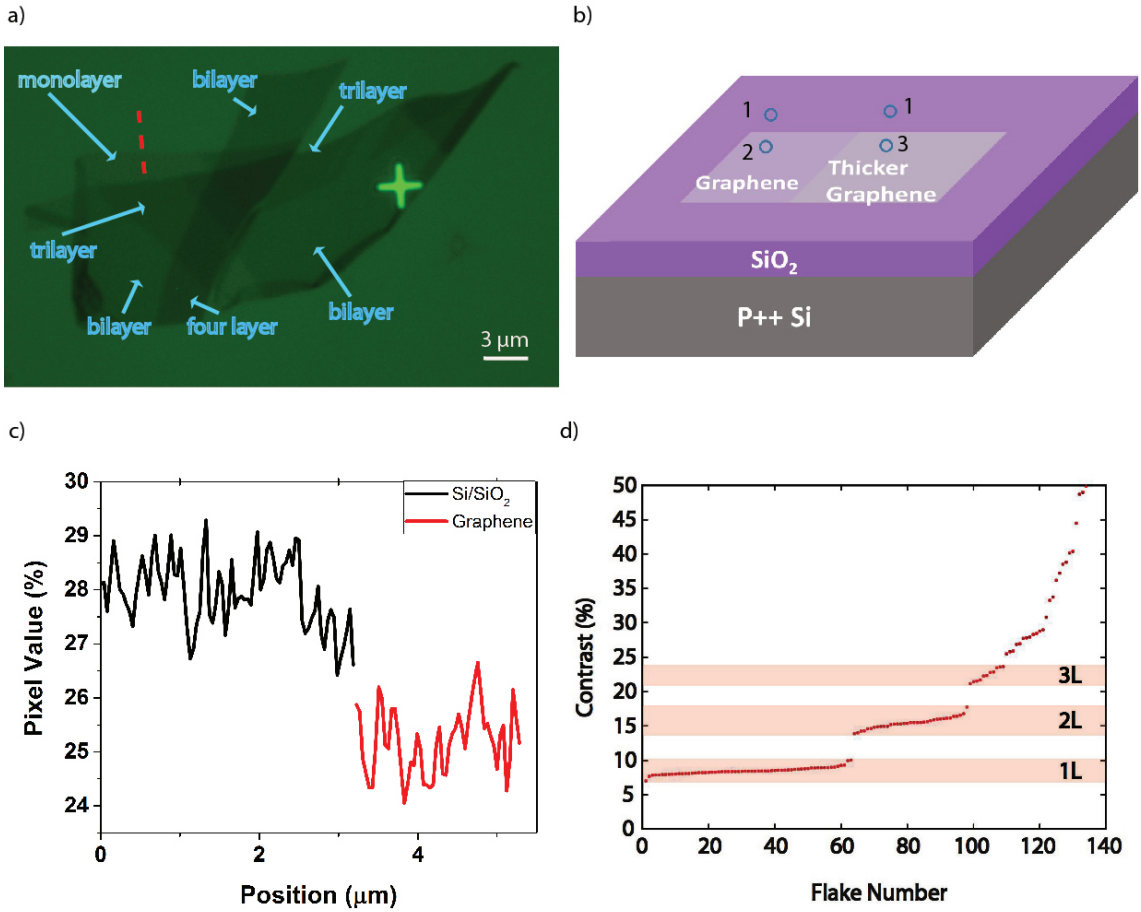

Figure 3.6: (a) Different layers of graphene after exfoliation, red dashed line corresponds to ImageJ line in (c) where the end points are compared in order to calculate contrast difference, (b) positions where the pixel measurement is taken from, 1 is on the surface of SiO_2, 2 is on monolayer graphene, 3 represents the position on trilayer graphene, (c) pixel difference measurement on the red dashed line in (a), (d) contrast measurements for different thickness of graphene, adapted from [13].

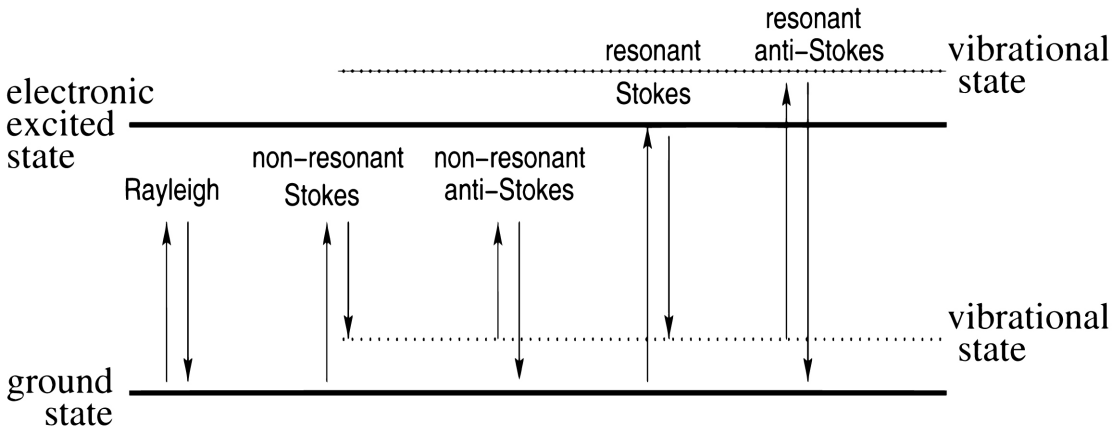

Figure 3.7: Rayleigh resonant and non-resonant stokes-anti-stokes Raman scattering, adapted from [15].

coupled device (CCD) detector. Raman spectroscopy can be used widely in chemical compounds as well as thin films and atomically thin materials identifying unknown materials and physical properties, quality and crystal structure of a material.

Raman spectroscopy of graphene

The Raman processes of graphene can be explained using the phonon dispersion relation and the electron-phonon interactions, see Figure 3.8 [16]. It has six phonon modes and three of which are acoustic (A), and three are optical (O). They both have in-plane transverse (T), longitudinal (L) and out-of-plane (Z) flexural or bending oscillations. TO and LO phonon modes are the dominant mechanisms in Raman scattering of graphene.

The in-plane vibration of sp2 bonded carbon atoms leads to the G peak. This is due to a first order single resonance process at Γ point where TO and LO are degenerate. An electron is excited to the conduction band and it is scattered by a phonon near the Γ point, see Figure 3.8b. Finally, the electron recombines with a hole emitting a photon.

Defect or disorder activated modes such as the D peak originate from vibrations of the LO phonon mode. Defects on CVD grown graphene can trigger these transitions. The D band is activated with the double resonance process involving single electron-phonon scattering near the K point of Brillouin zone due to the defects. An electron is excited and then scattered by a phonon to another valley and subsequently scattered back due to a defect emitting a photon when returning to the valence band states [17]. The D+D" peak is a combination of D and LA phonon mode oscillations due to the defects.

The 2D peak arises from second order double resonance involving two-phonon scattering on LO phonon mode near the K point. An excited electron scatters off a phonon into another valley, see Figure 3.8b. It returns back and recombines as emitting photon. This is an inter-valley process involving two phonons. If holes are scattered instead of electrons, the recombination of electron-hole pair at K' point can generate a resonant condition which results in a triple resonance.

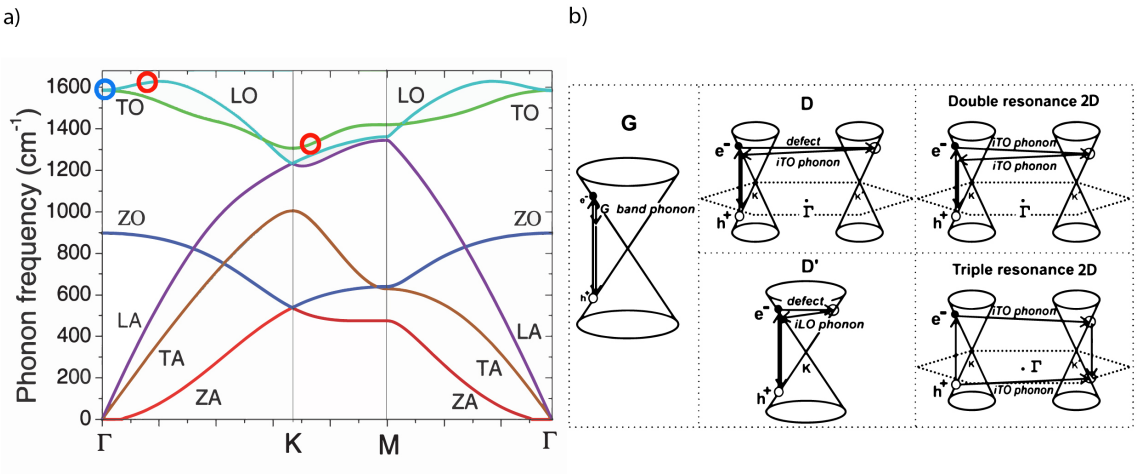

Figure 3.8: (a) Phonon dispersion modes of monolayer graphene, adapted from [16], G band is at blue circle on the left, and circle on the right is related to D and 2D bands, (b) Raman scattering processes in graphene, adapted from [17].

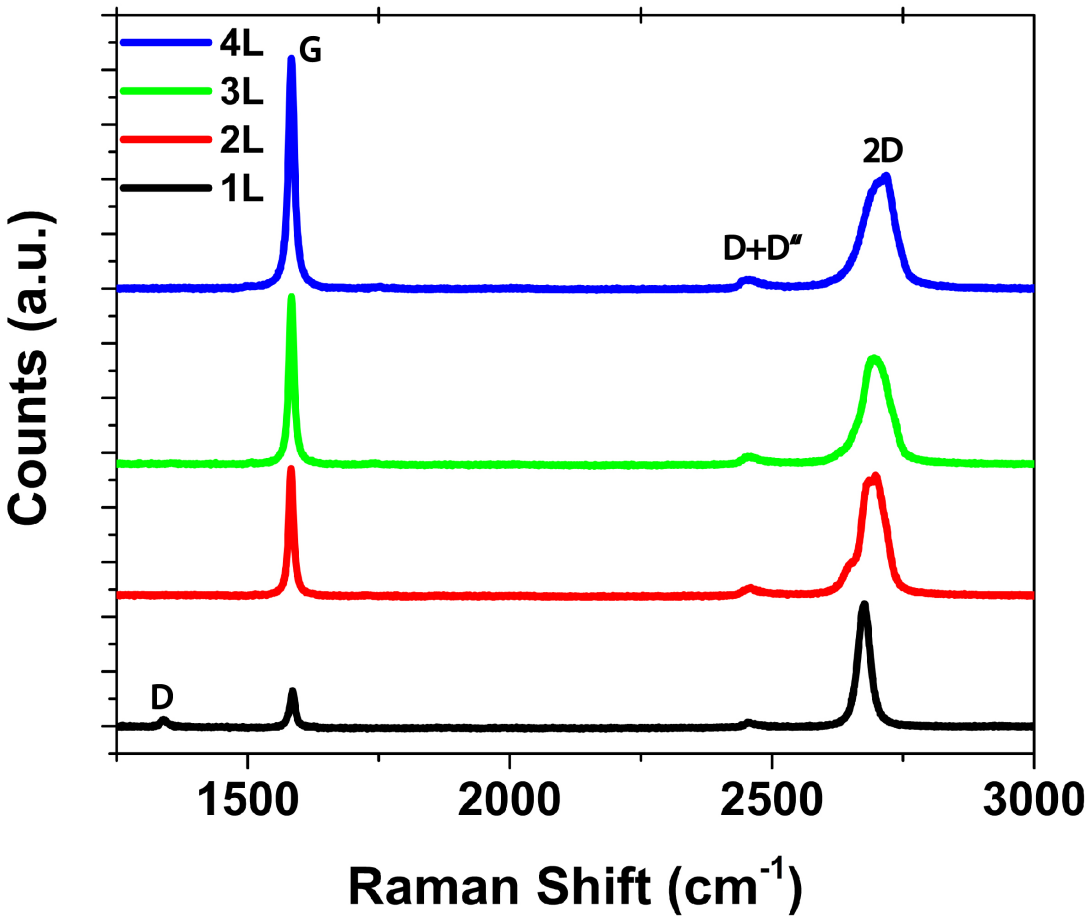

Figure 3.9: Raman spectra of few and monolayer graphene measured at 532 nm which shows D, G, 2D and D+D" peaks.

One of the easiest ways to characterise graphene and its thickness is Raman spectroscopy. Since few and monolayer graphene can be distinguished according to the relative intensity of the G and 2D peaks as well as the shape of the 2D peak. In pristine graphene, the G peak is located at 1586 cm^{-1} and 2D is at 2700 cm^{-1} [18]. Defect related D peak and D+D" peaks are at 1350 cm^{-1} and 2460 cm^{-1}, see Figure 3.9.

2D peak of monolayer graphene can be identified by its single Lorentzian peak shape, see Figure 3.10. Few and multilayer graphene have more transitions than monolayer graphene resulting in multiple Lorentzian peaks at 2D, see Figure 3.10. For example, four possible transitions exist in bilayer graphene. Two pairs of the four bands are strongly coupled with the light, and two nearly degenerate transverse optical phonons couple with conduction bands resulting in four different phonon processes with four different momenta (q_{1A}, q_{1B}, q_{2A}, q_{2B}), see Figure 3.11 [15].

Furthermore, the intensity of the G peak in monolayer graphene is half of the height of the 2D. Few and multilayer graphene have higher intensities of G peaks. The height ratio between 2D and G is about one in bilayer graphene, and G becomes larger for tri- and four-layer graphene. The intensity of G peak increases with the number of layers due to the rise in electrons involved in G-band transitions.

Another way to identify the thickness is to analyse the full width at half maximum (FWHM) of 2D peak. This is 26.3 cm^{-1} for monolayer graphene and 52.1 cm^{-1} for bilayer [19]. Moreover, trilayer and four-layer shows 56.1 cm^{-1} and 62.4 cm^{-1} FWHM [19], see Figure 3.10. Up to few-layer graphene, this method can be used to determine number of layers.

Raman spectroscopy of WS_2

Not only graphene can be characterised, but also TMDCs such as WS_2 and their thickness can be identified by Raman spectroscopy [20, 21]. In order to avoid possible damage on the flakes, an optical density filter is used along the pathway of the laser to reduce the power of the laser ($\sim 40\ \mu W/\mu m^2$). The excitation wavelength of 532 nm laser corresponds to the energy of the B exciton from the spin-orbit splitting of

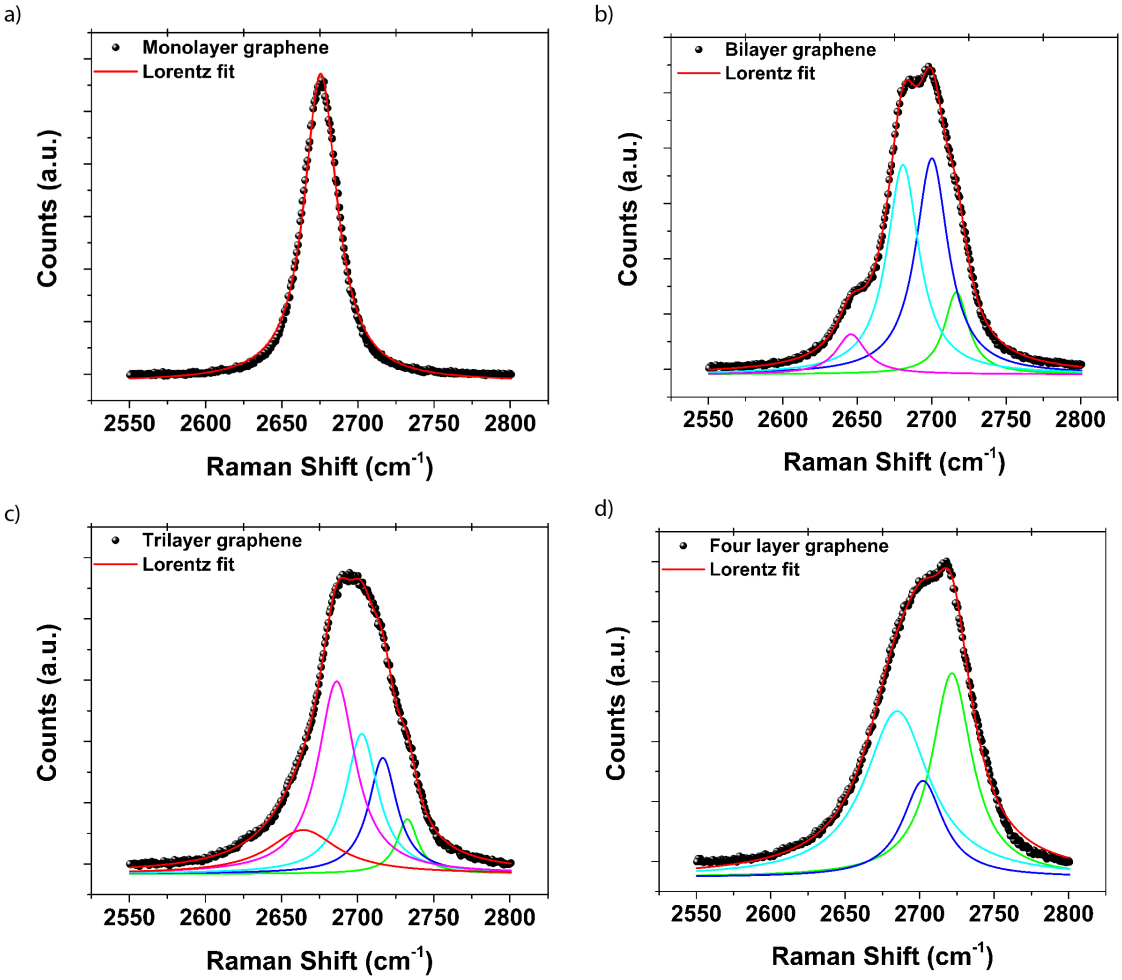

Figure 3.10: Raman spectra and Lorentz fit of 2D peak for (a) monolayer, (b) bilayer, (c) trilayer, (d) four-layer graphene.

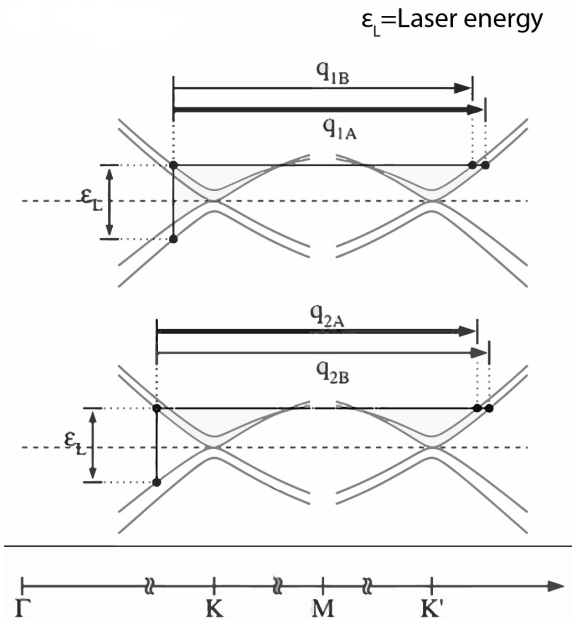

Figure 3.11: 2D peak, double resonance process in bilayer graphene adapted from [18].

WS_2 which can activate many phonon resonant modes. The main Raman modes that can provide information about the layer number are A_{1g} and 2LA(M) [21]. $E^1_{2g}(\Gamma)$ and $E^1_{2g}(M)$ peaks overlap with 2LA(M), as illustrated in Figure 3.12. They can be fitted with a Lorentzian function and the overlapped peaks can be distinguished.

In monolayer WS_2, $E^1_{2g}(\Gamma)$ and $E^1_{2g}(M)$ peaks at 358.6 cm^{-1} and 344.4 cm^{-1} represent in plane oscillations of the S and W atoms in opposite directions, while A_{1g} peak at 414 cm^{-1} is due to out of plane oscillations of sulphur atoms, see Figure 3.13c. The 2LA(M) peak is at 352 cm^{-1} and this corresponds to second order Raman resonance due to in plane oscillations of the atoms, see Figure 3.13c.

Figure 3.13a shows Raman spectra for WS_2 flakes of different number of layers. The intensity of $A_{1g}(\Gamma)$ increases with increasing layer number due to the stronger interlayer contributions for thicker layers [20]. The $A_{1g}(\Gamma)$ blue shifts with increasing thickness due to an increase in restoring force in van der Waals interactions between layers, whereas small redshift can be observed on the E_{2g} and 2LA phonon modes due to the dielectric screening effect of the vibration [20]. The Figure 3.13b shows the Raman shift difference between $A_{1g}(\Gamma)$ and 2LA(M) with respect to the number of layers which can assist to identify the number of layers for few-layer WS_2.

$A_{1g}(\Gamma)$ and 2LA(M) modes are polarisation dependent. The intensity of both peaks reduce when the polarisation of incoming and detected light are perpendicular to the plane of the flake, whereas the intensity of the peaks increases when the polarisation is parallel [22]. The position and intensity of the 2LA(M) peak also depend on the temperature. With decreasing the temperature, the 2LA peak blue shifts and its intensity becomes weaker than $E^1_{2g}(\Gamma)$ due to contraction of the lattice with temperature change. A shift in the phonon energies, which is introduced by a change in inter-atomic forces with temperature, causes anharmonic vibrations in the lattice led by phonon-phonon interactions [22, 23].

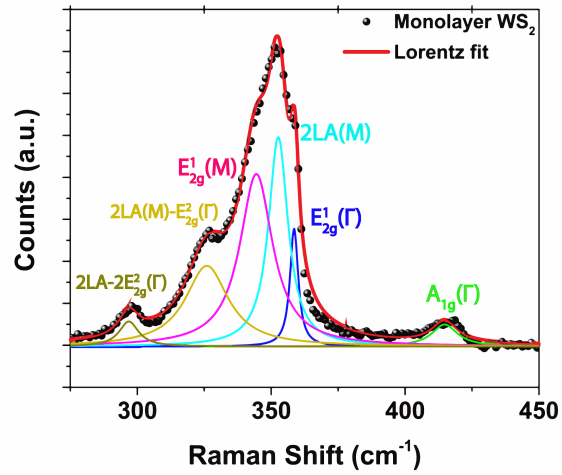

Figure 3.12: Raman spectra of monolayer WS_2.

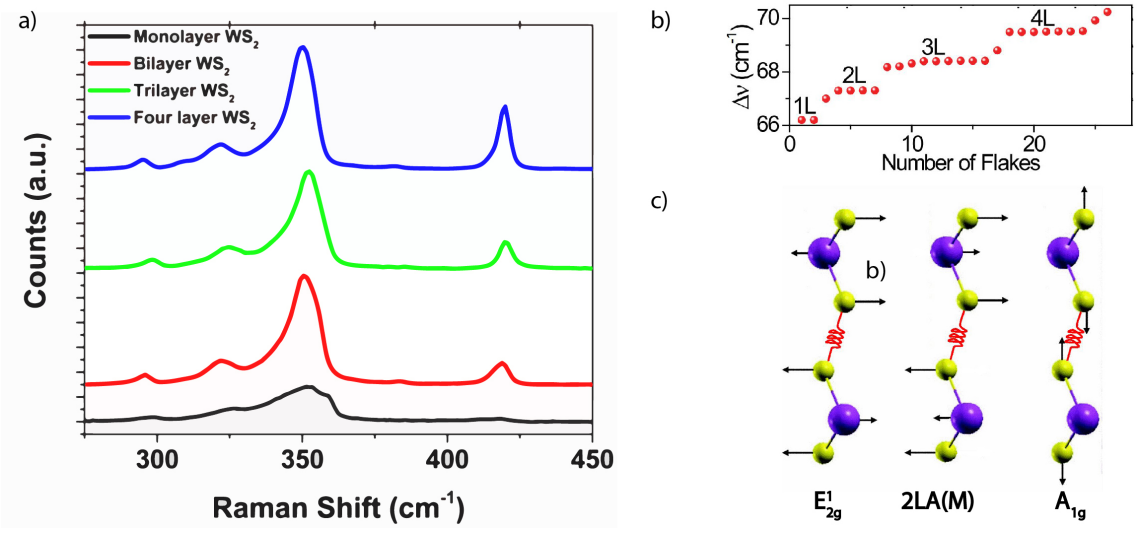

Figure 3.13: (a) Raman spectra of different numbers of WS_2, (b) $\Delta\nu$ corresponds to Raman shift difference between 2LA and A_{1g} mode, adapted from [21], (c) displacements E^1_{2g}, 2LA(M) and A_{1g} phonon modes where purple and yellow balls represent W and S atoms respectively, adapted from [24].

3.4 Electrical and optoelectronic measurements

3.4.1 Electrical transport in graphene

A variety of properties of graphene such as mobility, doping, conductivity and sheet resistance are commonly used as indicators of the quality of the material. These are commonly characterised with electrical transport measurements in a transistor geometry where the Fermi level can be modified by a perpendicular electrical field generated by a gate bias applied to the Si/SiO_2. Upon sweeping the bias applied to the back gate, graphene is electrostatically n (p) doped for negative (positive) bias, see Figure 3.14c. The gate sweep can be performed in two different ways which are zero-bias and constant source-drain voltage bias measurements.

For the zero-bias measurement, a lock-in amplifier (Ametek DSP 7270) is used to apply an AC signal between source and drain with a frequency and time constant which define average measurements of real and imaginary parts of the lock-in measurements, see Figure 3.14a. A 10 MΩ resistor which has at least two order of magnitude higher resistance than graphene is used as a ballast resistor to source constant current to the graphene. For the gate bias, the gate leakage is monitored simultaneously during the sweep using a Keithley 2400 sourcemeter. The resistance of graphene can be obtained directly from the lock-in using Kirchhoff's rules. The circuit can be defined as

$$V_{osc} - IR_{ballast} - IR_{sample} = 0 \tag{3.4}$$

where I is the current in the circuit, $R_{ballast}$ is the 10 MΩ resistor, and R_{sample} is the resistance of the graphene channel. In the limit that $R_{ballast}$ is much larger than R_{sample}, the resistance of the sample is given by

$$R_{sample} = \frac{V_{sd}R_{ballast}}{V_{osc}}. \tag{3.5}$$

The current in the circuit can be measured with a directly applied voltage, see

Figure 3.14b. A voltage source (Xitron 2000) is used to provide constant bias to the device and the current is measured with a multimeter (Agilent 34401A Multimeter). For small values of the currents, a current amplifier can be used in the circuit.

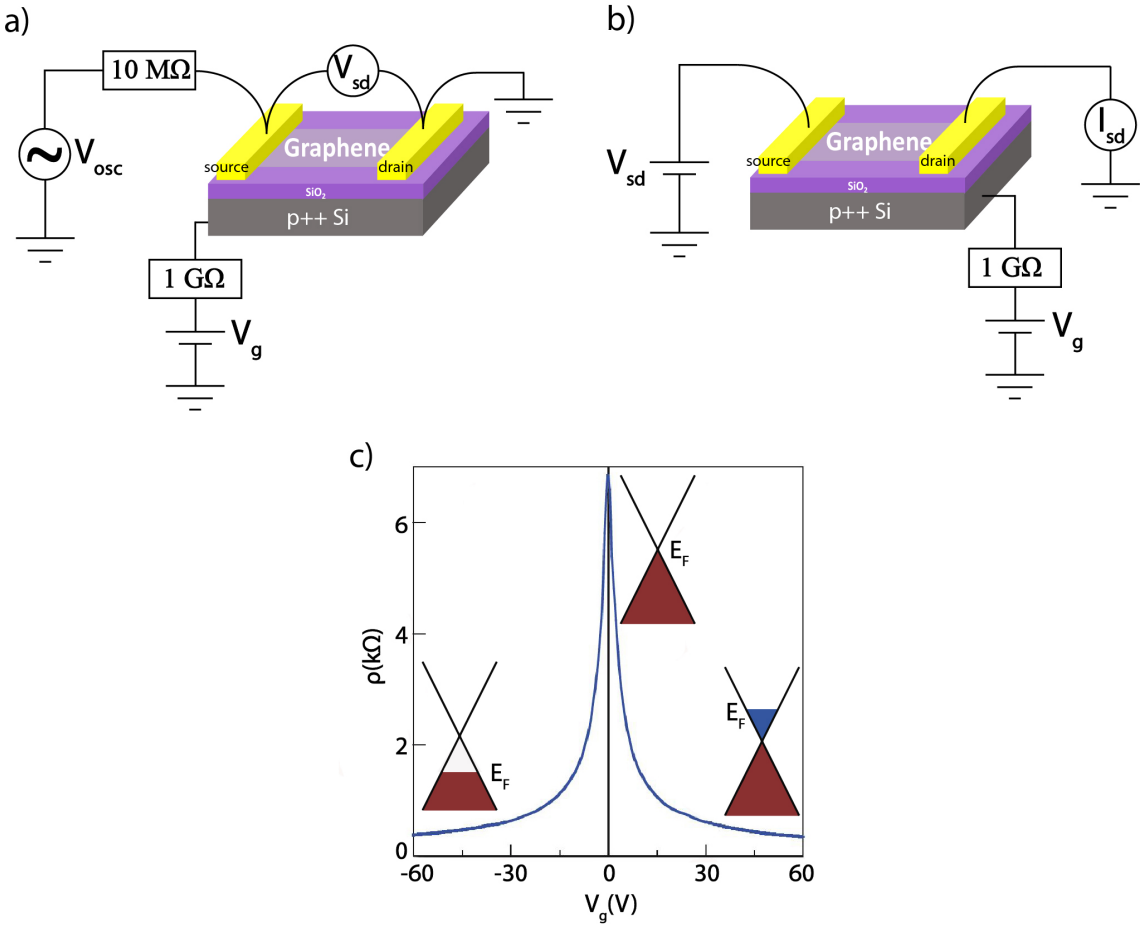

Figure 3.14: (a) Zero-bias or constant current electrical measurement set up, (b) constant voltage electrical measurement set up, (c) resistance versus gate bias for single layer graphene, adapted from [25]. The insets represent the Fermi level of the graphene.

High carrier mobility is a crucial property for assessing the quality of electronic devices. Within the Drude model, the mobility (μ) is a function of the electrical conductivity σ and the charge density (n):

$$\mu = \frac{\sigma}{ne} \tag{3.6}$$

where e is the electron charge. The carrier concentration can be found using the

parallel plate capacitor model as

$$n = \frac{C_g V_g}{e} \qquad \text{and} \qquad C_g = \frac{\epsilon_0 \epsilon_{SiO_2}}{d_{SiO_2}} \tag{3.7}$$

where C_g is the known geometrical capacitance of the device, V_g is the applied gate voltage, ϵ_0 is permittivity of free space, ϵ_{SiO_2} is permittivity of SiO_2, and d_{SiO_2} is the thickness of the gate. The conductivity (σ) depends on mobility linearly. It can be expressed as

$$\sigma = \frac{L}{w R_{sample}} \tag{3.8}$$

where L and w are the length and width of the channel respectively.

For the zero-bias measurements where resistance versus gate bias plots are obtained, the mobility is

$$\mu = \frac{L d_{SiO_2}}{\epsilon_0 \epsilon_{SiO_2} w} \frac{1}{R_{sample} V_g}. \tag{3.9}$$

Similarly, for the constant source-drain bias (V_{sd}) measurements, resistance of the channel is $R_{sample} = V_{sd}/dI_{sd}$, and the mobility can be expressed as a derivative of I_{sd} respect to V_{sd} with a constant which is

$$\mu = \frac{L d_{SiO_2}}{\epsilon_0 \epsilon_{SiO_2} w V_{sd}} \frac{dI_{sd}}{dV_g}. \tag{3.10}$$

The maximum resistance is reached at zero gate bias ($V_g = 0$), where the Dirac point is defined. Unwanted contamination in the processing dopes graphene and the Dirac point usually shifts toward the p-doped region. Upon annealing, these contaminants are removed and the Dirac peak shifts back to zero gate voltage.

3.5 Optoelectronic measurements

In order to study the optoelectronic properties of two-dimensional materials, I investigate their electrical properties under different illumination conditions. Change in the resistance of a device under a light exposure can give information about these features. Two different techniques are used to determine these properties

which are scanning photocurrent microscopy and a bulk illumination method with a monochromator.

3.5.1 Scanning photocurrent microscopy (SPCM)

In this thesis, I use a home developed scanning photocurrent microscopy system to characterise the photo-generated charge carriers upon laser illumination. The system consists of a computer controlled Cairn multiline-laserbank with four different laser beams: 473 nm, 514 nm, 561 nm and 685 nm. The selected laser light is directed to the sample using an upright Olympus BX51 microscope, see Figure 3.15a. The power of the illumination can be adjusted with the laser controller and optical density filters. Different magnification of the microscope objectives provides various sizes of beam spots down to 1 μm. The laser light can be a continuous wave or modulated through the transistor-transistor logic (TTL) of the laser bank controller. Standard lock-in technique is used for low-noise opto-electronic measurements. The electrical circuit on a device is shown on Figure 3.15b. The current signal is mapped as a function of the lateral position of the device using a motorised computer controlled XYZ stage with a resolution of 1 μm.

3.5.2 Bulk illumination

Another way to examine photodetection performance of a device is bulk illumination with monochromatic light. The bulk illumination setup contains a light source (Xenon arc or quartz tungsten halogen light source and power supply), collimating and focusing lenses, monochromator, and a vacuum tube with a fused quartz window, see Figure 3.16a. The light source systems are provided by Oriel tunable light source systems (TLS) and the vacuum chamber is integrated to this system. The setup is covered by a blackout light curtain to protect the light-sensitive equipment and measurements. The energy of the white light is tuned with the monochromator. Similar to SPCM measurements, the photocurrent is measured under dark and illumination with a current amplifier and a multimeter, illustrated as Figure 3.16b. The

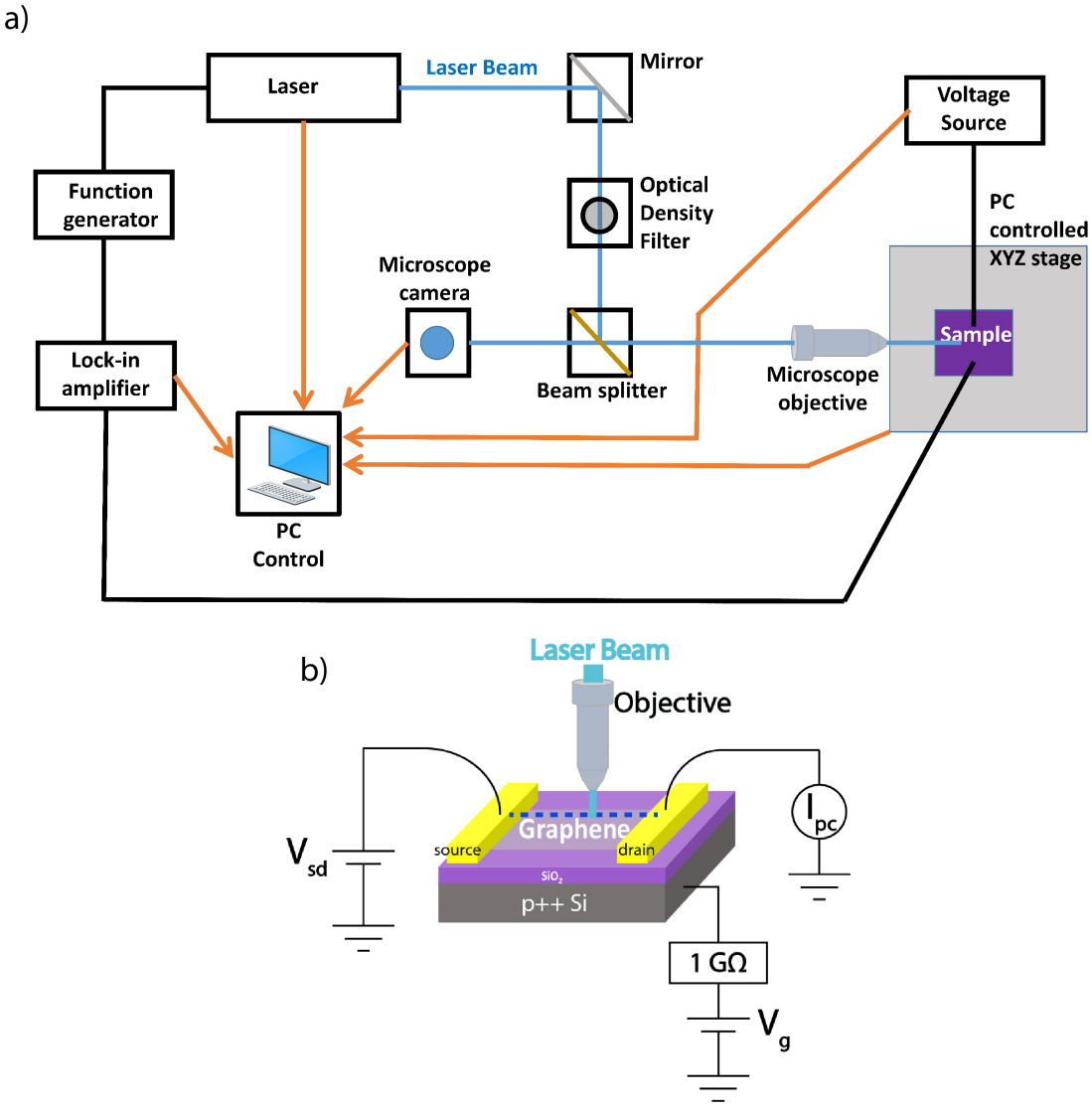

Figure 3.15: (a) Schematic of the scanning photocurrent microscopy experimental setup, the laser beam is provided by the laserbank. Beam splitter, microscope camera and microscope objective are mounted on the microscope, Olympus BX51. (b) Electrical connections of the sample measured on this setup, blue dashed line represents the horizontal laser scan, movement of the stage allows the laser rastered on the graphene.

power of the light can be adjusted with optical density filters and can be calibrated with a powermeter and a photodiode. Power densities down to 10^{-9} W/cm^2 can be achieved. This can provide highly sensitive measurements for photodetectors and memory devices.

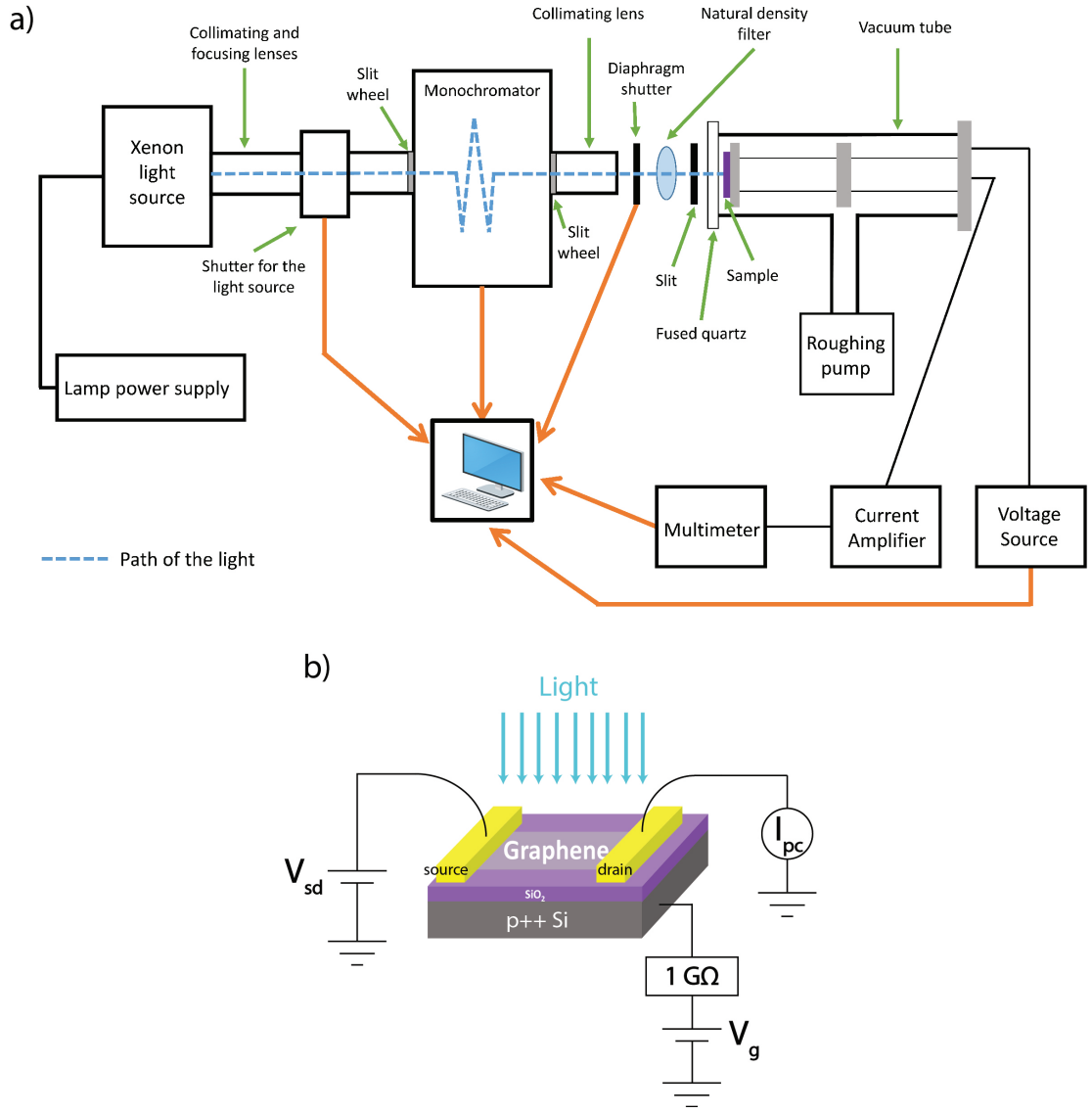

Figure 3.16: (a) The bulk illumination setup, Oriel tunable light source system with a sample stage embedded in a vacuum tube, (b) electrical schematic of a device for the white light measurements.

Bibliography

[1] H. Kim, E. Saiz, M. Chhowalla, and C. Mattevi, "Modeling of the self-limited growth in catalytic chemical vapor deposition of graphene," *New Journal of Physics*, vol. 15, p. 053012, Feb 2013.

[2] T. H. Bointon, M. D. Barnes, S. Russo, and M. F. Craciun, "High quality monolayer graphene synthesized by resistive heating cold wall chemical vapor deposition," *Advanced Materials*, vol. 27, no. 28, pp. 4200–4206, 2015.

[3] X. Li, W. Cai, J. An, S. Kim, J. Nah, D. Yang, R. Piner, A. Velamakanni, I. Jung, E. Tutuc, S. K. Banerjee, L. Colombo, and R. S. Ruoff, "Large-area synthesis of high-quality and uniform graphene films on copper foils," *Science*, vol. 324, no. 5932, pp. 1312–1314, 2009.

[4] J. W. Suk, A. Kitt, C. W. Magnuson, Y. Hao, S. Ahmed, J. An, A. K. Swan, B. B. Goldberg, and R. S. Ruoff, "Transfer of CVD-grown monolayer graphene onto arbitrary substrates," *ACS Nano*, vol. 5, no. 9, pp. 6916–6924, 2011.

[5] C. Cong, J. Shang, X. Wu, B. Cao, N. Peimyoo, C. Qiu, L. Sun, and T. Yu, "Synthesis and optical properties of large-area single-crystalline 2D semiconductor WS_2 monolayer from chemical vapor deposition," *Advanced Optical Materials*, vol. 2, pp. 131–136, Feb 2014.

[6] H. R. Gutiérrez, N. Perea-López, A. L. Elías, A. Berkdemir, B. Wang, R. Lv, F. López-Urías, V. H. Crespi, H. Terrones, and M. Terrones, "Extraordinary room-temperature photoluminescence in triangular WS_2 monolayers," *Nano Letters*, vol. 13, pp. 3447–3454, Aug 2013.

[7] Y. Zhang, Y. Zhang, Q. Ji, J. Ju, H. Yuan, J. Shi, T. Gao, D. Ma, M. Liu, Y. Chen, X. Song, H. Y. Hwang, Y. Cui, and Z. Liu, "Controlled growth of high-quality monolayer WS_2 layers on sapphire," *ACS Nano*, vol. 7, no. 10, pp. 8963–8971, 2013.

[8] S. Wang, Y. Rong, Y. Fan, M. Pacios, H. Bhaskaran, K. He, and J. H. Warner, "Shape evolution of monolayer MoS_2 crystals grown by chemical vapor deposition," *Chemistry of Materials*, vol. 26, pp. 6371–6379, 2014.

[9] R. R. Nair, P. Blake, A. N. Grigorenko, K. S. Novoselov, T. J. Booth, T. Stauber, N. M. R. Peres, and A. K. Geim, "Fine structure constant defines visual transparency of graphene," *Science*, vol. 320, pp. 1308–1308, Jun 2008.

[10] P. Blake, E. W. Hill, A. H. Castro Neto, K. S. Novoselov, D. Jiang, R. Yang, T. J. Booth, and A. K. Geim, "Making graphene visible," *Applied Physics Letters*, vol. 91, no. 6, pp. 2007–2009, 2007.

[11] Z. H. Ni, H. M. Wang, J. Kasim, H. M. Fan, T. Yu, Y. H. Wu, Y. P. Feng, and Z. X. Shen, "Graphene thickness determination using reflection and contrast spectroscopy," *Nano Letters*, vol. 7, no. 9, pp. 2758–2763, 2007.

[12] M. F. Craciun, S. Russo, M. Yamamoto, J. B. Oostinga, A. F. Morpurgo, and S. Tarucha, "Trilayer graphene is a semimetal with a gate-tunable band overlap," *Nature Nanotechnology*, vol. 4, no. 6, pp. 383–388, 2009.

[13] D. C. Hudson, *Two dimensional atomically thin materials and hybrid superconducting devices*. PhD thesis, University of Exeter, 2014.

[14] C. V. Raman and K. S. Krishnan, "A new type of secondary radiation," *Nature*, vol. 121, pp. 501–502, Mar 1928.

[15] A. C. Ferrari and D. M. Basko, "Raman spectroscopy as a versatile tool for studying the properties of graphene," *Nature Nanotechnology*, vol. 8, pp. 235–46, Apr 2013.

[16] J. A. Yan, W. Y. Ruan, and M. Y. Chou, "Phonon dispersions and vibrational properties of monolayer, bilayer, and trilayer graphene: Density-functional perturbation theory," *Physical Review B - Condensed Matter and Materials Physics*, vol. 77, no. 12, pp. 1–7, 2008.

[17] L. Malard, M. Pimenta, G. Dresselhaus, and M. Dresselhaus, "Raman spectroscopy in graphene," *Physics Reports*, vol. 473, pp. 51–87, Apr 2009.

[18] A. C. Ferrari, J. C. Meyer, V. Scardaci, C. Casiraghi, M. Lazzeri, F. Mauri, S. Piscanec, D. Jiang, K. S. Novoselov, S. Roth, and A. K. Geim, "Raman spectrum of graphene and graphene layers," *Physical Review Letters*, vol. 97, no. 18, 2006.

[19] Y. Hao, Y. Wang, L. Wang, Z. Ni, Z. Wang, R. Wang, C. K. Koo, Z. Shen, and J. T. L. Thong, "Probing layer number and stacking order of few-layer graphene by Raman spectroscopy," *Small*, vol. 6, no. 2, pp. 195–200, 2010.

[20] A. Berkdemir, H. R. Gutiérrez, A. R. Botello-Méndez, N. Perea-López, A. L. Elías, C.-I. Chia, B. Wang, V. H. Crespi, F. López-Urías, J.-C. Charlier, H. Terrones, and M. Terrones, "Identification of individual and few layers of WS_2 using Raman spectroscopy," *Scientific Reports*, vol. 3, p. 1755, Apr 2013.

[21] F. Withers, T. H. Bointon, D. C. Hudson, M. F. Craciun, and S. Russo, "Electron transport of WS_2 transistors in a hexagonal boron nitride dielectric environment," *Scientific Reports*, vol. 4, p. 4967, May 2014.

[22] A. A. Mitioglu, P. Plochocka, G. Deligeorgis, S. Anghel, L. Kulyuk, and D. K. Maude, "Second-order resonant Raman scattering in single-layer tungsten disulfide WS_2," *Physical Review B - Condensed Matter and Materials Physics*, vol. 89, no. 24, pp. 1–5, 2014.

[23] R. Yan, J. R. Simpson, S. Bertolazzi, J. Brivio, M. Watson, X. Wu, A. Kis, T. Luo, A. R. Hight Walker, and H. G. Xing, "Thermal conductivity of mono-

layer molybdenum disulfide obtained from temperature-dependent Raman spectroscopy," *ACS Nano*, vol. 8, no. 1, pp. 986–993, 2014.

[24] A. Molina-Sánchez and L. Wirtz, "Phonons in single-layer and few-layer MoS_2 and WS_2," *Physical Review B - Condensed Matter and Materials Physics*, vol. 84, no. 15, 2011.

[25] A. K. Geim and K. S. Novoselov, "The rise of graphene," *Nature Materials*, vol. 6, pp. 183–191, Mar 2007.

Chapter 4

Contact resistance based on few-layer CVD grown WS_2

4.1 Introduction

Over the course of the last decade, significant research efforts have been made to determine the physical properties of atomically thin TMDCs. In doing so, a number of technical problems have been encountered, one of which is an ongoing issue of the high contact resistance between the metal electrode and TMDC. Charge carriers flowing in a field-effect transistor (FET) encounter a large potential barrier at the metal-semiconductor interface, which restricts the flow of current in the transistor. Reducing the contact resistance is crucial for improving device performance such as achieving a higher saturation current in the ON state of the TMDC FET.

Metal-TMDC contacts have higher contact resistance than graphene and other semiconductors such as InGaAs and GaN [1]. One of the reasons for this resistance is the presence of a Schottky barrier at the metal/TMDC interface. The difference between the work function of the metal and electron affinity of the n-type semiconductor can form this barrier. In commercial semiconductors, the contact resistance can be reduced by ion-implantation where the contact areas below source-drain are bombarded by high energy ions and doped. However, it is hard to control doping density, dose and ion exposure in atomically thin structure of two-dimensional ma-

terials [2, 3]. The Schottky barrier in TMDCs can be lowered using different metals with work functions close to the electron affinity of the TMDCs, changing the phase of the TMDCs below the contacts from 2H to 1T and fabricating edge contacts can reduce the contact resistance [4–6].

The minimum contact resistance is defined by the quantum limit depending on the number of electron modes of the contact semiconductor [1, 7]. The minimum conductivity can be written as

$$R^{-1} = \sigma = \frac{2q^2}{h} M \approx \frac{M}{12.9\ k\Omega} \qquad \text{and} \qquad M = k_f W/\pi \tag{4.1}$$

where M is the number of propagating electron modes which depends on Fermi wavenumber (k_f) and width of the contact (W) [7]. Here, h is the Plank constant and q is the electron charge. The quantum limit of the TMDCs is 30 Ω μm [1, 8]. However, the lowest contact resistance reported for few-layer WS_2 is 0.7 kΩ μm where the contacts are doped by chloride molecular doping technique [4]. Sulphur vacancies in the WS_2 can be replaced by chloride (Cl) atoms, extra electrons donated by Cl atoms reduce the contact resistance [4]. With phase change of MoS_2 from 2H to 1T, resistances down to 200 Ω μm have been achieved [5].

In this chapter, the contact resistance of CVD-grown few-layer WS_2 of varying channel lengths is investigated at room temperature and in a liquid helium environment. I find a high contact resistance of the order of MΩ μm, independent of width and length of the channel. Possible oxide impurities, contamination and defects due to the fabrication methods, Schottky barrier and Fermi level pinning and van der Waals gap between the bulk metal and atomically thin WS_2 affect the value of contact resistance [8, 9].

4.2 Experimental details

Atomically thin WS_2 flakes are grown on a 300 nm Si/SiO_2 substrates by chemical vapour deposition, see Chapter 3. Optical microscopy allows the identification of the CVD WS_2 triangles, with flake edges easily distinguished using dark field illumination. Oxide spots or secondary domains under the flakes can readily be observed in this mode, see Figure 4.1a and b. These are usually caused by the growth method. Furthermore, the flakes are triangular due to the growth rate of the flakes [10]. The lighter spots on Figure 4.1b are the WO_3 seeds from which WS_2 domains are grown by sulphurisation of the WO_3. The lateral size of CVD grown WS_2 flakes ranges from 5 to 30 μm. Optical inspection allows the selection of large area flakes, which are free from contaminants left behind the growth process.

Raman spectroscopy is used to characterise the quality and thickness of the flakes. It is acquired under ambient conditions with a Renishaw spectrometer containing an excitation laser of 532 nm. Figure 4.1c shows the Raman spectra of a CVD grown WS_2 flake. The layer dependent Raman modes, A_{1g}, E_{2g} and 2LA, are observed. The spectra can be compared with previous literature to identify the number of layers [11–13]. The difference of the A_{1g} and 2LA modes is 68 cm^{-1} which suggests that the flakes are trilayer.

Following optical characterisation, FET devices are fabricated using high-quality WS_2 flakes. The samples are spin-coated with 500 nm of PMMA and baked 30 minutes at 160°C to obtain hard PMMA surface to protect flakes from any contamination during the scribing process. Then, they are scribed to pieces less than 5 mm length and width to fit them into the chip carrier and measurement probes. The PMMA is subsequently removed with acetone and IPA. Using the previously described lithography, deposition (6/65 nm of Cr/Au) and lift-off techniques in Chapter 3, transistors with channel length ranging from 200 nm to 2.5 μm are defined, see Figure 4.1d and e, allowing the electrical transport properties of CVD grown WS_2 flakes to be investigated.

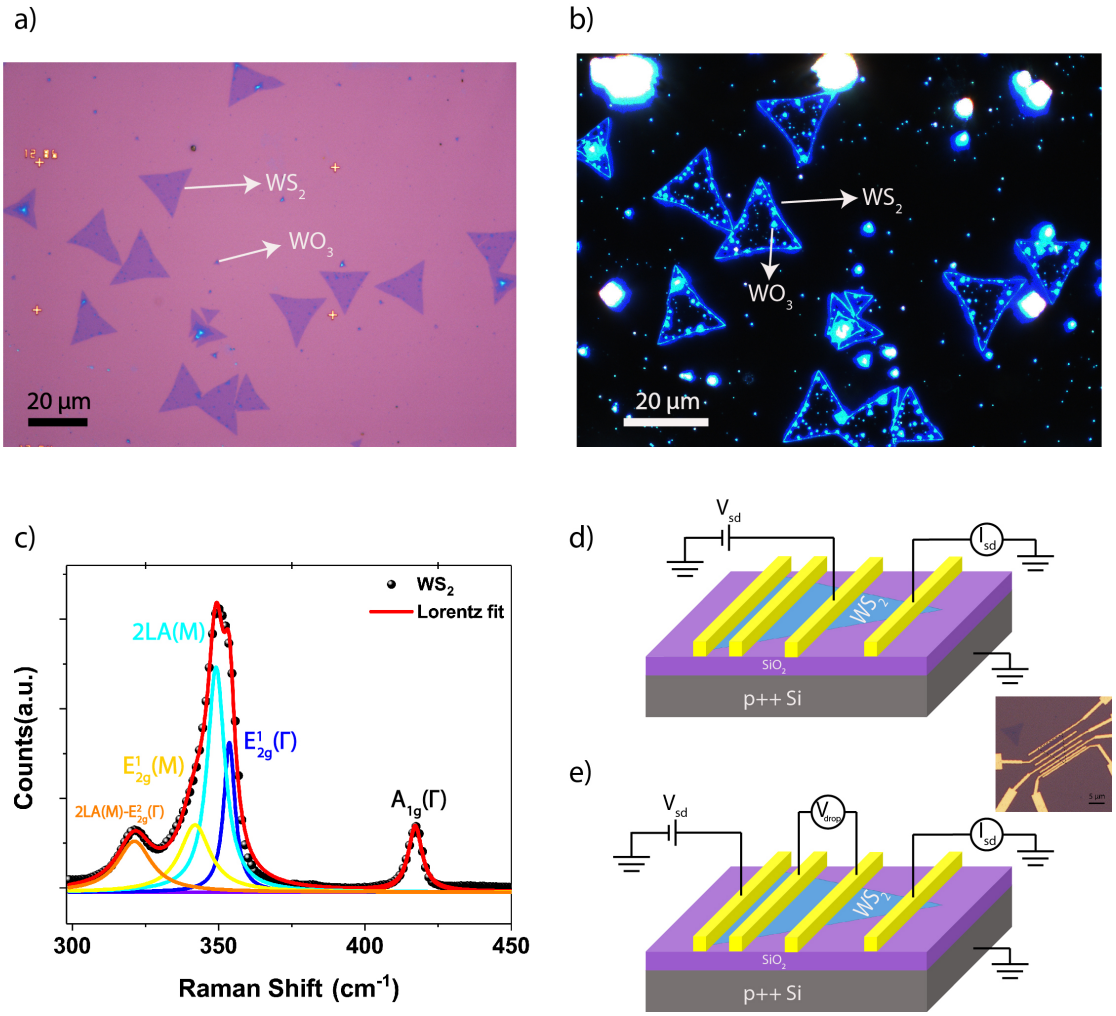

Figure 4.1: (a) Optical microscope and (b) dark field microscopy images of the WS_2. Triangular shapes are the flakes and the bright spots in (b) are the WO_3 seeds from the growth process. The sizes of the flakes can change from 5 μm to 30 μm. (c) Raman spectra of the flakes. (d) Schematic of two-probe and (e) four-probe measurements. The yellow rectangles represent the Cr/Au contacts. The inset is the optical microscope image of a fabricated device, scale bar 5 μm. The WS_2 is centred and under the metal contacts.

4.3 Results

I use two-probe and four-probe techniques to characterise the flakes electrically. Each channel is biased separately to identify the two-probe resistance at room temperature and 4.2 K. The results are compared with four-probe resistance to extract the resistance of the semiconductor.

The contact resistance can be calculated using source-drain (I - V) characteristics of WS_2. The flakes are triangular, therefore I need to consider changes of the width along with the channel length. The total resistance is given by the slope of a I - V curve which is

$$R_{total} = 2R_c(W) + R_{channel}(W) + 2R_{Cr/Au} \tag{4.2}$$

where R_c is the resistance between the metal and the semiconductor, $R_{channel}$ is the resistance of the channel and $R_{Cr/Au}$ is the resistance of Cr/Au contacts. The resistance of the semiconductor is $R_{channel} = \rho_{channel}L/W$ where L and W are the channel length and width, $\rho_{channel}$ is the resistivity of the semiconductor. The total resistance considers all of the resistive components of the measurement system.

A source-drain bias is applied to the devices recording the current with channel lengths ranging from 0.2 to 2.3 μm, see Figure 4.2a. With the change of quasi-Fermi level, a semiconductor device acts as a metal above turn-on voltages due to the high electrostatic doping. The resistance of the WS_2 is investigated at the point above the turn-on voltages where the sufficient current (1 nA or larger) passes through the channel.

The two-probe measurements at room temperature show resistances larger than MΩ which is dominated by the contact resistance, see Figure 4.2a and b. To confirm this, the resistance of the flake is determined with a four-probe measurement, and it is found to be in the kΩ range. The contribution to the total resistance from the resistance of the metallic contacts can be neglected because it is orders of magnitude smaller than the resistance of the channel. As a result of this, contact resistance

can be rewritten as

$$R_{total} = 2R_c(W), \qquad R_c(W) = \frac{R_{total}}{2}. \tag{4.3}$$

The dependence of the width is considered with extracting the contact resistivity from $R_c = R_c.W$. The lowest contact resistance found is 22.2 MΩ μm ± 18.4 MΩ μm. This contact resistance is not comparable with the sheet resistance of the flake. Therefore, the total resistance has no linear increase with the channel length.

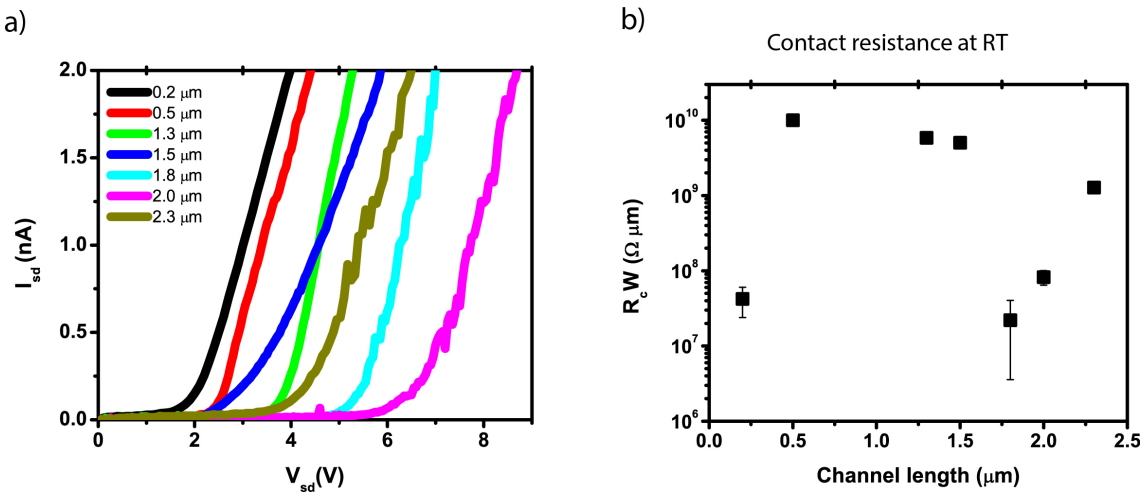

Figure 4.2: (a) Source-drain measurement of a few-layer CVD WS_2 device with different channel lengths. (b) Contact resistances of these channel lengths.

The devices are subsequently annealed in liquid helium under a large source-drain current. I apply a large and fast sweep of source-drain bias up to 210 V and the currents reaching up to 10 μA lasting for a few seconds. Joule heating is commonly used to remove contaminants and adsorbates from the surface of atomically thin materials [14, 15]. A high rate of device failure is observed during the Joule heating process. After the annealing, the total resistance is reduced by two orders of magnitude, see Figure 4.3a. This indicates that the metal-WS_2 interface is affected by the presence of contaminants and possibly an oxide barrier.

After the improvement in the contacts with the annealing, the source-drain bias is applied to observe the total resistances of the devices, see Figure 4.3c. The contact resistances are calculated. Even though the current annealing is performed,

the contact resistance remains high. The lowest calculated contact resistance is 0.77 MΩ μm $\pm$ 53.9 kΩ μm, see Figure 4.3d.

Sweeping the back gate allows different energy levels in the band structure to be accessed. However, the device does not provide any gate sweep dependence even when the gate is biased to 100 V and source-drain is biased to 30 V. Subsequently, I transfer the flakes to a new Si/SiO_2 substrate by dry transfer method, see Chapter 3, and applied a voltage bias. Also in this case, the gate does not show any modulation of the electrical properties of the TMDCs, see Figure 4.3b. This might be due to the large Fermi level pinning in the devices [16].

4.4 Conclusion

I have examined metal-WS_2 interface with electrical transport measurements. The high contact resistance at the interface isolated the resistance of the WS_2. The possible contamination, impurities and defects were cleaned by the bias annealing in liquid helium. However, the contact resistance was not only due to these impurities. The Schottky barrier, Fermi level pinning, van der Waals gap and the lattice mismatch between the metal and the semiconductor could be the reason of the high resistance which has been reported previously [4, 8, 16–18]. Strong Fermi level pinning could prevent the gate modulation. It might be possible to improve the quality of the contacts with further doping, intercalating and phase change methods, and the vacuum annealing might allow to clean any contaminants on the surface leading lower contact resistances.

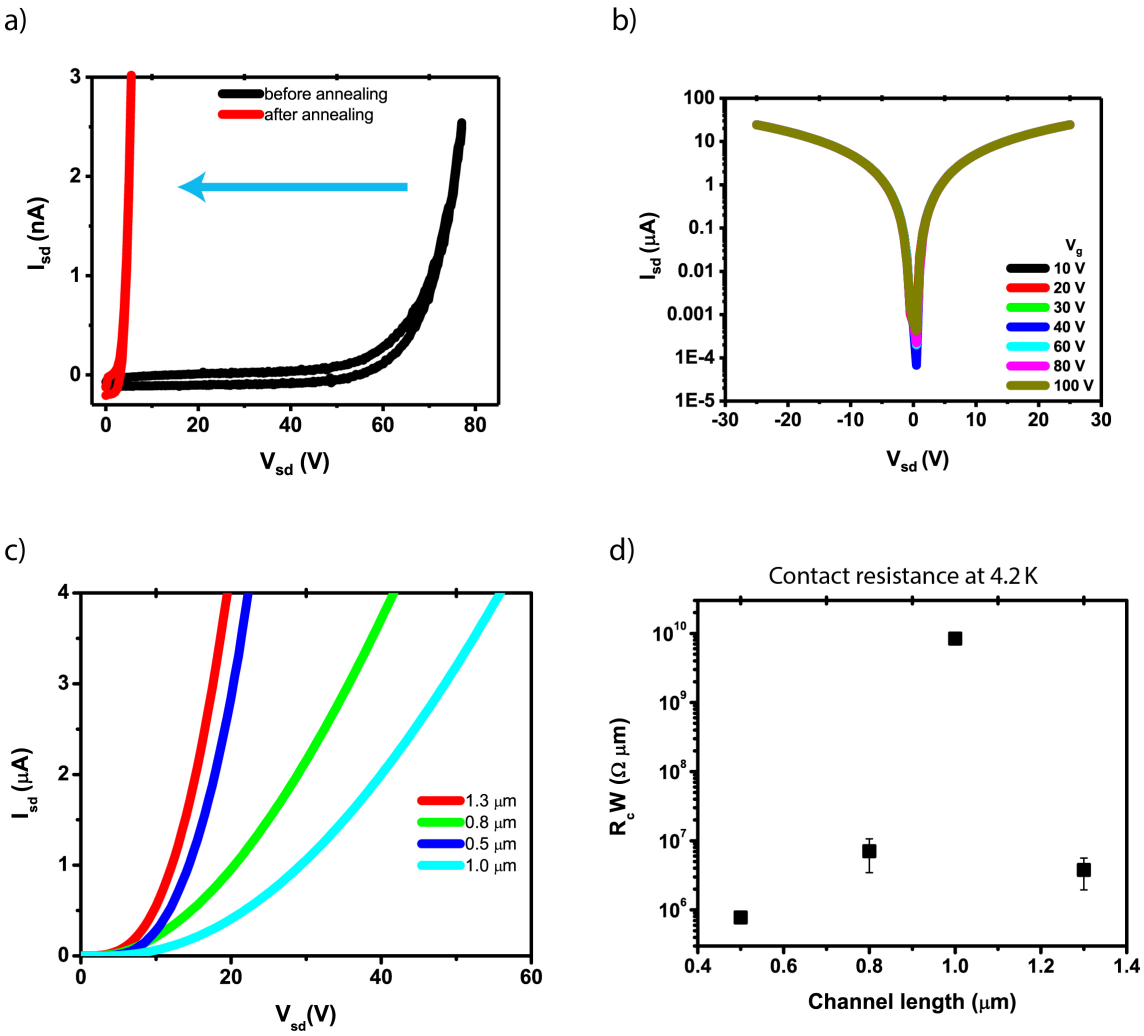

Figure 4.3: (a) Source-drain bias annealing of the devices at 4.2 K. The black and red curve represent the transport before and after the annealing respectively. (b) Current (absolute value) vs voltage at different back gate biases. The green single line shows all the measurements are overlapping each other and cannot be distinguished. (c) Source-drain measurements in liquid helium for difference channel lengths. (d) Calculated contact resistances of the device.

Bibliography

[1] D. Jena, K. Banerjee, and G. H. Xing, "Intimate contacts," *Nature Materials*, vol. 13, no. 12, pp. 1076–1078, 2014.

[2] K. Jia, Y. Su, J. Zhan, K. Shahzad, H. Zhu, C. Zhao, and J. Luo, "Enhanced end-contacts by helium ion bombardment to improve graphene-metal contacts," *Nanomaterials*, vol. 6, no. 9, p. 158, 2016.

[3] H. J. Chuang, B. Chamlagain, M. Koehler, M. M. Perera, J. Yan, D. Mandrus, D. Tománek, and Z. Zhou, "Low-resistance 2D/2D ohmic contacts: A universal approach to high-performance WSe_2, MoS_2, and $MoSe_2$ transistors," *Nano Letters*, vol. 16, no. 3, pp. 1896–1902, 2016.

[4] L. Yang, K. Majumdar, H. Liu, Y. Du, H. Wu, M. Hatzistergos, P. Y. Hung, R. Tieckelmann, W. Tsai, C. Hobbs, and P. D. Ye, "Chloride molecular doping technique on 2D materials: WS_2 and MoS_2," *Nano Letters*, vol. 14, pp. 6275–6280, 2014.

[5] R. Kappera, D. Voiry, S. E. Yalcin, B. Branch, G. Gupta, A. D. Mohite, and M. Chhowalla, "Phase-engineered low-resistance contacts for ultrathin MoS_2 transistors," *Nature Materials*, vol. 13, pp. 1–15, Aug 2014.

[6] M. H. D. Guimarães, H. Gao, Y. Han, K. Kang, S. Xie, C. J. Kim, D. A. Muller, D. C. Ralph, and J. Park, "Atomically thin ohmic edge contacts between two-dimensional materials," *ACS Nano*, vol. 10, no. 6, pp. 6392–6399, 2016.

[7] S. Datta, *Electronic Transport in Mesoscopic Systems*. Cambridge: Cambridge University Press, 1995.

[8] A. Allain, J. Kang, K. Banerjee, and A. Kis, "Electrical contacts to two-dimensional semiconductors," *Nature Materials*, vol. 14, no. 12, pp. 1195–1205, 2015.

[9] J. Kang, W. Liu, D. Sarkar, D. Jena, and K. Banerjee, "Computational study of metal contacts to monolayer transition-metal dichalcogenide semiconductors," *Physical Review X*, vol. 4, no. 3, p. 031005, 2014.

[10] S. Wang, Y. Rong, Y. Fan, M. Pacios, H. Bhaskaran, K. He, and J. H. Warner, "Shape evolution of monolayer MoS_2 crystals grown by chemical vapor deposition," *Chemistry of Materials*, vol. 26, pp. 6371–6379, 2014.

[11] A. Berkdemir, H. R. Gutiérrez, A. R. Botello-Méndez, N. Perea-López, A. L. Elías, C.-I. Chia, B. Wang, V. H. Crespi, F. López-Urías, J.-C. Charlier, H. Terrones, and M. Terrones, "Identification of individual and few layers of WS_2 using Raman spectroscopy," *Scientific Reports*, vol. 3, p. 1755, Apr 2013.

[12] F. Withers, O. Del Pozo-Zamudio, S. Schwarz, S. Dufferwiel, P. M. Walker, T. Godde, A. P. Rooney, A. Gholinia, C. R. Woods, P. Blake, S. J. Haigh, K. Watanabe, T. Taniguchi, I. L. Aleiner, A. K. Geim, V. I. Fal'Ko, A. I. Tartakovskii, and K. S. Novoselov, "WSe_2 light-emitting tunneling transistors with enhanced brightness at room temperature," *Nano Letters*, vol. 15, no. 12, pp. 8223–8228, 2015.

[13] A. A. Mitioglu, P. Plochocka, G. Deligeorgis, S. Anghel, L. Kulyuk, and D. K. Maude, "Second-order resonant Raman scattering in single-layer tungsten disulfide WS_2," *Physical Review B - Condensed Matter and Materials Physics*, vol. 89, no. 24, pp. 1–5, 2014.

[14] J. Moser, A. Barreiro, and A. Bachtold, "Current-induced cleaning of graphene," *Applied Physics Letters*, vol. 91, no. 16, pp. 1–4, 2007.

[15] F. Withers, T. H. Bointon, D. C. Hudson, M. F. Craciun, and S. Russo, "Electron transport of WS_2 transistors in a hexagonal boron nitride dielectric environment," *Scientific Reports*, vol. 4, p. 4967, May 2014.

[16] R. T. Tung, "Chemical bonding and fermi level pinning at metal-semiconductor interfaces," *Physical Review Letters*, vol. 84, no. 26 Pt 1, pp. 6078–6081, 2000.

[17] F. Xia, V. Perebeinos, Y.-m. Lin, Y. Wu, and P. Avouris, "The origins and limits of metal-graphene junction resistance," *Nature Nanotechnology*, vol. 6, no. 3, pp. 179–184, 2011.

[18] Y. Liu, P. Stradins, and S.-H. Wei, "Van der Waals metal-semiconductor junction: Weak Fermi level pinning enables effective tuning of Schottky barrier," *Science Advances*, vol. 2, no. 4, p. e1600069, 2016.

Chapter 5

Side gate leakage and field emission in graphene FETs

5.1 Introduction

SiO_2/Si is typically used as a back gate for graphene field-effect transistors to apply a vertical electric field allowing modulation of the Fermi level. A top gate can also be added to increase the electric field and capacitive modulation. Risk of failure in the device becomes higher with the addition of the complexity [1, 2]. However, side gates can be used as an alternative gating mechanism to reduce the interaction with the dielectric, avoid dielectric breakdown and top-gate related hysteresis [3]. One of the main weakness of side gate devices is the leakage between the channel and the gate from dielectric/air or dielectric/vacuum environment [4]. Graphene side gates and their horizontal transport properties on a dielectric surface are interesting problems. In previous studies with graphene side gates separated by a couple of hundreds of nanometres distance on SiO_2 gate, the I - V characteristics of the graphene flake are governed by the space-charge-limited flow of current at low bias, whilst at higher

The results in this chapter have been published as A. Di. Bartolomeo, F. Giubileo, L. lemmo, F. Romeo, S. Russo, S. Unal, M. Passacantando, V. Grossi and A. M. Cucolo, *Applied Physics Letters* **109**, 2, 023510, (2016) which the author of this thesis is a co-author. Contributions were made to the design, fabrication and characterisation of the devices.

bias Fowler-Nordheim tunnelling dominates [5, 6]. It has also been found that field emission between suspended graphene flakes is based on Fowler-Nordheim field emission [7].

In this chapter, the role of side gates situated 100 nm laterally away from the graphene channel is studied. First, the device is electrically characterised in ambient conditions. After that, the graphene side gate transport properties are studied in a SEM chamber providing high vacuum conditions. The leakage to the side gate is directed through the SiO_2 substrate and the vacuum environment. At low voltage regime less than 58 V, the leakage is due to Fowler-Nordheim emission. Furthermore, with the applied bias, the leakage rises sharply due to the contribution of Frenkel-Poole transport. The reason for this is high electric field emission in the measurement environment.

5.2 Experimental details

Graphene is exfoliated on Si/SiO_2 substrate and identified under an optical microscope using the green light contrast analysis, see Figure 5.1a [8]. The graphene side gates and channels are defined by electron beam lithography. In order to define high precision sub-micrometre gate distances, a thin layer of PMMA is used as a mask prior to the lithography and developed short time in IPA:MIBK:MEK following electron beam exposure, see Chapter 3. The desired side gates are obtained by O_2 reactive ion plasma etching which removes regions of graphene not masked by PMMA. This allows side gate structures to be fabricated with a desired gate distance to be obtained. Following the removal of the PMMA mask in hot acetone, 20/90 nm of Cr/Au metal contacts are defined and deposited by the lithography, thermal evaporation and lift off. The fabricated device has two graphene channels connected in series by a metal line. Each graphene channel has its own side gate which can be tuned independently of one another, see Figure 5.1b and c. They can also be used individually as a graphene field-effect transistor.

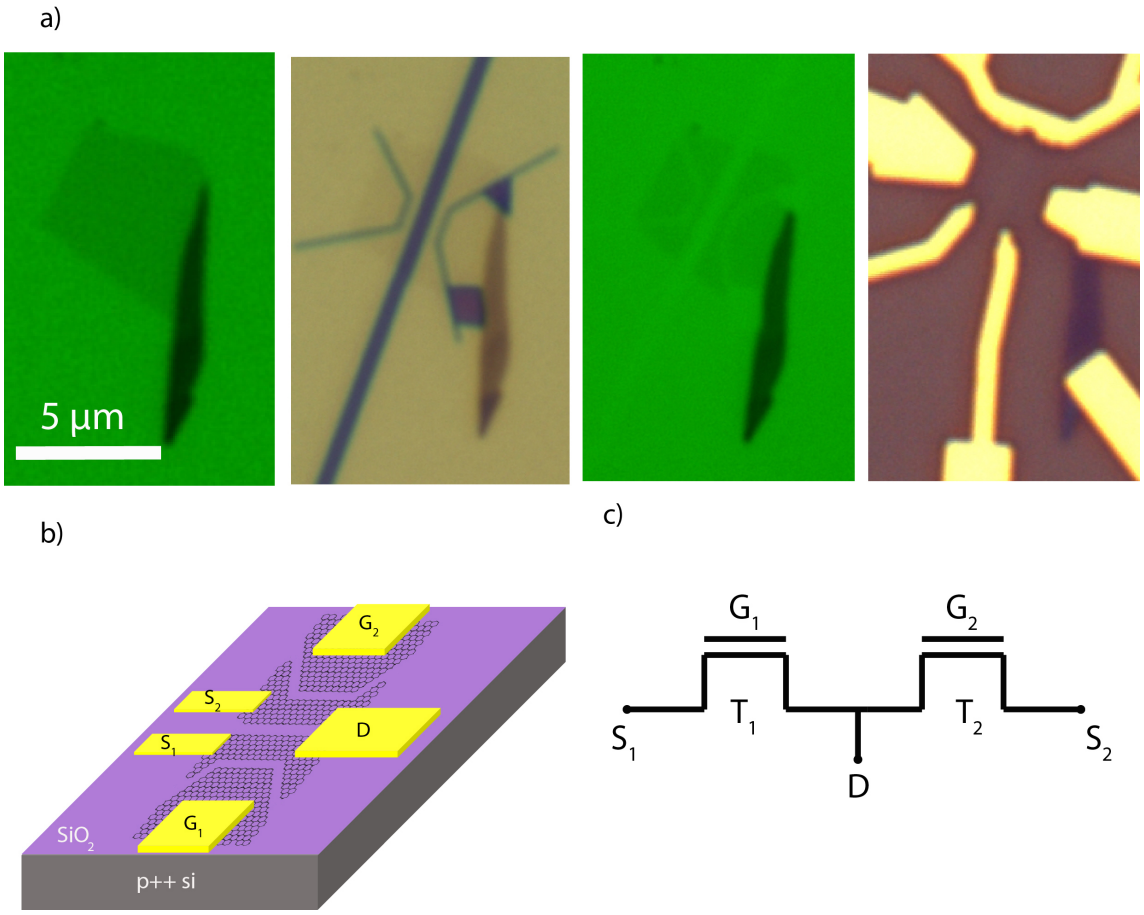

Figure 5.1: (a) Optical microscope images with a green filter. The first image from left shows the exfoliated graphene, the second one is the image after the lithography and developing processes. Etched graphene and the contacts on the side gate and source-drain are shown in third and fourth. (b) Schematic of the device, S_1 and S_2 are the contacts used for source and drain. D is the connection which couples the two flakes in series. G_1 and G_2 are the gate electrodes. (c) The circuit schematic of the device. T_1 and T_2 represent the first and the second graphene field-effect transistor.

5.3 Results

The device is electrically characterised in a Janis probe station at a pressure of $\sim$ 1 Torr. In order to achieve clean surface and remove the contaminants, the sample is vacuum annealed at $\sim 10^{-6}$ Torr and kept at room temperature more than three days in a nanoprobe integrated high-vacuum Zeiss SEM chamber. The gate leakage and field emission are measured in-situ using a Keithley 4200 sourcemeter.

Initially the electrical transport properties of the side-gated graphene FETs are investigated in ambient conditions. While floating the back gate, the source-drain current is recorded whilst sweeping the source-drain bias for various side gate voltages, see Figure 5.2a. Then, the side gate is swept at constant source-drain voltage (9 mV) to obtain the change in the resistance of the device with modulation of the side gate bias, see Figure 5.2b. A similar measurement is also performed on the back gate, see Figure 5.2c. The minimum resistance ($\sim$ 50 kΩ) at the highly doped region is dominated by the channel. Measurements on test devices in the same chip shows 1 kΩ μm contact resistance which is expected for the graphene/Cr contacts Figure 5.2 [9, 10]. The Dirac point is located at $V_{sg} \sim 0.35$ V representing a p-doped device. Hysteresis on the Figure 5.2b shows $\sim$ 20% ratio of the difference in the voltage shift and width between forward and reverse sweep at R = 65 kΩ, whereas the back gate measurements indicate the ratio of $\sim$ 39% at the same resistance point. This hysteresis is due to the traps in the gate, residues of PMMA or contamination of the surface, e.g. by water molecules, which might reduce the performance of the side gate. In order to increase the functionality of the device, the measurements are performed in a vacuum chamber, a contamination free environment, and the bias on the side gate is kept low to avoid any leakage and degradation in the SiO_2.

The side gate sweeps show that the graphene has a p-type behaviour. This is confirmed by the back gate measurements. The Dirac point is located at $V_{bg} = 10$ V. A second Dirac point appears here which might be due to the doping of the contacts, oxide traps and Fermi-level de-pinning which have been observed previously [11–13]. This peak does not appear on the side gate sweeps up to 3 V.

The normalised transconductance, $G_m = (dI_D/dV_G)_{V_d=9mV}$ is calculated for side gate and back gate measurements to compare their effect on the channel and efficiency to modulate the transconductance, see Figure 5.2d and e. The efficiency of the side gate is 5 to 10 times higher than the back gate under a much larger back gate bias.

In order to identify the mechanism behind the transport between the side gate and the graphene flake, the horizontal current between the two is measured in a high vacuum environment to avoid any surface water, moisture and contamination until the device breakdown. Before beginning this measurement, the leakage in the back gate is checked on the graphene channel and the side gate which is about 0.1 nA up to 100 V. The low leakage from the back gate might permit measuring the side gate leakage. Then, the graphene flake is biased up to 100 V monitoring the current while the side gate is grounded, see Figure 5.3a.

The leakage current between the flake and side gate is measured under a 50 V back gate bias, see Figure 5.3b. To stabilise the current in the graphene channel multiple low bias sweeps were performed prior to the measurement. Then, the 2nd sweep is performed, see Figure 5.3b. An obvious separation in leakage current occurs at $V_D = 15$ V. The side gate leakage becomes higher than the back gate. Moreover, a sharp increase is observed at 60 V which can be interpreted as tunnelling between graphene to graphene through SiO_2 or vacuum. A slow degradation happens after 70 V, and this degradation continuous in the third sweep. The high rate of the leakage might indicate a different mechanism.

The mechanism behind the leakage is investigated with comparing the low and the high voltage regimes. In a similar device, it has been previously found that low voltage regime is governed by the space-charge-limited flow where the current is dominated by the free flow of the charge carriers in the insulator [6, 14]. However, a better approximation can be observed with Frenkel-Poole transport in low voltage regime [5, 15]. In this case, defects and trap states in SiO_2 limit the current passing through the oxide [16, 17]. Electrons injected into this insulator can be trapped by these states and pass to another trapping site under an electric field. The current

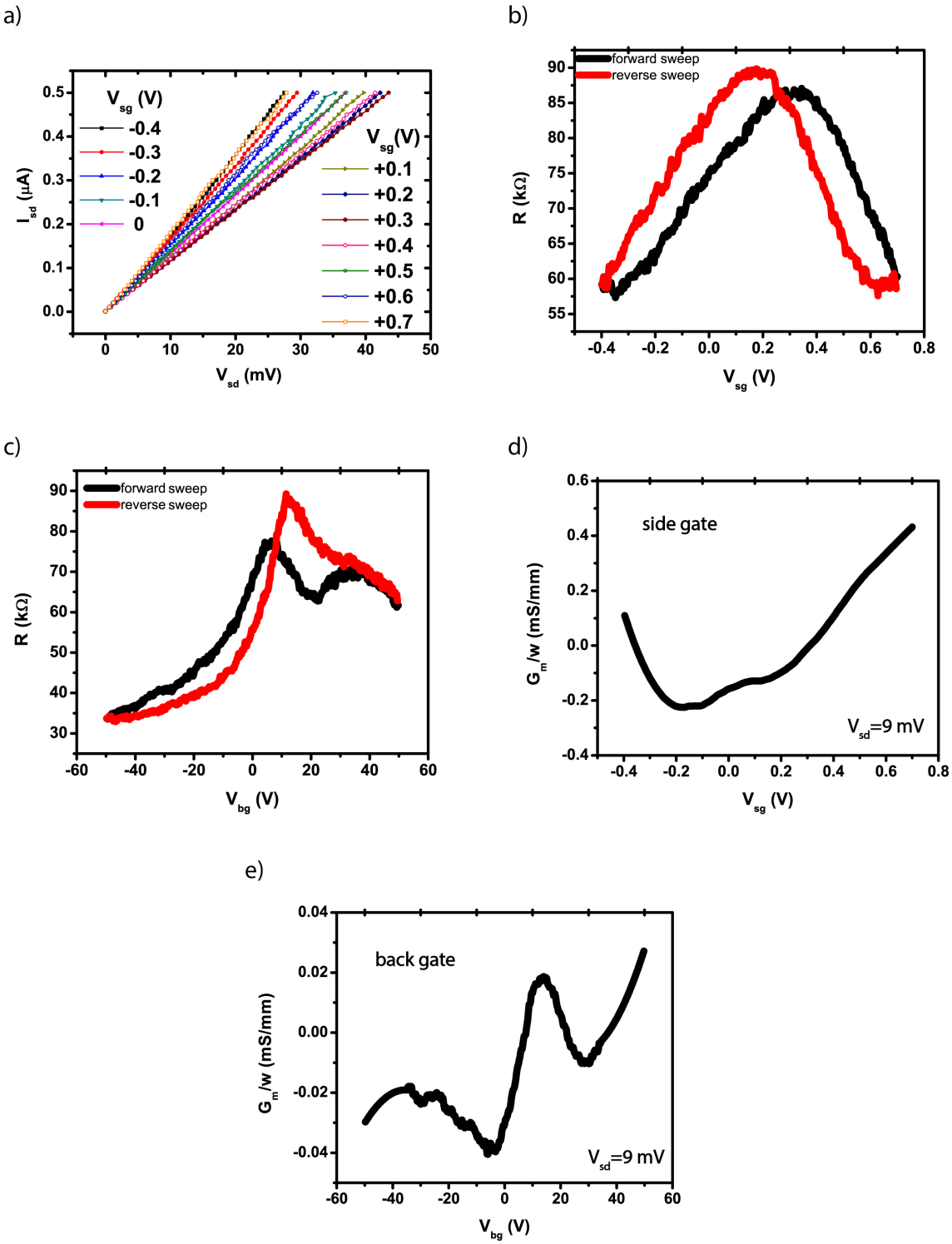

Figure 5.2: Electrical characterisation of T_1 graphene channel. (a) Source-drain measurements at different side gate biases. (b) The resistance of the channel as a function of side gate and (c) back gate bias at 9 mV constant source-drain voltage. (d) Side gate and (e) back gate transconductance normalised by channel width.

is given as

$$I_D \propto V_D exp\left(\frac{e}{kT}\left(2\alpha\sqrt{V_D} - \phi_B\right)\right) \tag{5.1}$$

where I_D and V_D are the current and the applied bias, e is the electron charge, k is the Boltzmann constant, T is the temperature, α is the Frenkel-Poole constant ($\alpha = \sqrt{\frac{q}{4\pi\varepsilon_0\varepsilon_r d}}$), ε_r is the dielectric constant of SiO_2, ε_0 is the vacuum permittivity, d is the thickness of the dielectric and ϕ_B is the trap potential barrier [5, 18]. The fit of Figure 5.3c shows a linear behaviour which is expected for the Frenkel-Poole model. Using this, the trap barrier can be calculated from the intercept ($e\phi_B/kT$) of the fit which is $\phi_B \sim 0.8$ V for both sweeps. Similar trap barrier energies have been previously reported for SiO_2 [19–21]. The conduction mechanism is due to the injection of electrons into the trap states via SiO_2. Electrons can be excited to the conduction band by the large electric field and transferred to the graphene.

The Fowler-Nordheim emission is observed as a dominant transport mechanism at voltages higher than 58 V. Carriers tunnel through a thick oxide barrier or vacuum when an electric field is applied to an electrode in vacuum [17, 22]. The current in this transport can be described as

$$I \propto a\frac{1}{\phi}\left(\frac{\beta V}{d}\right)^2 exp\left(\frac{b\phi^{3/2}d}{\beta V}\right) \tag{5.2}$$

where $b = 6.83\times10^9$ $e\mathrm{V}^{3/2}$.V/m and $a = 1.54\times10^{-6}$ $e\mathrm{V}^{-1}$ are the constants, d is the thickness of the dielectric, ϕ is the trap barrier height (work function of graphene is 4.5 eV) and β is the field enhancement factor on the edge of graphene which can be calculated from slope of Figure 5.3d as ~ 4 [18, 22]. The Figure 5.3d inset shows $ln(I/V^{3/2})$ versus V^{-1} plot. Even though Equation 5.2 is the general representation of the Fowler-Nordheim emission, the prefactor V^2 can be replaced by $V^{3/2}$ for the graphene [23, 24]. It is found that Fowler-Nordheim model is the closest to the presented results between 58 V and 71 V.

Figure 5.4a shows low bias transport between graphene and the side gate. Electron injected in the SiO_2 moves from the trap and defect states by trapping and de-

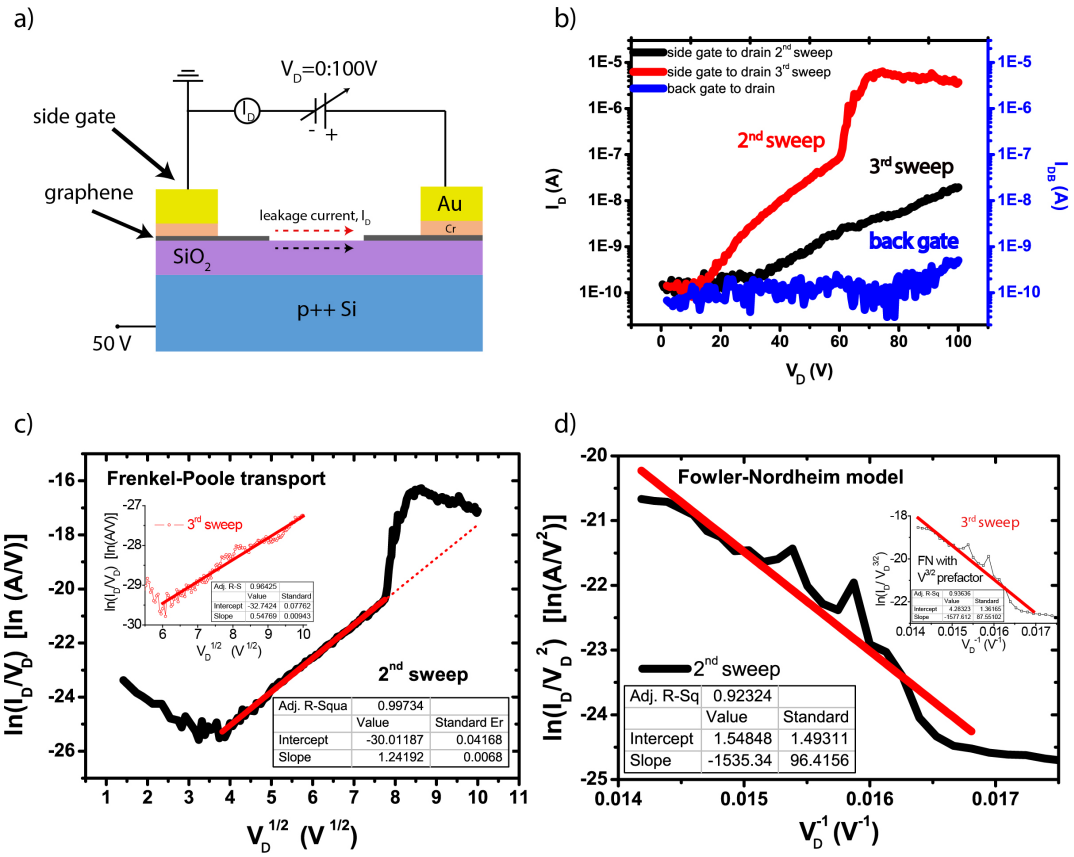

Figure 5.3: (a) Schematic of the side gate leakage measurement. (b) The planar current between side gate and the graphene flake (I_D, left axis). the blue line is the back gate leakage up to 100 V for T_1. The red is the second sweep which is acquired after a couple of low voltage sweeps. The leakage current in 2^{nd} sweep has three steps. The first is the increase in the leakage starting at $V_D = 15$ V, the second is the sharp increase at 58 V and the third is the current degradation at $V_D = 71$ V. The black line (3^{rd} sweep) shows a repetition of the 2^{nd} one. (c) Frenkel-Poole model fit of the 2^{nd} sweep and (inset) 3^{rd} sweep up to $V_D \sim 60$ V. (d) Fit of Fowler-Nordheim field emission model of the 2^{nd} and (inset) 3^{rd} sweep between 58 V and 71 V, adapted from [23].

trapping events under an electric field which is described by Frenkel-Poole transport. There is another mechanism taking place at higher biases which is Fowler-Nordheim tunnelling. It governs the transport between 58 V and 71 V. In this regime, electrons travel in the vacuum since current flow is not limited by any scattering process (capture or emission), see Figure 5.4b. SiO_2 acts as a triangular barrier which the carriers can tunnel through [17]. The degradation after 71 V might be the result of Joule heating in carbon atoms or current modification of carbon edges which was previously reported [25, 26].

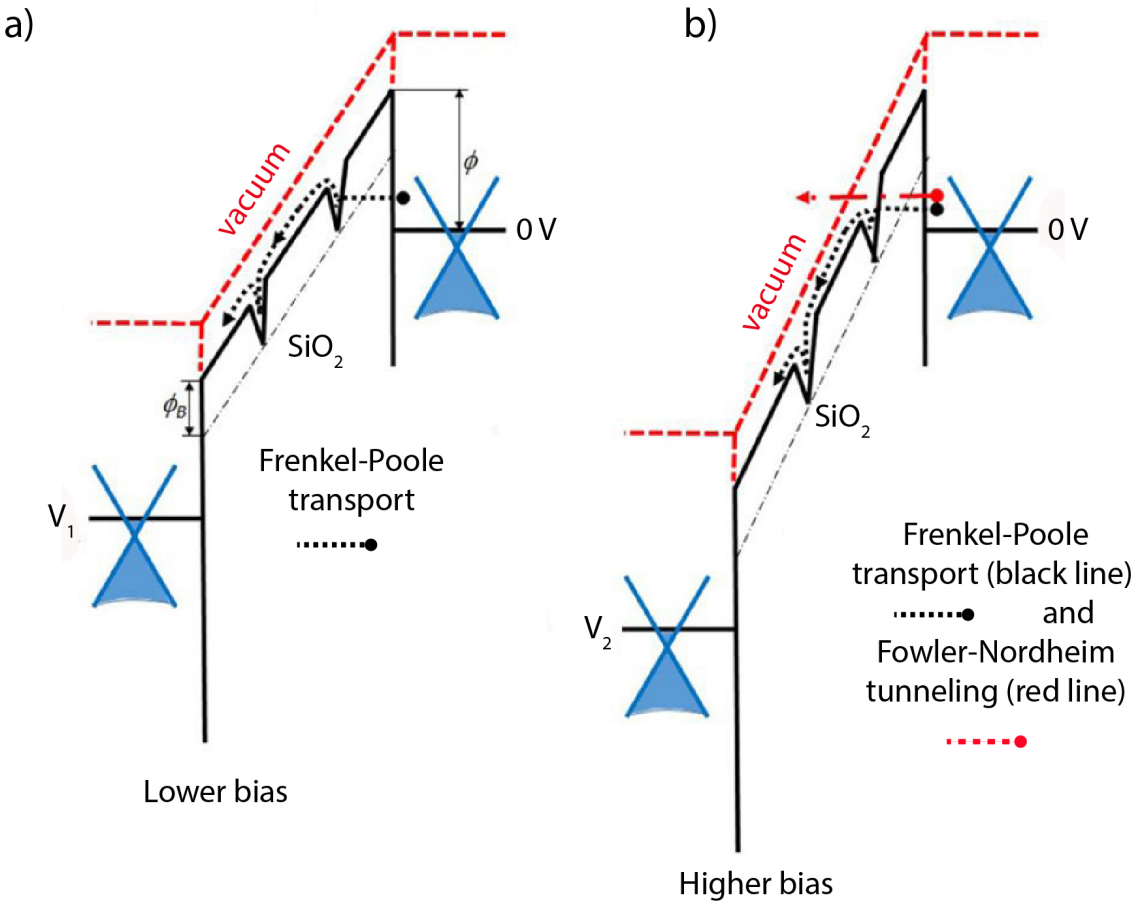

Figure 5.4: (a) Schematic diagram of Frenkel-Poole transport at biases lower than 58 V and (b) Fowler-Nordheim tunnelling and transport in the vacuum. Fowler-Nordheim tunnelling is more favourable than Frenkel-Poole transport at higher biases, adapted from [23].

5.4 Conclusion

In summary, graphene field-effect transistors have been fabricated along with a graphene side gate. One of the advantages of this structure is the possibility to pattern the gate and contact electrodes in a single lithography and etching step. In order to efficiently gate and increase the electric field between the side gate and the channel, the distance between the two was kept 100 nm, and the channel width was 500 nm. The comparison between the side gate and the back gate has shown that the side gate sweeps were 5 to 10 times more efficient than the back gate. The leakage mechanism between the channel and the side gate has been investigated. The leakage at low voltage bias regimes was caused by Frenkel-Poole transport and Fowler-Nordheim emission at higher biases with high electron field emission in a vacuum environment. This work has shown that the graphene side gates can be used as an alternative gating technique to the top or the back gate configurations and bringing additional benefits such as it can be produced easy and fast fabrication techniques.

Bibliography

[1] M. C. Lemme, T. J. Echtermeyer, M. Baus, and H. Kurz, "A graphene field-effect device," *IEEE Electron Device Letters*, vol. 28, pp. 282–284, Apr 2007.

[2] I. Meric, M. Y. Han, A. F. Young, B. Ozyilmaz, P. Kim, and K. L. Shepard, "Current saturation in zero-bandgap, top-gated graphene field-effect transistors," *Nature Nanotechnology*, vol. 3, no. 11, pp. 654–659, 2008.

[3] C. T. Chen, T. Low, H. Y. Chiu, and W. Zhu, "Graphene-side-gate engineering," *IEEE Electron Device Letters*, vol. 33, no. 3, pp. 330–332, 2012.

[4] X. Li, X. Wu, M. Sprinkle, F. Ming, M. Ruan, Y. Hu, C. Berger, and W. A. de Heer, "Top- and side-gated epitaxial graphene field effect transistors," *Physica Status Solidi (a)*, vol. 207, no. 2, pp. 286–290, 2010.

[5] J. Frenkel, "On pre-breakdown phenomena in insulators and electronic semiconductors," *Physical Review*, vol. 54, no. 8, pp. 647–648, 1938.

[6] H. M. Wang, Z. Zheng, Y. Y. Wang, J. J. Qiu, Z. B. Guo, Z. X. Shen, and T. Yu, "Fabrication of graphene nanogap with crystallographically matching edges and its electron emission properties," *Applied Physics Letters*, vol. 96, p. 023106, Dec 2010.

[7] S. Kumar, G. S. Duesberg, R. Pratap, and S. Raghavan, "Graphene field emission devices," *Applied Physics Letters*, vol. 105, p. 103107, Sep 2014.

[8] M. F. Craciun, S. Russo, M. Yamamoto, J. B. Oostinga, A. F. Morpurgo, and S. Tarucha, "Trilayer graphene is a semimetal with a gate-tunable band overlap," *Nature Nanotechnology*, vol. 4, no. 6, pp. 383–388, 2009.

[9] S. Russo, M. F. Craciun, M. Yamamoto, A. F. Morpurgo, and S. Tarucha, "Contact resistance in graphene-based devices," *Physica E: Low-Dimensional Systems and Nanostructures*, vol. 42, no. 4, pp. 677–679, 2010.

[10] A. Di Bartolomeo, F. Giubileo, F. Romeo, P. Sabatino, G. Carapella, L. Iemmo, T. Schroeder, and G. Lupina, "Graphene field effect transistors with niobium contacts and asymmetric transfer characteristics," *Nanotechnology*, vol. 26, no. 47, p. 475202, 2015.

[11] A. Di Bartolomeo, F. Giubileo, S. Santandrea, F. Romeo, R. Citro, T. Schroeder, and G. Lupina, "Charge transfer and partial pinning at the contacts as the origin of a double dip in the transfer characteristics of graphene-based field-effect transistors," *Nanotechnology*, vol. 22, no. 27, p. 275702, 2011.

[12] F. Xia, V. Perebeinos, Y.-m. Lin, Y. Wu, and P. Avouris, "The origins and limits of metal-graphene junction resistance," *Nature Nanotechnology*, vol. 6, no. 3, pp. 179–184, 2011.

[13] J. Knoch, Z. Chen, and J. Appenzeller, "Properties of metal-graphene contacts," *IEEE Transactions on Nanotechnology*, vol. 11, no. 3, pp. 513–519, 2012.

[14] G. Wright, "Mechanisms of space-charge-limited current in solids," *Solid-State Electronics*, vol. 2, no. 2-3, pp. 165–189, 1961.

[15] S. M. Sze, "Current transport and maximum dielectric strength of silicon nitride films," *Journal of Applied Physics*, vol. 38, pp. 2951–2956, Jun 1967.

[16] H. Schroeder, "Poole-Frenkel-effect as dominating current mechanism in thin oxide films-An illusion?!," *Journal of Applied Physics*, vol. 117, p. 215103, Jun 2015.

[17] A. W. Strong, E. Y. Wu, R. P. Vollertsen, J. Suñé, G. L. Rosa, S. E. Rauch III and T. D. Sullivan, *Dielectric Characterization and Reliability Methodology*, pp. 71–208. Hoboken, NJ, USA: John Wiley & Sons, Inc., 2009.

[18] S. Sze and K. K. Ng, *Physics of Semiconductor Devices*. Hoboken, NJ, USA: John Wiley & Sons, Inc., Oct 2006.

[19] H. Krause, "Poole-Frenkel currents in thermally grown SiO_2 films," *Physica Status Solidi (a)*, vol. 74, pp. 151–154, Dec 1982.

[20] S. A. DiBenedetto, A. Facchetti, M. A. Ratner, and T. J. Marks, "Charge conduction and breakdown mechanisms in self-assembled nanodielectrics," *Journal of the American Chemical Society*, vol. 131, pp. 7158–7168, May 2009.

[21] W. Harrell and J. Frey, "Observation of PooleFrenkel effect saturation in SiO_2 and other insulating films," *Thin Solid Films*, vol. 352, pp. 195–204, Sep 1999.

[22] R. H. Fowler and L. Nordheim, "Electron emission in intense electric fields," *Proceedings of the Royal Society A: Mathematical, Physical and Engineering Sciences*, vol. 119, no. 781, p. 173, 1928.

[23] A. Di Bartolomeo, F. Giubileo, L. Iemmo, F. Romeo, S. Russo, S. Unal, M. Passacantando, V. Grossi, and A. M. Cucolo, "Leakage and field emission in side-gate graphene field effect transistors," *Applied Physics Letters*, vol. 109, no. 2, p. 023510, 2016.

[24] R. G. Forbes and J. H. B. Deane, "Correction for Forbes and Deane, Reformulation of the standard theory of Fowler-Nordheim tunnelling and cold field electron emission," *Proceedings of the Royal Society A: Mathematical, Physical and Engineering Sciences*, vol. 464, no. 2100, pp. 3378–3378, 2008.

[25] A. Di Bartolomeo, A. Scarfato, F. Giubileo, F. Bobba, M. Biasiucci, A. M. Cucolo, S. Santucci, and M. Passacantando, "A local field emission study of partially aligned carbon-nanotubes by atomic force microscope probe," *Carbon*, vol. 45, no. 15, pp. 2957–2971, 2007.

[26] M. Passacantando, F. Bussolotti, S. Santucci, A. Di Bartolomeo, F. Giubileo, L. Iemmo, and A. M. Cucolo, "Field emission from a selected multiwall carbon nanotube," *Nanotechnology*, vol. 19, no. 39, p. 395701, 2008.

Chapter 6

High photoresponsivity in graphene-WS_2 heterostructures

6.1 Introduction

Two-dimensional materials, such as graphene and WS_2, have a great potential in future electronic devices, field-effect transistors and photodetectors with their near-infrared and visible range band gap in the electromagnetic spectrum [1, 2]. At the same time, graphene has high carrier mobility, transparency and broadband operation range, fast optical response time and it can be integrated into optoelectronic devices [3–5].

In this chapter, a photodetector based on a graphene/WS_2 heterostructure with a polymer gate is introduced. The heterostructure is characterised optically and electrically with and without the polymer top gate. SPCM measurements are performed to investigate optical active area on a prototype graphene/bulk WS_2 devices in ambient conditions. The active area of these samples is the heterojunction which produces at least two orders of magnitude higher photocurrent than bare graphene.

The results in this chapter have been accepted for publication in *Advanced Materials* as Jake Mehew, Selim Unal, Elias Torres Alonso, Gareth Jones, Saad Ramadhan, Monica Craciun and Saverio Russo which the author of this thesis is a co-author. Contributions were made to the fabrication, optical characterisation, electrical-optical measurements and preparation of the manuscript.

Subsequently, the EQE and photoresponsivity measurements on graphene/few-layer WS_2 are examined in a home built vacuum chamber integrated with a light and monochromator, see Figure 3.16. The photodetectors operate in the wavelength range of 400-700 nm and the photoresponsivity is 10^6 W/A which is one of the highest recorded in the graphene-TMDC heterostructure devices. The response time of the heterostructure is 2.8 ms and 4.0 ms for the rise and the fall time respectively. These results are confirmed by the bandwidth measurements. With traditional Si/SiO_2 gates, the graphene-TMDC devices show a persistent photocurrent after removal of the light, of interest for memory applications, whereas a high photoresponsive and gain photodetector within the order of millisecond response times is obtained by graphene-WS_2 heterostructure [6].

6.2 Experimental details

WS_2 is mechanically exfoliated on a highly p-doped Si/SiO_2 (290 nm) substrate from a synthetic crystal (HQ Graphene) with purity of 99.995%. The exfoliated areas are covered by a high-quality graphene grown by cold wall chemical vapour deposition technique using wet transfer method [7]. Fully covered flakes are identified by an optical microscope. Few-layer WS_2-graphene is characterised by Renishaw Raman spectroscopy with a 532 nm laser.

Further lithography steps are performed and contact metals are deposited. Three layers of metal are deposited as 25/7/65 nm Au/Cr/Au directly contact to the graphene region only. The graphene channel is further etched using Argon plasma.

After the fabrication of the sample, a solid polymer top gate is prepared by magnetic stirring of poly (ethylene oxide) (PEO) and lithium perchlorate ($LiClO_4$) at a ratio of 8:1 in methanol and drop-cast on the device in ambient conditions.

The device is characterised electrically. Photocurrent maps are obtained on a prototype graphene-bulk WS_2 device in ambient conditions using the photocurrent scanning map, see Chapter 3. Furthermore, other optoelectronic measurements are performed on graphene/few-layer WS_2 in a vacuum chamber with a fused quartz

window, monochromator and a white light source. A Thorlabs PM320E power meter with S130VC sensor is used for power calibration.

6.3 Results

Raman spectra of few-layer WS_2-graphene is acquired using a 532 nm laser beam. High power of the laser can damage the sample and saturate the WS_2 signal. Therefore, a neutral density filter is used inside the Raman system which can reduce the power of the laser down to $\sim$ 39 μW. The peaks are fitted by Lorentzian up to 420 cm^{-1} corresponds to Raman modes of WS_2 and graphene up to 3000 cm^{-1}, see Figure 6.1b. The Raman shift difference in the layer number dependent Raman modes, 2LA and A_{1g}, corresponds to three atomic layer WS_2. Characteristic single layer graphene peaks are observed as well as a broad photoluminescence peak of WS_2 around $\sim$ 3100 cm^{-1}, see Figure 6.1c.

I set up the circuit as shown in Figure 6.1a. Electrical transport is measured by sweeping the top gate at constant source and drain voltage. The Dirac point for graphene can be resolved at $V_{tg} = 0.1$ V, see Figure 6.1d. The maximum sheet resistance of the flake is calculated as $\sim$ 16 k$\Omega/\square$.

The Figure 6.1a inset shows the cross section of the graphene/few-layer WS_2 device. The contact is deposited on the top layer graphene. Ionic polymer serves as a top gate on the heterostructure. The polymer induces higher carrier concentration than the back gate [8–10]. It establishes a few nanometre Debye layer where the impurities between the gate and the device are reduced by mobile ions [11, 12]. When the top gate bias is applied, the mobile ions accumulate to the Au electrode and the graphene surfaces. The bias has to be kept lower than 4 V to avoid any chemical reaction processes and high gate leakage [13]. If the gate is biased negatively, the positive ions, Li^+ accumulates to the electrodes whereas ClO_4^- ions move onto the graphene. The negative ions near the graphene surface dope the graphene p-type increasing hole formation.

The mobility of the graphene is calculated using the applied voltage to the gate

which corresponds to the electrostatic potential (ϕ) difference between the graphene and the gate electrode and Fermi level (E_F) shift [8]. The capacitance of the polymer gate, 2.2 x 10^{-6} F cm^{-2}, is much larger than the back gate (12 nF cm^{-2}) [8, 14]. Therefore, the Fermi energy change in the graphene needs to be considered in the top gate voltage. Then, the applied gate bias can be written as

$$V_{tg} = \frac{E_F}{e} + \phi = \frac{\hbar|\upsilon_F|\sqrt{\pi n}}{e} + \frac{ne}{C_{tg}} \tag{6.1}$$

where e is the electron charge, n is the carrier concentration, υ_F is the Fermi velocity and C_{tg} is the capacitance of the top gate [8]. The gate capacitance, $C_{tg} = \varepsilon\varepsilon_0/d_{tg}$, can be calculated using dielectric constant of PEO ($\varepsilon = 5$) and Debye length (d_{tg}). The carrier concentration is extracted for each V_{tg} solving Equation 6.1 and used to find carrier mobility which is $\sim$ 400 cm^2/Vs. In the case of SiO_2 back gate, the capacitance is much lower than the top gate. Therefore, the number of carriers, which lead to shifts in the Fermi level, become much smaller than the carriers leading to the electrostatic potential difference, so only ϕ term is considered for mobility calculations with the SiO_2 gate.

After the electrical and optical characterisation of the device, I am interested in its optoelectronic properties. A laser with 473 nm wavelength is rastered on device measuring photocurrent as a function of the position of the laser beam, see Figure 6.2a. For this case, I use graphene on a bulk WS_2 rather than a few-layer WS_2 as a prototype, see Figure 6.2b. The large bulk flakes enable distinguishing photoactive areas clearly. The scan is started from the left electrode to the right recording the photocurrent for each μm distance. This mapping is performed at different gate voltages which are V_{tg} = -1.5 V, 0 V and +1.5 V in ambient conditions. The Figure 6.2a shows an overlap of the maps with optical images of the device.

The results of the photocurrent maps show a large photocurrent difference between graphene on SiO_2 and the graphene on bulk WS_2 regions. More specifically, the photocurrents generated from graphene on SiO_2 and graphene-gold regions are two orders of magnitude smaller than the values recorded in the heterostructure.

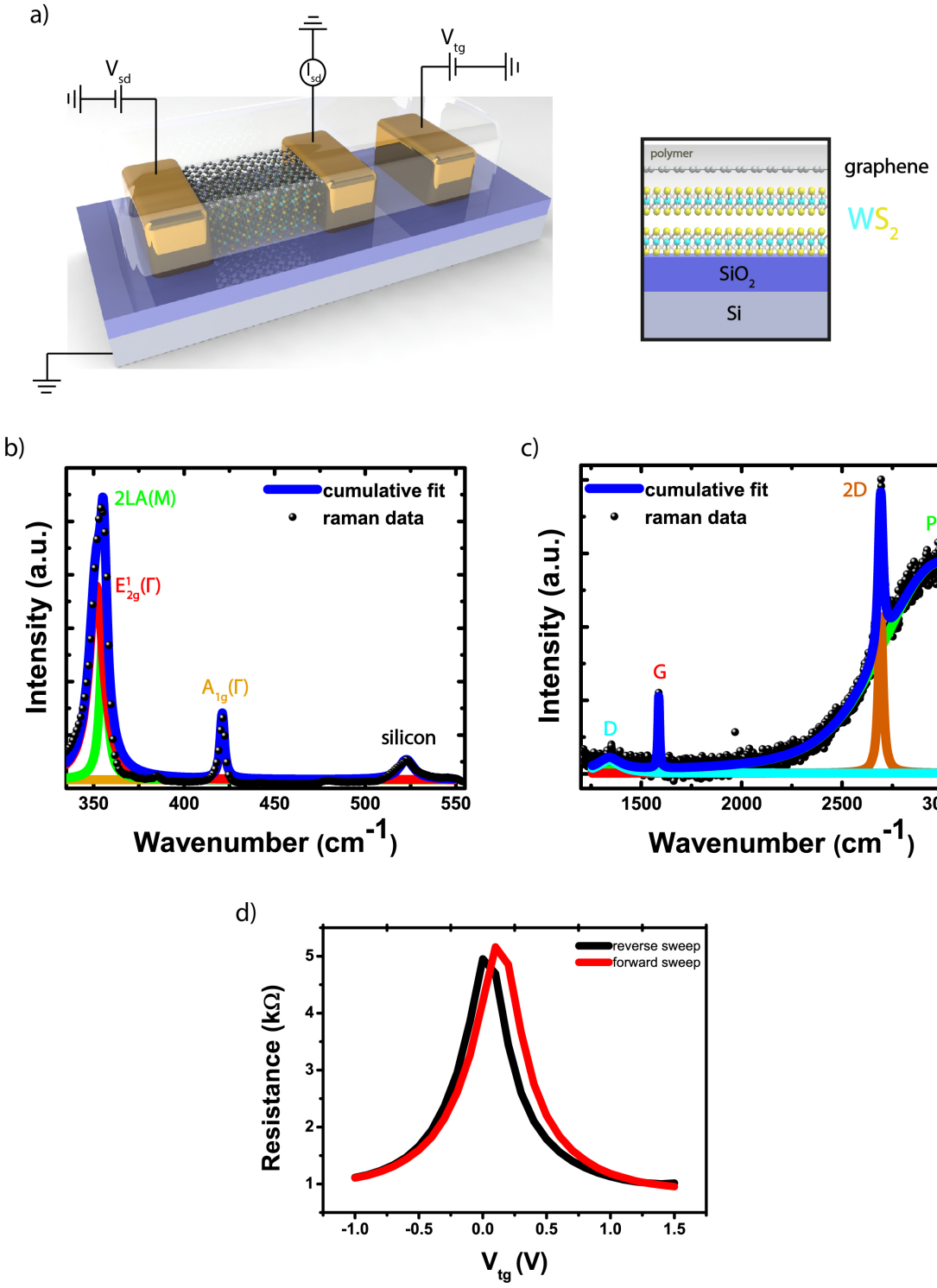

Figure 6.1: (a) Schematic of the few-layer WS_2-graphene device with transparent ionic polymer electrode top. Inset: Cross section view of the device. The gate is biased from the top gate with an independent Au contact, and source-drain voltage is kept constant. Raman spectra of the heterostructure can be divided into two regions. They are (b) WS_2 and silicon peaks and (c) graphene region. (d) The resistance of the graphene sheet on the TMDC with the modulation of the top gate. The contact resistance of graphene is $\sim$ 1 kΩ μm.

Short-circuit configuration is used to study the photocurrent for this device. With this configuration, the photocurrent is measured directly without any source-drain bias, and the dark current is zero. For this reason, a sign change is observed on the maps (blue and red regions) which depend on the doping of the graphene and the electric field on the surface. Under the negative and positive gate bias (V_{tg} = -1.5 V and +1.5 V), an increase on photocurrent is observed and a change in the photocurrent sign on the active regions. This is expected due to the electrostatic change in the Fermi level of the graphene.

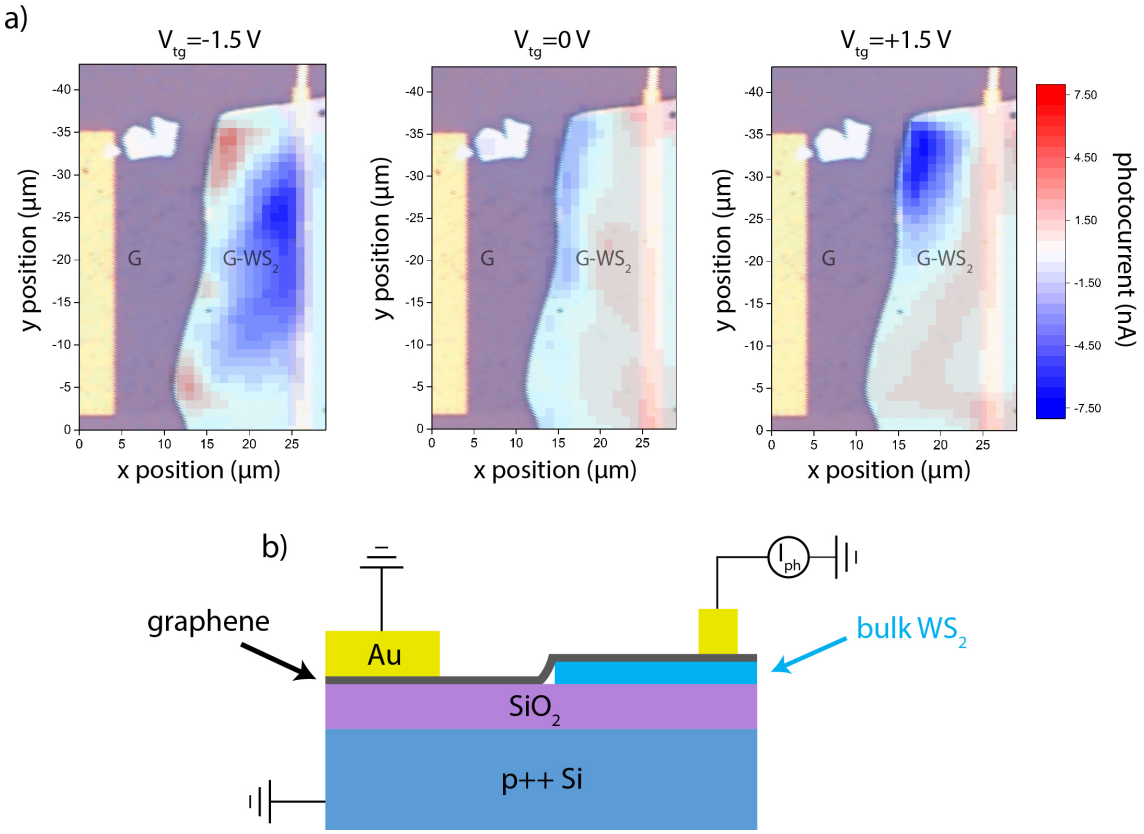

Figure 6.2: (a) Photocurrent maps of the prototype graphene-bulk WS_2 device. The left part of the map contains the only graphene and the right is the heterostructure. Au electrodes are shown in yellow. (b) Schematic of the graphene-bulk WS_2 device.

In order to investigate the behaviour of the few-layer WS_2-graphene device under the gate bias, photocurrent measurements is performed at different gate voltages in dark and light using 600 nm wavelength and 200 $\mu W/cm^2$ power of light, see Figure 6.3a. The resistance of graphene increases when the light is on. The electron-hole pairs split in the graphene-WS_2 interface as the hole remains in the valence band of

WS_2 while the electron is transferred to graphene, see Figure 6.3b. An increase in the resistance is due to the transfer of the electrons into the electrostatically hole doped graphene where $V_{tg} < V_{dirac}$. The separation of charges is assisted by built-in field and the formation of band bending at the interface. This photogeneration mechanism corresponds to the photogating effect or photoconductive effect [2].

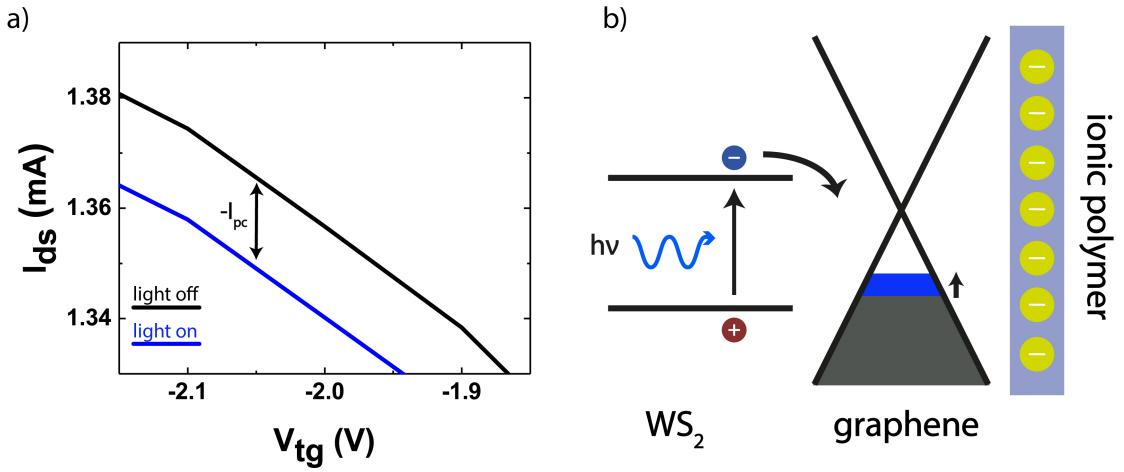

Figure 6.3: (a) Change in source-drain current (I_{ds}) with modulation of the top gate bias (V_{tg}) in dark (black curve) and under illumination (blue curve) of 640 nm and 200 μW/cm^2 light. Source-drain voltage (V_{sd}) is 10 mV. (b) Schematic of the charge transfer between graphene and few-layer WS_2 when $V_{tg} < 0$. The negative charges are transferred to graphene leading an increase in the resistivity. Mobile ions near the graphene surface are ClO_4^-.

The device performance is investigated for the different wavelengths of light. The spectral responsivity of the heterostructure is defined as the photocurrent and power of the light is measured with modulation of the wavelength of the light. To obtain the responsivity, the photocurrent is divided by the optical power of the light for each wavelength. The energy of the light is modulated from 1.8 eV (690 nm) to 3.1 eV (400 nm) with a step of 0.004 eV (0.8 nm). The responsivity, as well as photocurrent of the device, is measured as zero below 1.8 eV. The four main peaks are observed at 1.92 eV, 2.06 eV, 2.36 eV and 2.97 eV, see Figure 6.4a. They are fitted with the Gaussian function. These peaks are expected to be due to electronic transitions in bands of the WS_2.

The first peak at 1.92 eV belongs to the so-called A exciton transition [15].

This peak arises due to the formation of electron-hole bound state with transitions between the upper split of the valence band and the conduction band. The direct band gap transitions from the valence to the conduction band (single-particle gap) result in a peak at 2.06 eV, E_g [16]. This peak represents the electronic band gap at K point, and it corresponds to the energy needed to tunnel an electron and a hole into the WS_2 [17]. The binding energy of the exciton is the difference between the band gap transition energy and the A exciton energy which is 140 meV. For bulk and monolayer WS_2, the binding energy is $\sim$ 50 meV and $\sim$ 300-800 meV respectively [15, 18, 19]. The excitons with large binding energies can contribute to the photocurrent under a large electric field [20]. The lower branch of the valence band transitions can cause B exciton peak at 2.36 eV [21, 22]. The spin-orbit splitting can be calculated from the difference between A and B exciton energies as 440 meV which has been previously reported [23, 24]. The broad peak at 2.97 eV corresponds to transitions between the density of states in the valence and conduction bands. WS_2 has strong light-matter interactions in the visible range of optical spectrum [24]. The localized d orbitals of W atom in the valence band results in high density of states at C peak [24]. A joint density of states peak around this energy point has been reported in reference [24].

Figure 6.5a and b show the rise and fall time of the heterostructure. The black dots are the measured data and the red line is the smoothed data. Blue and green lines are the guides for before and after the light illumination. The dashed lines correspond to 10% and 90% rise and fall in the signal and shaded region represents the raising signal for both Figure 6.5a and b. The results show 2.8 ms rise time and 4.0 ms fall time.

Previous studies with TMDCs and quantum dots (QDs) have longer rise and fall times due to the long-lived charge trapping and slow decay times with persistence of the photocurrent [6, 25, 26]. This is characterised by a larger value of the dark current after having illuminated the sample. To recover the initial value of dark current, large gate pulses are applied. However, these heterostructure devices do not show any persistence, and fall and rise times are much smaller than in previous

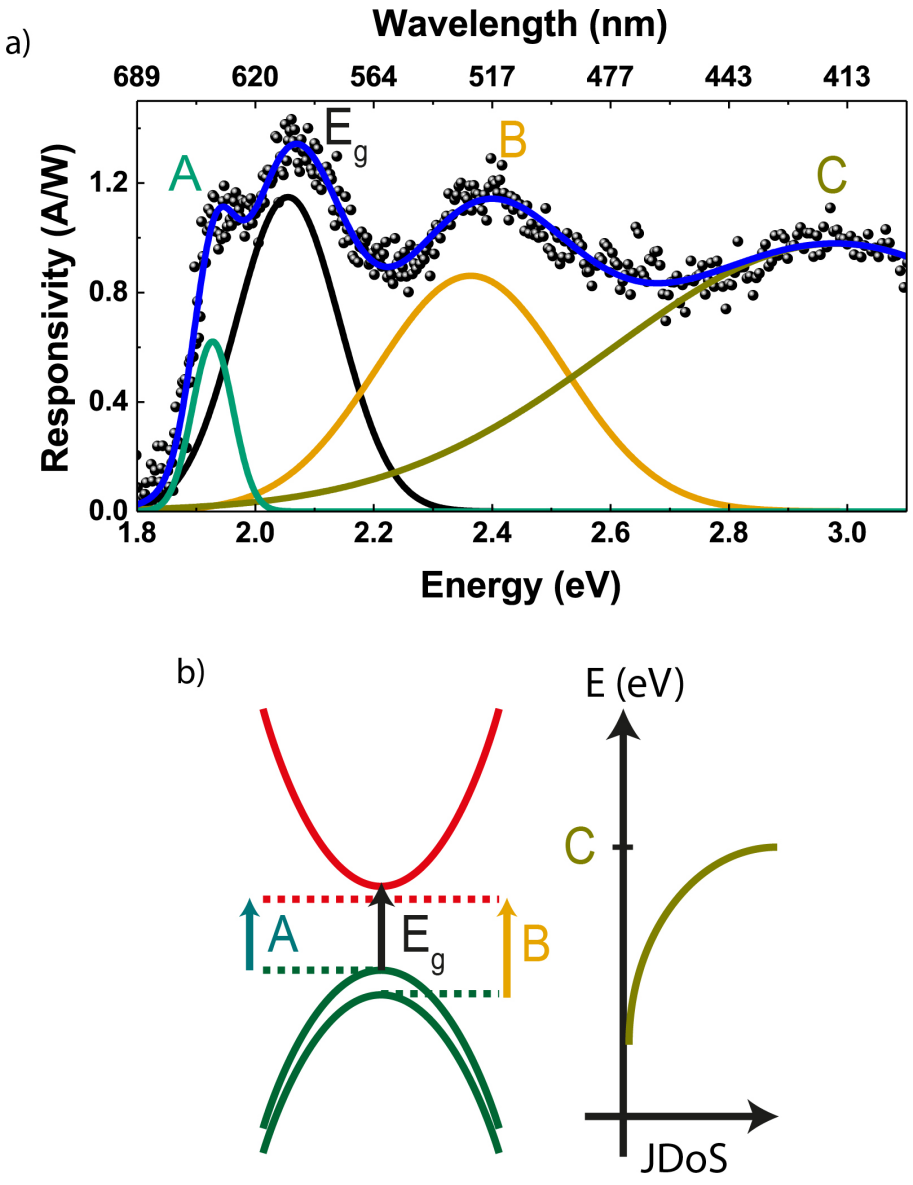

Figure 6.4: (a) Spectral responsivity of graphene/few-layer WS_2. $V_{tg} = 0$ V and $V_{sd} = 10$ mV. A, B and C exciton peaks can be observed as well as the direct band (single-particle) gap peak, E_g. (b) Schematic of the transitions in A, B, C and E_g peaks.

works. Using the top gate as an ionic polymer, the long-lived traps between WS_2 and SiO_2, which cause slow response times, can be screened [27].

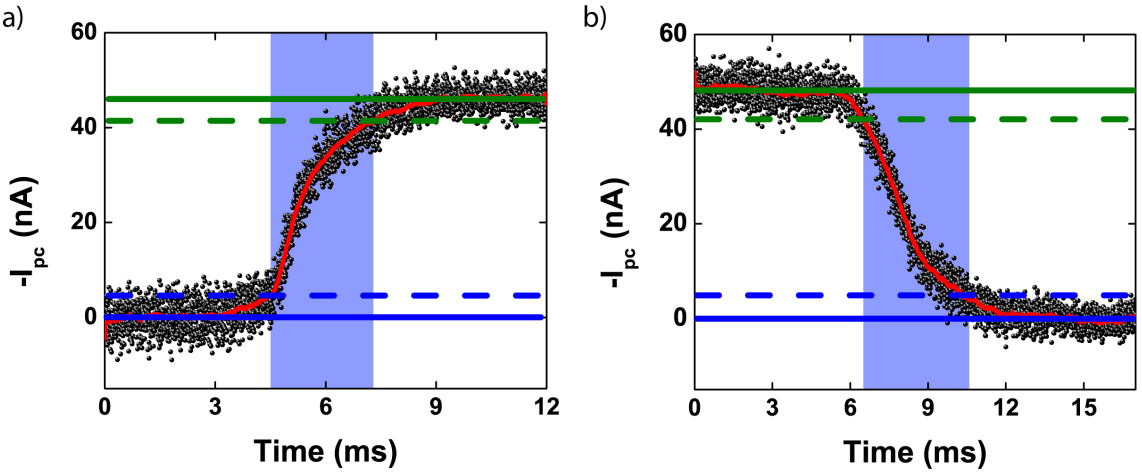

Figure 6.5: (a) Rise and (b) fall time of graphene/few-layer WS_2 under 640 nm illumination and 2 mW/cm^2 optical power. Shaded areas represent the response rise and decay interval. I_{pc} is the photocurrent.

Having characterised the response time of the device, the bandwidth can be investigated. The signal drops down to 70% of its initial value are observed at 125 Hz which is called as cut-off frequency or -3 dB bandwidth, see Figure 6.6a.

Figure 6.6b shows responsivity and EQE of the device as a function of incident optical power. The responsivity and EQE are calculated for each optical power and plotted. The maximum value of the responsivity is found to be reaching up to 3×10^5 A/W and the EQE is 6.2×10^5%. This high responsivity can be explained by the presence of a gain mechanism in which one charge carrier is in a trap state in the WS_2 and the other one circulates until they recombine [2]. The calculated gain is $\sim 10^6$ which is expected considering the achieved mobility and high carrier concentrations with the polymer. Detectivity of the device can also be obtained using the bandwidth, responsivity and area of the device as $D^* \sim 10^{11}$ Jones which is much higher than other graphene-TMDC photodetectors.

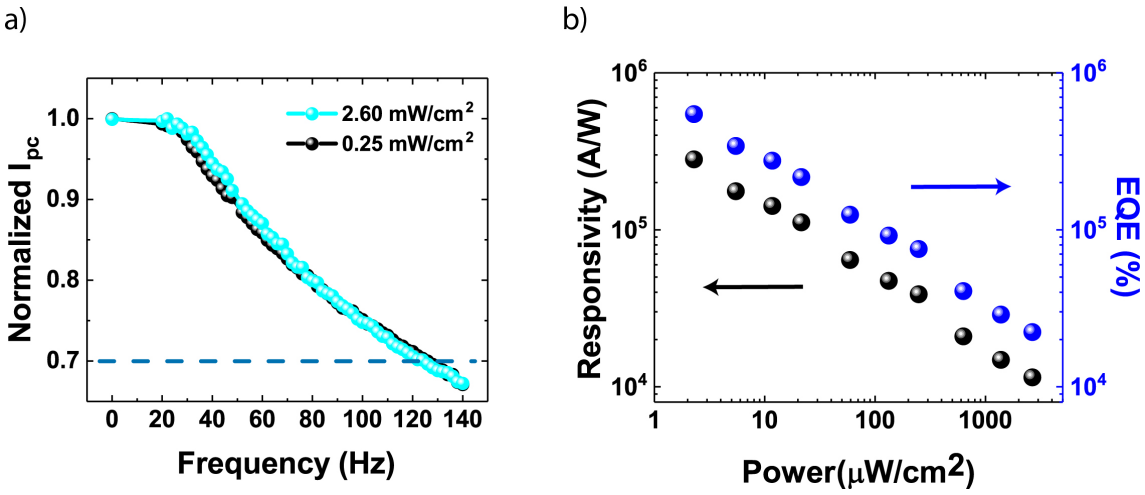

Figure 6.6: (a) Change in the normalised photocurrent with modulation of light frequency measured for two different optical power. The dashed line corresponds to the - 3 dB cut-off frequency which is $\sim$ 125 Hz. (b) Responsivity (black) and EQE (blue) of the device respect to optical power. V_{tg} = -2.0 V and V_{sd} = 0.1 V.

6.4 Conclusion

Graphene-WS_2 heterostructure devices have been electrically and optically characterised. I have used this device as a photodetector and investigated the optical mechanism and device performance. The dominant mechanism was the photogating effect with high gain and responsivity which was approximately 10^6 A/W. The response time and bandwidth of the heterostructure have been examined. The cut-off frequency was 125 Hz and the rise and fall times were 2.8 ms and 4.0 ms. The trap and defect states usually exist in SiO_2 and at the interface between a TMDC and the gate causing a persistent of photocurrent [6]. This limits the photocurrent and the responsivity on these devices. Fast response times and large responsivity were due to the small Debye length of top gate, the reduced trap and defect states between the device and the gate with the ionic liquid and the photoconductive gain mechanism of the WS_2. The detectivity was $\sim 10^{11}$ Jones. This device with its high responsivity and fast response times, it can be used in high frame rate video applications.

Bibliography

[1] A. Kuc, N. Zibouche, and T. Heine, "Influence of quantum confinement on the electronic structure of the transition metal sulfide TS_2," *Physical Review B*, vol. 83, p. 245213, Jun 2011.

[2] F. H. L. Koppens, T. Mueller, P. Avouris, A. C. Ferrari, M. S. Vitiello, and M. Polini, "Photodetectors based on graphene, other two-dimensional materials and hybrid systems," *Nature Nanotechnology*, vol. 9, pp. 780–793, Oct 2014.

[3] C.-H. Liu, Y.-C. Chang, T. B. Norris, and Z. Zhong, "Graphene photodetectors with ultra-broadband and high responsivity at room temperature," *Nature Nanotechnology*, vol. 9, no. 4, pp. 273–278, 2014.

[4] M. Liu, X. Yin, E. Ulin-Avila, B. Geng, T. Zentgraf, L. Ju, F. Wang, and X. Zhang, "A graphene-based broadband optical modulator," *Nature*, vol. 474, pp. 64–67, Jun 2011.

[5] F. Bonaccorso, Z. Sun, T. Hasan, and A. C. Ferrari, "Graphene photonics and optoelectronics," *Nature Photonics*, vol. 4, pp. 611–622, Aug 2010.

[6] K. Roy, M. Padmanabhan, S. Goswami, T. P. Sai, G. Ramalingam, S. Raghavan, and A. Ghosh, "Graphene-MoS_2 hybrid structures for multifunctional photoresponsive memory devices," *Nature Nanotechnology*, vol. 8, pp. 826–830, Nov 2013.

[7] T. H. Bointon, M. D. Barnes, S. Russo, and M. F. Craciun, "High quality monolayer graphene synthesized by resistive heating cold wall chemical vapor deposition," *Advanced Materials*, vol. 27, no. 28, pp. 4200–4206, 2015.

[8] A. Das, S. Pisana, B. Chakraborty, S. Piscanec, S. K. Saha, U. V. Waghmare, K. S. Novoselov, H. R. Krishnamurthy, A. K. Geim, A. C. Ferrari, and A. K. Sood, "Monitoring dopants by Raman scattering in an electrochemically top-gated graphene transistor," *Nature Nanotechnology*, vol. 3, no. 4, pp. 210–215, 2008.

[9] A. Allain and A. Kis, "Electron and hole mobilities in single-layer WSe_2," *ACS Nano*, vol. 8, no. 7, pp. 7180–7185, 2014.

[10] M. Watanabe, S. Nagano, K. Sanui, and N. Ogata, "Ion conduction mechanism in network polymers from poly(ethylene oxide) and poly(propylene oxide) containing lithium perchlorate," *Solid State Ionics*, vol. 18-19, pp. 338–342, Jan 1986.

[11] Z. L. Miskovic, P. Sharma, and F. O. Goodman, "Ionic screening of charged impurities in electrolytically gated graphene," *Physical Review B*, vol. 86, p. 115437, Sep 2012.

[12] P. Sharma and Z. L. Miskovic, "Ionic screening of charged impurities in electrolytically gated graphene: A partially linearized Poisson-Boltzmann model," *Journal of Chemical Physics*, vol. 143, no. 13, 2015.

[13] C. Lu, Q. Fu, S. Huang, and J. Liu, "Polymer electrolyte-gated carbon nanotube field-effect transistor," *Nano Letters*, vol. 4, no. 4, pp. 623–627, 2004.

[14] J. Xia, F. Chen, J. Li, and N. Tao, "Measurement of the quantum capacitance of graphene," *Nature Nanotechnology*, vol. 4, pp. 505–509, Aug 2009.

[15] J. Wilson and A. Yoffe, "The transition metal dichalcogenides discussion and interpretation of the observed optical, electrical and structural properties," *Advances in Physics*, vol. 18, pp. 193–335, May 1969.

[16] H. Zeng and X. Cui, "An optical spectroscopic study on two-dimensional group-VI transition metal dichalcogenides," *Chemical Society Reviews*, vol. 44, no. 9, pp. 2629–2642, 2015.

[17] M. M. Ugeda, A. J. Bradley, S.-F. Shi, F. H. Da Jornada, Y. Zhang, D. Y. Qiu, W. Ruan, S.-K. Mo, Z. Hussain, Z.-X. Shen, F. Wang, S. G. Louie, and M. F. Crommie, "Giant bandgap renormalization and excitonic effects in a monolayer transition metal dichalcogenide semiconductor," *Nature Materials*, vol. 13, no. 12, pp. 1091–1095, 2014.

[18] A. Chernikov, T. C. Berkelbach, H. M. Hill, A. Rigosi, Y. Li, O. B. Aslan, D. R. Reichman, M. S. Hybertsen, and T. F. Heinz, "Exciton binding energy and nonhydrogenic rydberg series in monolayer WS_2," *Physical Review Letters*, vol. 113, p. 076802, Aug 2014.

[19] A. T. Hanbicki, M. Currie, G. Kioseoglou, A. L. Friedman, and B. T. Jonker, "Measurement of high exciton binding energy in the monolayer transition-metal dichalcogenides WS_2 and WSe_2," *Solid State Communications*, vol. 203, pp. 16–20, 2015.

[20] A. R. Klots, A. K. M. Newaz, B. Wang, D. Prasai, H. Krzyzanowska, J. Lin, D. Caudel, N. J. Ghimire, J. Yan, B. L. Ivanov, K. A. Velizhanin, A. Burger, D. G. Mandrus, N. H. Tolk, S. T. Pantelides, and K. I. Bolotin, "Probing excitonic states in suspended two-dimensional semiconductors by photocurrent spectroscopy," *Scientific Reports*, vol. 4, p. 6608, 2014.

[21] S. Hwan Lee, D. Lee, W. Sik Hwang, E. Hwang, D. Jena, and W. Jong Yoo, "High-performance photocurrent generation from two-dimensional WS_2 field-effect transistors," *Applied Physics Letters*, vol. 104, no. 19, p. 193113, 2014.

[22] B. Zhu, X. Chen, and X. Cui, "Exciton binding energy of monolayer WS_2," *Scientific Reports*, vol. 5, p. 9218, Mar 2015.

[23] W. Zhao, Z. Ghorannevis, L. Chu, M. Toh, C. Kloc, P.-H. Tan, and G. Eda, "Evolution of electronic structure in atomically thin sheets of WS_2 and WSe_2," *ACS Nano*, vol. 7, pp. 791–797, Jan 2013.

[24] L. Britnell, R. M. Ribeiro, A. Eckmann, R. Jalil, B. D. Belle, A. Mishchenko, Y.-J. Kim, R. V. Gorbachev, T. Georgiou, S. V. Morozov, A. N. Grigorenko, A. K. Geim, C. Casiraghi, A. H. Castro Neto, and K. S. Novoselov, "Strong light-matter interactions in heterostructures of atomically thin films," *Science*, vol. 340, pp. 1311–1314, Jun 2013.

[25] G. Konstantatos, M. Badioli, L. Gaudreau, J. Osmond, M. Bernechea, F. P. G. de Arquer, F. Gatti, and F. H. L. Koppens, "Hybrid graphene-quantum dot phototransistors with ultrahigh gain," *Nature Nanotechnology*, vol. 7, no. 6, pp. 363–368, 2012.

[26] Y. J. Zhang, T. Oka, R. Suzuki, J. T. Ye, and Y. Iwasa, "Electrically switchable chiral light-emitting transistor," *Science*, vol. 344, pp. 725–728, May 2014.

[27] S. Ghatak, A. N. Pal, and A. Ghosh, "Nature of electronic states in atomically thin MoS_2 field-effect transistors," *ACS Nano*, vol. 5, pp. 7707–7712, Oct 2011.

Chapter 7

Conclusion

7.1 Research implications and limitations

In this thesis, current-voltage characteristics of WS_2 and graphene FETs were experimentally investigated. Graphene was also used as a side gate, and leakage through the insulator and the environment was discussed. Optoelectronic properties and performance of ionic polymer gated graphene-WS_2 heterostructure were demonstrated. I have developed transport properties and applications of two-dimensional materials.

The first objective was to investigate transport properties of CVD grown WS_2. Metal contacts on CVD grown trilayer WS_2 were fabricated. Schottky barrier between the semiconducting TMDC and metal caused resistances of tens of MΩ to GΩ. The contact resistance conceals the electronic properties of WS_2 and could result in low mobility. With a voltage bias annealing in liquid helium, this resistance was reduced at least an order of magnitude. This resistance was due to the difference in the work function of the contact metal and the electron affinity of the WS_2. Other effects such as strong Fermi-level pinning and lattice mismatch could contribute to this resistance.

Electrical transport in the leakage provided by graphene side gates was investigated. Transport measurements of graphene in ambient conditions showed that the graphene was p-doped and the minimum sheet resistance was ~ 9 k$\Omega/\square$. The side gate leakage measurements in a vacuum chamber indicated two different transport

mechanism. Frenkel-Poole transport was effective at low voltage bias ($V_{sg} < 60$ V) which the carriers were transmitted by SiO_2 trap states. However, with biases between 60 V and 70 V, the carriers were both transmitted by SiO_2 and the vacuum environment. This was explained by Fowler-Nordheim tunnelling.

Finally, the optoelectronic properties and photodetector applications of ionic polymer gated graphene-TMDC heterostructure were presented. Ionic polymer gate screened trap states and resulted in a clean interface between the gate and the material. The photoresponsivity of this device could reach up to 10^6 A/W and the response time was in the order of milliseconds. The photoconductive gain was $\sim 10^6$. Due to the high gain mechanism and reduced trap states at the interface of the gate, high photoresponsivity and fast response times, 2.8 ms and 4.0 ms, were achieved. This has been the first graphene-TMDC photodetector having such a high responsivity, gain and fast response times at the same time.

7.2 Future work

Field-effect transistors based on two-dimensional materials and their heterostructures have been studied extensively. With their electrical and optical properties, they have a potential to be used in future nanoelectronics. In order to improve these devices;

- transport properties and mechanisms in the metal-TMDC contact interface could be studied,
- the size of the depletion region, the Schottky barrier, the Fermi-level pinning and gate voltage dependence need to be investigated,
- growth methods of the CVD TMDCs has to be improved to obtain clean, impurity free surface and large area flakes,
- the interface between metal and the atomically thin materials could be improved by future doping methods or phase changing methods [1–3],

- the side gate transport properties at high voltage biases and the reason of the degradation need to be understood,
- efficiency comparison between the ionic polymer gate and the back gate needs to be performed,
- the back gate and the ionic polymer electric fields could be combined to increase the optical responsivity in the hybrid devices,
- the role of charge trap states in the hybrid devices could be studied,
- the response time in graphene devices could be improved by the top gate and bottom gate studies and increasing the mobility of the semiconductor.

Bibliography

[1] R. Kappera, D. Voiry, S. E. Yalcin, B. Branch, G. Gupta, A. D. Mohite, and M. Chhowalla, "Phase-engineered low-resistance contacts for ultrathin MoS_2 transistors," *Nature Materials*, vol. 13, pp. 1–15, Aug 2014.

[2] D. Jena, K. Banerjee, and G. H. Xing, "Intimate contacts," *Nature Materials*, vol. 13, no. 12, pp. 1076–1078, 2014.

[3] L. Yang, K. Majumdar, H. Liu, Y. Du, H. Wu, M. Hatzistergos, P. Y. Hung, R. Tieckelmann, W. Tsai, C. Hobbs, and P. D. Ye, "Chloride molecular doping technique on 2D materials: WS_2 and MoS_2," *Nano Letters*, vol. 14, pp. 6275–6280, 2014.